University of Stavanger

Faculty of Science and Technology

MASTER`S THESIS

Study program/specialization: Petroleum Technology/production	Spring semester, 2014 Open
Writer: Silje Bru	…… (Writer`s signature)
Faculty supervisor: Thor Martin Svartås Co – supervisor: Runar Bøe	
Title of Thesis: "Heat transfer measurements in stirred, cylindrical cells containing ethylene oxide (EO) and tetra hydro furan (THF) hydrate – water solutions at temperatures between 1 – 4 °C as function of amounts and volume of hydrates present in the solutions."	
Credits (ECTS): 30	
Key words: Hydrate growth, controllable hydrates, miscible solution, heat transfer coefficient	Pages: 86 + Enclosure:18 Stavanger, …….. date/year

PREFACE

After reading about the topics of this year thesis I made my decision writing about gas hydrates. During my bachelor thesis mu interests in gas hydrates and laboratory work were improved.

The content presented in this thesis is inspired by two papers written by Remi-Erempagano Meindinyo: “Hydrate growth estimation from heat transfer – experimental result analysis” and “Heat transfer during hydrate formation – an investigation on the effect of hydrate content on the heat transfer coefficient of gas hydrate slurry”. It should be noted that Meindinyo`s paper are based upon a former thesis by Nordbø; “Hydrate growth kinetics: A study on the relation between energy release rates and gas consumption rates during methane hydrate formation and growth” is the former papers based on.

I am so grateful for my supervisor Prof. Thor Martin Svartås, who has been very helpful, and advised me. I will also give a big thanks to my co-supervisor Prof. Runar Bøe, who has helped me with the analysis on Matlab, and understand heat transfer in a better manner. Ph.D student Remi Meindinyo helped and assists me at the laboratory and my thesis in general, I am so grateful.

In the end I will give thanks to the staff at the hydrate laboratory, the library staff and my family.

ABBREVIATION

conc. = concentration

EO = Ethylene Oxide

HCS = Heating and cooling sequence

HTC = Heat transfer coefficient

LDHI = Low dosage hydrate inhibitor

mole % = Mole percent

Re = Reynolds number

sI = Structure I

sII = Structure II

sH = Structure H

SHS = Stable hydrate structure

Teq = Equilibrium melting temperature

THF = Tetrahydrofuran

vs = versus

NOMENCLATURE

Symbols:

A = matrix A

A = surface area [m^2]

α = thermal diffusivity [m^2/s]

Bi = Biot`s number [-]

C = the concentration [mole/L] or [%]

C = the cell interior [-]

c_p = specific heat capacity at constant pressure [J/kg K]

δ = thickness [m]

Δh = the heat formation per unit mass [J/mole]

f_i = the fugacity of component i in the bulk phase [Pa]

Fo = Fourier`s number [-]

h = the overall heat transfer coefficient [W/m^2K]

K = k = mass transfer coefficient through the film around the particle [m/s]

λ = thermal conductivity [W/m K]

m = mass [kg]

n = number of moles [mole]

N = number of moles of gas (air) [mole]

Q = **q** = heat flow [W/m^2]

r = inner cell radius [m]

R = outer cell radius [m]

ρ = density [kg/m^3]

T = matrix T

T = temperature [K]

t = time [s]

t = time of hydrate formation [s]

v = the linear growth rate [1/s]

x_b = the molefraction [-]

$x= x_h$ = the x – position at the hydrate- film front [-]

X = temperature equivalent for heat generation [K]

Y = matrix Y

Sub – script:

conv. = convection

d = through hydrate film around the particle

f = hydrate film

g = gas

g-1 = gas – liquid interface

h = H = hydrate

I = inner boundary

i = interior

int = bulk – liquid interface

L = liquid film

n = outer border or wall

n – 1 = second last node

o = initial condition

O = outer boundary

p = particle

r = rate constant

w = water

∞ = the bulk/fluid near the wall

1n = first node

2n = second node

Super – script:

b = bulk phase

eq = equilibrium in the liquid phase

p = current time step

p +1 = future time step

p -1 = previous time step

*= hydrate growth constant

ABSTRACT

It is believed that heat transfer plays a major role in hydrate formation, and is also dependent on the hydrate concentration. Heat transfer during hydrate growth is an important process, which deserves a great depth of study.

The aim of this present work is to analyze the heat transfer properties of hydrate – water suspensions/slurries as function of hydrate concentration in the slurry. Ethylene oxide (EO) and tetrahydrofuran (THF) was used as hydrate formers. Both of these components are completely soluble in water and the amount of hydrates formed was controlled by the given stoichiometric concentration of EO or THF added to the water prior to hydrate formation. Heat transfer properties of the EO and THF hydrate suspensions were measured in the temperature region between 1 and 4 °C.

The analytical model and program used, is based on the former studies of Meindinyo. The program can be used to predict and validate the heat transfer coefficient of the aqueous phase/solution present in the cell interior through temperature responses during controlled heating and cooling cycles.

The stability of the hydrates during the test was dependent on the hydrate equilibrium properties of the system at the given concentration of EO and THF in the water phase. For concentrations less than 40 % of stoichiometric concentration the THF and EO hydrates dissociated during the test sequence between 1 and 4 °C. The heat transfer coefficient of hydrate suspension (hI) showed a general dependence on amount of hydrate in slurry. hI decreased with an increase in amount of hydrate in hydrate suspension. Analysis was also carried the effects of stirring rate, and cell volume on the heat transfer behavior.

TABLE OF CONTENTS

1 INTRODUCTION

1.1 Natural gas hydrates – historical review

In 1778 Joseph Priestly (Priestly & Pearson, 1790) observed that "Ice was formed at temperatures above 0°C by water in presence of SO_2". Without knowing the "ice" was hydrate, Priestly described the formation of hydrates for the first time in history.

Research on gas hydrates can be divided into three different eras. (E. Dendy Sloan & Koh, 2008)

The first era: Gas hydrates formed by use of chlorine and water were discovered by Humphrey Davy in 1810 (Davy, 1811). Following his discovery, in the time period 1810 – 1925 several forming gas hydrates components were identified, and gas hydrates remained of academic interest until 1934. (E. Dendy Sloan & Koh, 2008)

In 1896 Villard was the first to use heat of formation data to obtain a gas/water ratio and to determine the hydration number. (Villard, 1896)

The second era started when Hammeschmidt (Hammerschmidt, 1934) discovered in 1934 that ice caused plugged natural gas pipelines. As a result of this discovery, the oil and gas industry recognized hydrates as a gas transportation problem. In 1946 Deaton and Frost (Deaton & Frost, 1946) proposed a hydrate prevention method based on experimental and simulated results observed from formation of hydrates of both pure and heavy mixtures of methane, ethane and propane.

Katz and other scientists developed methods to predict hydrate formation temperature and pressure by use of "gas gravity" charts (Wilcox, Katz, & Carson, 1941). Along with "gas gravity" charts, the understanding of the science of hydrate formation advanced as Van der Waals and Platteeuw in 1959 described hydrate formation conditions through a model combining statistical and classical thermodynamics (Van der Waals & Platteeuw, 1959). However, it was not until 1972 that this model could be practically used due to lack of solution methods, for use in computer programs. Parrish & Prausnitz (Parrish & Prausnitz, 1972) developed a numerical solution method that could be used in computer software.

The third era began in 1960 when Makogon et al. (Y. F. Makogon, 1965) reported finding gas hydrates formed in Siberia. This period is still highly relevant today because it has been discovered that natural gas hydrates exist in permafrost and sediments, below the sea floor.(E. Dendy Sloan & Koh, 2008) Thus, in the 21st century logging and coring tools for recording gas hydrates in permafrost regions and oceanic locations have been developed. (Trèhu et al., 2006)

Introduction to "cold flow" took place in 2004 when Camargo et al. and BP/SINTEF demonstrated prevention of hydrate plugging in pipelines, without the use of any chemical additives, producing dry hydrate that could be transported as small particles dissolved in the liquid hydrocarbon phase along the line. (Camargo & Goncalves, 2004; E. Dendy Sloan & Koh, 2008)

There are different proposals on how to classify the chemical nature of guest molecules. One proposal on classifications was written by Jeffrey and McMullan in 1967. They proposed that the guest molecules of hydrates must lie within four groups, where the third group is "water soluble polar compounds" where miscible aqueous solutions of Ethylene oxide (EO) and Tetrahydrofuran (THF) belong. (McMullan & Jeffrey, 1965)

In the 1970s it was first discovered by Kuliev how surfactants prevent hydrate formation in a well. It was, however, not until the 1980s further work was done on Low Dosage Hydrate Inhibitors (LDHIs). (Kelland, 2006)

1.2 Background

Offshore producing oil and gas fields can be connected with subsea satellite wells for first stage processing before further transport of separated gas and oil through pipelines and then tankers. Between the satellite wells and the offshore production platform (or an onshore processing unit) the fluids in a minimum processed (or unprocessed) state are transported through pipelines for further processing. The water associated with oil and gas transport may convert into hydrate and has the potential of creating a hydrate plug if the fluid temperature enters the hydrate region. If the conditions are kept inside of the hydrate stability zone, a

hydrate plug may form and fill the entire cross-sectional area of the pipe, and the pipeline becomes blocked. The design of multiphase transmission system, which would prevent hydrate blockage, requires knowledge of heat and mass transfer of hydrate formation. (Creek, Douglas, & Subramanian, 2011; Dorstewitz & Mewes, 1993; Mork & Gudmundsson, 2001)

Hydrates can be formed in marine sediments when methane, either from biogenic or thermogenic sources, comes into contact with water (Kvenvolden & Claypool, 1985).Malone (Malone, 1985) suggests there are four types of hydrate consolidations; disseminated, nodular, layered and massive. For production of the methane and hydrocarbons from hydrate-bearing sediments, the use of thermal simulation techniques may be one of the options. Thermal properties are central for optimization of such techniques (Hovland & Gudmestad, 2001; Pooladi-Darvish, 2004). Enthalpy data provide correct evaluation of the recovery of hydrates found in natural deposits. (Lesist, Murray, Post, & Davidson, 1982)There are no comprehensive studies in hydrate-bearing sediments (Waite, Gilbert, Winters, & Mason, 2005). Dissociation of hydrates by pressure reduction or by injection of antifreeze (ice dissolver), like methanol, may be other methods to stimulate gas production from hydrates. (Kelland, 2009; E. D. Sloan, Koh, & Sum, 2011; Sloan Jr, 2000)

It is believed that gas hydrate growth is controlled by three main mechanisms(E. Dendy Sloan & Koh, 2008):

1. Intrinsic growth kinetics (Englezos, Kalogerakis, Dholabhai, & Bishnoi, 1987a, 1987b)
2. Mass transfer limited kinetics (Skovborg & Rasmussen, 1994)
3. Heat transfer limited kinetics (Uchida, Ebinuma, Kawabata, & Narita, 1999a)

The above mechanisms are probably interconnected, but during measurements one individual mechanism can appear as dominant dependent on equipment and process conditions. The growth rate, described through the two former models, is a function of reaction rate (intrinsic kinetic model), mass transfer (both models) and a driving force in the form of fugacity or concentration gradients in the system. The latter mechanism is a function of heat transfer coefficient and a driving force in form of a temperature gradient only.

In recent time it has been suggested that during hydrate growth intrinsic kinetics plays a less dominant role than mass and heat transfer. It is also believed that the melting process is dominant by heat transfer. However, the melting process can be affected by both mass transfer and internal kinetics and as a result it is uncertain which physical process is more dominant in determining hydrate growth. (E. Dendy Sloan & Koh, 2008)

The formation of hydrates is an exothermic process and thus hydrate growth is followed by energy release. The energy release at onset of hydrate formation in the experimental setup is reflected through a sudden temperature increase within the cell.(Abay & Svartaas, 2010; Abay, Svartaas, & Ke, 2011) Presumably the driving force will be affected by temperature changes in the cell. Therefore, it is reasonable to assume that the measured growth rate of hydrates, during cell experiments, is a function of both mass and heat transfer rates, though the overall growth process may be limited by the mass transfer rate.

In 2012 the hydrate group from the Department of petroleum engineering at the University of Stavanger, conducted cell experiments in an effort to investigate how hydrate growth and heat release are connected. The results of these experiments were used to help model the formation and growth process of gas hydrates through energy balance. The modelling was a part of a PhD study by Remi-Erempagano Meindinyo, commencing fall 2012. The first description established as a simple model using heat balance based on the heat fluxes occurring in the cell during hydrate formation. This model was tested experimentally during a MSc thesis work at UiS in 2013 (Nordboe, 2013). In the model the energy influx is related to the amount of hydrates formed and its heat of formation, while the energy outflow is related to temperature differences between the cell interior and the cooling water on the outside.

Therese Nordbø (Nordboe, 2013) measured the gas consumption and simultaneous temperature fluctuations in a cell during growth of methane hydrate. She utilized the model to simulate the cell temperature during growth and observed an overestimation between the model and the measurements, where the heat transfer properties and the coefficients would likely be not matching. It was concluded there was a discrepancy between the simulations and the measurements, caused by variations in the boundary layers affected, in all probability, by the formed hydrates.

Meindinyo et al. (Meindinyo, Svartaas, & Boe, 2014a) measured heat transfer properties of slurries containing different amounts of methane hydrate. A relation between the amount of hydrate in the slurry and heat transfer was demonstrated. Another study by Meindinyo et al. (Meindinyo, Svartaas, Nordbø, & Boe, 2014b) based on Nordbø`s data tuned the heat transfer coefficients during hydrate formation and obtained a better fit between measured and simulated temperature response. Decay in heat transfer as a function of increasing concentration of hydrates in the resulting water slurry, was suggested.

1.3 Definition of the thesis

It was proposed to improve the analytical (simulated) model by examining the effects of an increasing hydrate mass on heat transfer properties during hydrate growth. In the measurements done by Meindinyo et al.(Meindinyo et al., 2014a) the amount of methane hydrate present was difficult to control, and repeating such measurements by use of THF hydrate (structure II (sII)) and EO hydrate (structure I (sI)) was proposed. Both THF and EO, are completely miscible with water (aqueous phase). By adding the given amount of THF or EO to the water, the amount of hydrates can be controlled, controlling the fraction of water that can be converted into hydrates. The effects of hydrate concentration on heat transfer properties could be measured starting at the stoichiometric concentration of THF/EO in water solution, where the total amount of hydrates are formed, and reducing the concentration in steps down to a minimum level. (Ashworth, Johnson, & Lai, 1984; Glew & Rath, 1965; Larsen, Knight, & Sloan, 1998; Mak & McMullan, 1965; T. Y. Makogon, Larsen, Knight, & Sloan Jr., 1996; McMullan & Jeffrey, 1965; Ross & Andersson, 1982)

The purpose of the present MSc thesis is to measure heat transfer properties of hydrate slurries suspensions concentrations of gas hydrates using miscible solutions of THF and EO. The aim in general is to collect data required for improving the analytical model described by Meindinyo`s PhD study (Meindinyo et al., 2014b).

1.4 Terminology

In this present thesis different terms have been used on the parameter: “Amount of hydrates”, and “estimated heat transfer coefficient (HTC)”. These are explained below:

1.4.1 Amount of hydrate

When using the term “% stoichiometric concentration of THF/EO” it is referred to “% amount of THF/EO hydrate”, “% THF/EO” and/or “% content of THF/EO”.

The relationship between THF and water is: 1:17 molecules in stoichiometric mixture. 1 molecule of THF and 17 molecules of water corresponds with one hundred percent conversion of water into hydrate.(T. Y. Makogon et al., 1996)

The same principle is the same regarding 100% stoichiometric EO solution; where the relationship between EO and water is: 3:23 molecules.(Larsen et al., 1998)

1.4.2 Heat transfer coefficient

When using the term “estimated HTC” it is referred to the “inner heat transfer coefficient (hI)”.

2 Theoretical background

2.1 Natural gas hydrate crystal – Hydrate formers and structures

2.1.1 Hydrate structures

Natural gas hydrates have an ice-like structure composed of water and gas molecules. In the gas hydrate structure guest molecules (gas) are entrapped in lattice cages/cavities formed the water cavities (host), and when the required fraction of cavities is filled with gas the hydrate is stable. Compared to ice, hydrates may form at temperature above 0°C dependent on guest type and pressure. (E. Dendy Sloan & Koh, 2008)

The physical conditions necessary for hydrate formation to form are: a hydrate guest molecule, free water and correct pressure-temperature conditions. Without any of these mentioned conditions, hydrates will not form. (E. Dendy Sloan & Koh, 2008)

Hydrate cavities are also called unit cells (i.e. the building blocks of the hydrate), formed by hydrogen-bonded water molecules composed of polyhedral There are different sizes of cavities (sI, sII, or sH). The guest molecule can be classified through physical/chemical properties and shape determining the hydrate structured formed. (E. Dendy Sloan & Koh, 2008) Occupation of all the large cages in a hydrate it is concluded that the hydrate structure is stable. For sI (EO) it requires minimum of 6 guest molecules.(Dyadin, Bondaryuk, & Zhurko, 1991)

A hydrate system presenting EO or THF will have the hydrate structure I or II, respectively. (Larsen et al., 1998)

Illustration of both shape and geometry of the different structures are illustrated in Figure 1 and Table 1, respectively.

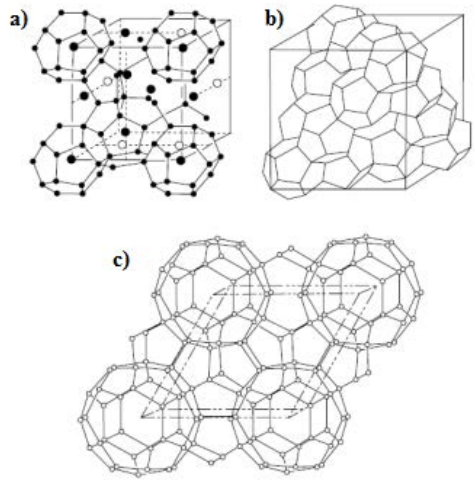

Figure 1: Figure 1: Hydrate crystal unit structure: (a) sI(McMullan & Jeffrey, 1965) , (b) sII(Mak & McMullan, 1965) , and (c) sH(E. Dendy Sloan & Koh, 2008).

Table 1: The geometry of cages in sI, sII and sH hydrates (E. Dendy Sloan & Koh, 2008)

Geometry of Cages

Hydrate crystal structure	I		II		H		
Cavity	Small	Large	Small	Large	Small	Medium	Large
Description	5^{12}	$5^{12}6^2$	5^{12}	$5^{12}6^4$	5^{12}	$4^35^66^3$	$5^{12}6^8$
Number of cavities/unit cell	2	6	16	8	3	2	1
Average cavity radius[a] (Å)	3.95	4.33	3.91	4.73	3.94[b]	4.04[b]	5.79[b]
Variation in radius[c] (%)	3.4	14.4	5.5	1.73	4.0*	8.5*	15.1*
No. of water molecules/cavity[d]	20	24	20	28	20	20	36

[a] The average cavity radius will vary with temperature, pressure, and guest composition.
[b] From the atomic coordinates measured using single crystal x-ray diffraction on 2,2-dimethylpentane · 5(Xe,H_2S)-34H_2O at 173 K (from Udachin et al., 1997b). The Rietveld refinement package, GSAS was used to determine the atomic distances for each cage oxygen to the cage center.
[c] Variation in distance of oxygen atoms from the center of a cage. A smaller variation in radius reflects a more symmetric cage.
[d] Number of oxygen atoms at the periphery of each cavity.

Asterisks represent the variation in radius taken by dividing the difference between the largest and smallest distances by the largest distance.

2.1.2 Hydrate forming liquids and gases

Over 130 compounds are known to form of sI, sII or sH with water molecules. The hydrate forming ability is function of shape, size (non-stoichiometric value) and chemical nature of the guest molecules. (E. Dendy Sloan & Koh, 2008)

THF and EO are two hydrate formers used in the present study. This is described in more details in Table 2.

A comparison of the composition and molecular structure of THF, EO and water (ice) is illustrated in Figure 2.

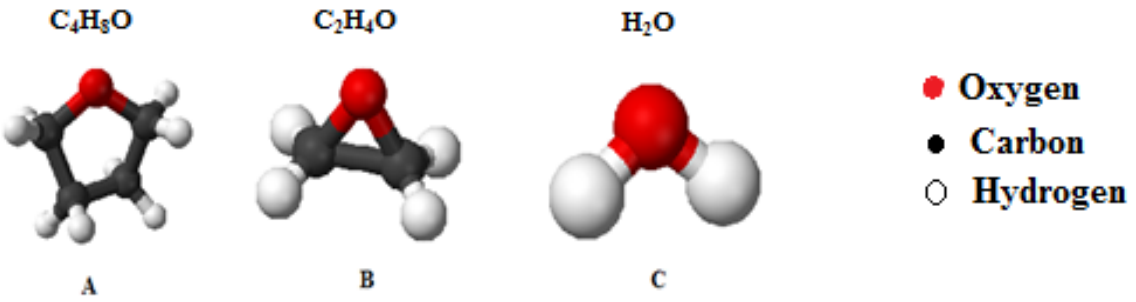

Figure 2: The composition and molecular structure of (A) THF (Vogel, EOSTG, & council, 2007) , (B) EO (Jynto, 2011) , and (C) water (ice) (Vogel et al., 2007).

Table 2: THF vs. EO

Chemical	THF	EO	Water (ice)
Composition	C_4H_8O[e]	C_2H_4O[k]	H_2O[i]
Molacular weight (g/mol)	72.11[j]	44.01[k]	18.015[i]
Density (g/cm^3)	0.8892[e]	0.9682[f]	1.0[e](0.917[e])
Equilibrium melting point (°C)	4.4[a] (4.98*)	11.0[a]	0.0[i]
Heat capacity (J/kg °C)	1600[d]	2000[f]	2405[b](2100[e])
Stoichiometry (water:component)	1:17[g]	3:23[h]	-
Soluble in water	Miscible[c]	Miscible[c]	N/A[e]

[a] Calculated by Sloan et al. (E. Dendy Sloan & Koh, 2008) in a system with hydrogen at atm. pressure
*Calculated by Svartaas, T.M. in a system with nitrogen at atm. pressure (Svartaas, 2014).
[b] **Heat capacity of water (Haas, 1950)**
[c] **Solubility of THF and EO(Larsen et al., 1998)**

[d] **Measured by Tombari et al. (Tombari, Presto, Salvetti, & Johari, 2006)**
[e] **(Lee, Yun, Santamarina, & Ruppel, 2007)**
[f] **Calculated by Dever et al (Dever, George, Hoffman, Soo, & corp., 1994)**
[g] **Measured by Erva (Erva, 1956)**
[h] **Measured by Glew & Rath (Glew & Rath, 1995)**
[i] **Properties of water (Torkildsen, 2013)**
[j] **Molecular weight of THF (Loudon, 2002)**
[k] **Composition and molecular weight of EO (McKetta & Cunningham, 1984)**

During hydrate formation Glew and Rath (Glew & Rath, 1966) observed that EO-rich solutions (>14%) have a higher density than EO-lean solutions (<14%). They hypothesized that density and system composition are dependent on each other. This is confirmed by XRD and Raman spectroscopy by Huo et al.(Huo, Jager, Miller, & Sloan, 2002)

2.2 Hydrate formation

Gas hydrate formation is a crystallization process which starts with nucleation followed by crystal growth. The nucleation process is stochastic and therefore very unpredictable. Various methods, including experimental, theoretical, and numerical, have been proposed for use in studying the nucleation process. But hydrate nucleation remains a subject of great curiosity. Gas hydrate growth unlike nucleation is a continuous crystallization process. It is predictable and thus is handled from a deterministic approach. (E. Dendy Sloan & Koh, 2008) The growth process starts when nucleating hydrate clusters have achieved a critical size, after which spontaneous growth proceeds. (Baez & Clancy, 1994; Christiansen & Sloan Jr, 1994; Hawtin & Rodger, 2006; Kashciev & Firoozabadi, 2002; Kvamme, 1996; Long, 1994; Moon, Taylor, & Rodger, 2003; Mullin, 1993; Radhakrishnan & Trout, 2002; E. Dendy Sloan & Koh, 2008) (This present thesis will not go into further details about nucleation.)

2.2.1 Hydrate crystal growth

2.2.1.1 Molecular concept of crystal growth

In hydrate formation, nucleation; surface area, agitation, water history, etc are important parameters controlling hydrate growth as well as mass and heat transfer. Hydrate formation is exothermic process and the growth is followed by heat release. Hydrate growth is function of the rate of gas consumption which can be controlled by heat and/or mass transfer together

with kinetics. (E. Dendy Sloan & Koh, 2008) which factor is dominant, and the process controlling the hydrate formation, is still under discussion.

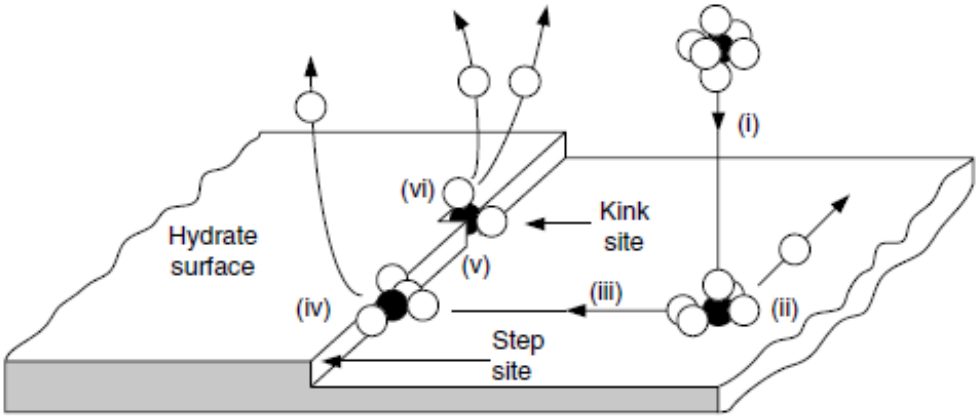

Figure 3: Hypothesis picture of hydrate growth at a crystal. (Elwell & Scheel, 1975)

Figure 3 gives a hypothetical picture of hydrate crystal growth, on a molecular level. The figure illustrates a cluster of water molecules surrounding a single guest (i) being transported towards the growing surface. The cluster is adsorbed onto the crystal surface (ii) releasing one of the water molecules in the cluster. The cluster is not locked on the crystal surface, but diffuses along the surface (iii) until it is attached to a crystal layer at a step (iv) on the surface. At this step, the cluster releases another solvent molecule, and can only move in one dimension, until a kink (a surface with three or more edges) is found (v). At the kink, the cluster is immobile in three dimensions, and several solvent molecules are released (vi). (Note that this is hypothesis without evidence from hydrate growth experiments.)(Elwell & Scheel, 1975)

The hydrocarbon hydrate formers have low mutual solubility in water; the crystal growth appears at the liquid-gas interface, where the gas saturation is at maximum or super saturation level. (Long, 1994)

2.2.2 Boundary layer

All modern crystal growth models of hydrates include mass transfer, particularly from the bulk phase to the hydrate. (E. Dendy Sloan & Koh, 2008)

"Diffusional boundary theory" model (Bird, Stewart, & Flightfoot, 1960) is well-established and modified several times, especially on physical evidence for the existence of the boundary layer (Berg, 1938; Bunn, 1949). Modification on the former model were done by Berthoud and Valeton (Berthoud, 1912; Valeton, 1924), where they included two steps; diffusion to the interface, and reaction at the interface.

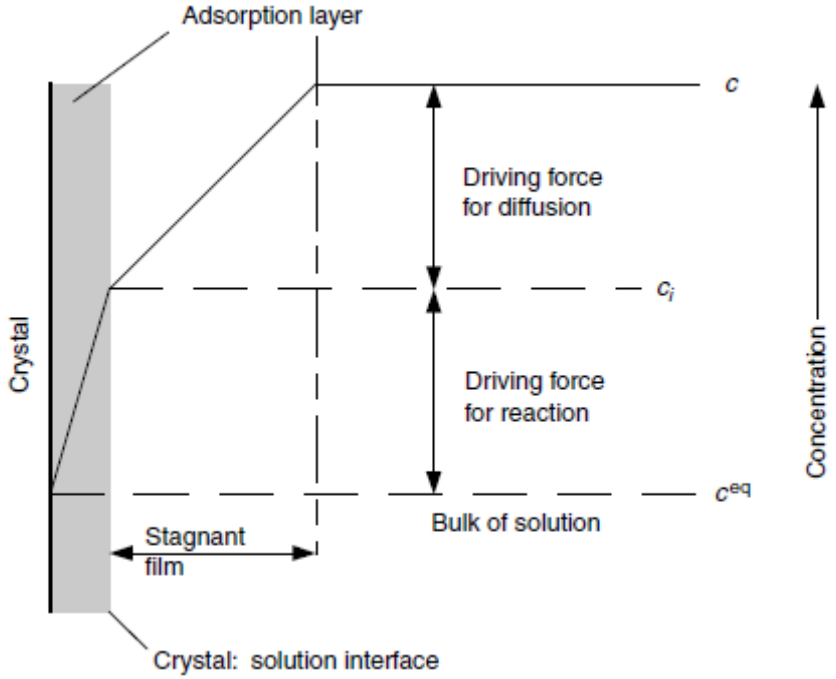

Figure 4: Conceptual model of mass transfer from bulk to liquid phase. (E. Dendy Sloan & Koh, 2008)

A model based on a stagnant boundary layer is shown in Figure 4. This boundary layer exists on the fluid side of the crystal interface. The interfacial concentration is difficult to measure, therefore a concentration gradient within the fluid, is equal to the bulk fluid concentration minus the interfacial concentration. (The concentration differences are expressed as driving force.)(E. Dendy Sloan & Koh, 2008)

The crystallization is mainly controlled by mass transfer when the reaction is very rapid related to diffusion, only. On the other hand when diffusion is more rapid than the reaction, the reaction coefficient controls the crystallization.(E. Dendy Sloan & Koh, 2008)

Hydrate growth can be limited by an increase in temperature within the bulk phase which causes a local drop in subcooling, e.g. when using an experimental cell setup. (Meindinyo et al., 2014b)

2.2.3 Single crystal growth

The hydrate crystal growth can be divided into four different groups (E. Dendy Sloan & Koh, 2008):

1. Single crystal growth
2. Hydrate film/shell growth at the water-hydrocarbon interface
3. Multiple crystal growth in an agitated system
4. Growth of metastable phases

(1)Single crystal growth of hydrates is a useful method to investigate the effect of additives on hydrate crystal growth and morphology. (E. Dendy Sloan & Koh, 2008)

.

Larsen et al. believe that the most probable mechanism in the step creation, in single crystal growth, is surface nucleation. (Larsen et al., 1998)

Normally, it is difficult to study crystal hydrate growth of natural gas hydrates, but hydrates of miscible solution, such as THF and EO hydrates (see Figure 5), can easily be grown and isolated for structural analysis, since there is mass transfer in the bulk phase, only.(T. Y. Makogon et al., 1996) The observations, visually, is the slowest growing plane, only (Mullin, 1993). (111) and (110) is the slowest growing planes for THF and EO, respectively (Larsen et al., 1998; T. Y. Makogon et al., 1996).

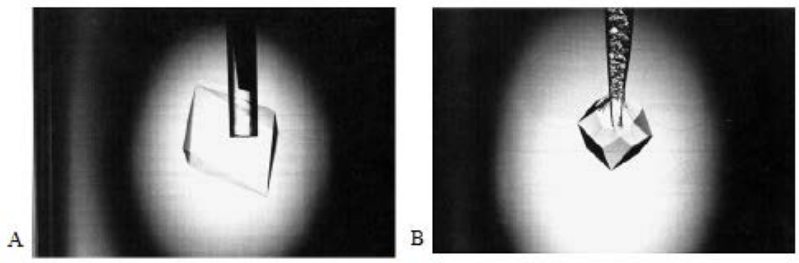

Figure 5: Photo of single hydrate crystals of (A) THF (sII), and (B) EO (sI). (Larsen et al., 1998)

Methane and EO crystals form sI and have been under same consideration when it comes to hydrate growth: crystallization and inhibition. This means that the growth habits are the same. (Larsen, Knight, Rider, & Sloan Jr., 1999)

(2)Hydrate growth is typically initiated at the water–hydrocarbon interface. Realistic hydrate growth models can be produced by use of measurements on growth of hydrate film/shell. (E. Dendy Sloan & Koh, 2008)

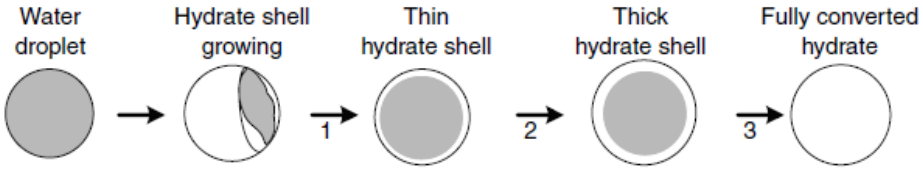

Figure 6: A schematic illustration of the proposed mechanism for hydrate formation from a water droplet to hydrate. (Taylor, 2006)

Servio and Englezos suggested this formation process of hydrates: "water droplets to hydrate particle". This growth process is analog to film growth occurring on a planar water-hydrocarbon surface (see Figure 6). (Englezos & Servio, 2003) The mechanism shown in figure 6 can be studied by use of "Micro-imaging". (E. Dendy Sloan & Koh, 2008)

(3)Crystal growth with interfacial agitation can be formed in a stirring reactor where gas consumption is a function of time. Bishoni laboratory has done a lot research on interfacial crystal growth. (Englezos & Bishnoi, 1988; Englezos et al., 1987a, 1987b)

(4)Metastable phases during hydrate growth can be detected by Raman and NMR spectroscopy, Neutron – and X-ray diffraction. The molecular mechanisms of hydrate growth and the possible origin of thermodynamic structural transitions are able to predict by the appearance of metastable phases during hydrate growth. (E. Dendy Sloan & Koh, 2008)

2.2.4 Models and correlation of macroscopic crystal growth

Table 3 shows a list of all the developed hydrate growth models, by different research groups. Three major correlations for hydrate growth exist:

1. Intrinsic growth kinetics

2. Mass transfer limited
3. Heat transfer limited

Table 3 List of hydrate growth models (E. Dendy Sloan & Koh, 2008)

Growth model	Driving force/model features	Researchers
Growth kinetics	$(f - f_{eq})$	(Englezos et al., 1987a,b)
Growth kinetics	$(f - f_{eq})$ Minor modification to Englezos' model	(Malegaonkar et al., 1997)
Mass transfer	$(x^i_{int} - x^i_b)$ Simplification/modification to Englezos' model	(Skovborg and Rasmussen, 1994)
Mass transfer	Based on phase field theory	(Svandal et al., 2005)
Mass transfer	Based on Monte Carlo cellular automata	(Buanes et al., 2005)
Heat transfer	Curved film front growth on water–hydrate former interface	(Uchida et al., 1999a)
Heat transfer	Curved film front growth on water–hydrate former fluid interface	(Mori, 2001)
Heat transfer	Straight film front growth on water side of water–hydrate former interface	(Freer et al., 2001; Mochizuki and Mori, 2005, 2006)

2.2.4.1 Intrinsic kinetics – the Englezos - Bishnoi model

Heat and mass transfer effects play a major role in hydrate intrinsic growth kinetics, compared to hydrate growth in real system which is suggested to play an insignificant role. (E. Dendy Sloan & Koh, 2008)

A three step kinetic growth process is suggested/assumed by Englezos and Bishnoi (It is further modified by Malegoankar)(Englezos et al., 1987a, 1987b; Malegoankar, Dholabhai, Bishnoi, & Can, 1997):

1. Transport of gas from vapor to liquid phase
2. Diffusion of gas around hydrate particles
3. Adsorption of gas at the hydrate interface

The rate of growth per particle based on step (2) and (3) is given in eq. (1):

$$\left(\frac{dn_i}{dt}\right)_p = K^* A_p \left(f_i^b - f_i^{eq}\right) \text{ and } \frac{1}{K^*} = \frac{1}{k_r} + \frac{1}{k_d} \qquad \textbf{(1)}$$

Where, $(dn_i/dt)_p$ is the number of moles of gas consumed pr. second by the hydrate; A_p [m^2] is the surface area of each particles; f_i^b and f_i^{eq} [Pa] are fugacity of component i in the bulk phase and in the liquid at hydrate equilibrium, respectively; K^* is the hydrate formation growth constant; k_r and k_d is the reaction rate constant and mass transfer coefficients through the film around the particle, respectively. The overall driving force is $f_i^b - f_i^{eg}$.

This model does not take into consideration the transport of the gas from the vapor phase into the liquid phase, and then trough the bulk towards the particle, and has its limitations. (E. Dendy Sloan & Koh, 2008)

2.2.4.2 Mass transfer limited growth – the Skovborg - Rasmussen model

Skovborg and Rasmussen noted two restrictions in addition to limitations (2), and (3) in Englezos and Bishnoi`s model. These restrictions are as follows (Skovborg & Rasmussen, 1994):

1. The secondary nucleation can be neglected since the secondary nucleation constant was found very low. Skovborg and Rasmussen suggested then that the crystallization population balance could be removed from the model.
2. The mass transfer coefficient K_L (through the liquid film) affects the K*, so that the value of K* may have been too high. Skovborg noted that 50 % error in K_L will result in an error: K* in an order of two.

They, Skovborg and Rasmussen, assumed that the entire hydrate formation can be modeled as a mass transfer restriction, gas through liquid film at the gas-liquid interface (see eq. 2) (Skovborg & Rasmussen, 1994)

$$\frac{dn}{dt} = k_L A_{(g-1)} c_{wo} (x_{int} - x_b) \qquad \textbf{(2)}$$

Where, $A_{(g-1)}$ is the area of the gas-liquid interface; c_{wo} is the initial concentration of water; x_{int} and x_b are the molefraction at the bulk-liquid interface and bulk phase, respectively; dn is the number of moles gas consumed at the time step dt.

Sloan (E. Dendy Sloan & Koh, 2008) suggested that there are limitations within the Skovberg and Rasmussen model, and that all model descriptions should be studied carefully and used with caution

Skovborg re-analyzed the Englezos kinetic data and obtained mass transfer coefficients for methane and ethane. (Skovborg & Rasmussen, 1994)

2.2.4.3 Heat transfer limited growth – several models

All the heat transfer models represented here (Figure 7), assume that rate of hydrate growth is proportional to the rate of heat removal from the hydrate film. (E. Dendy Sloan & Koh, 2008)

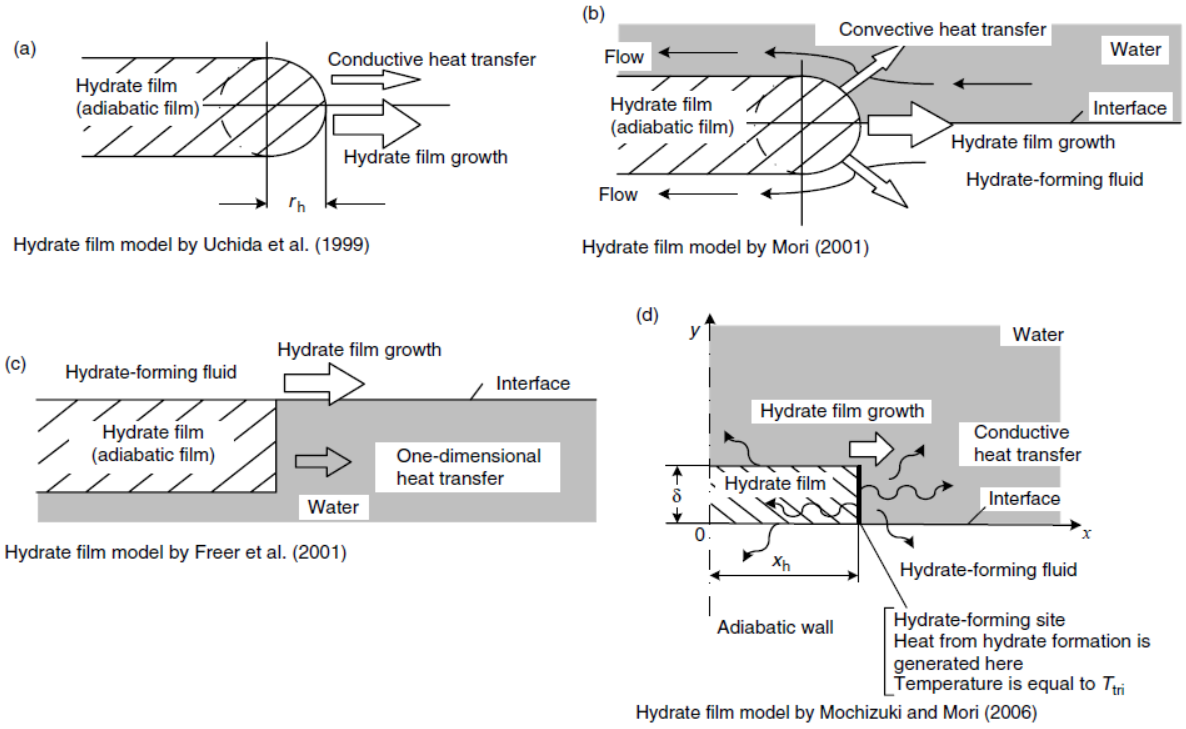

Figure 7: Physical models of hydrate film growth along the water-hydrate former fluid interface. (Mochizuki & Mori, 2006)

The model by Uchida et al (Uchida et al., 1999a) (Figure 7a) is based on hydrate crystals growth at the front of the hydrate film, only, and the front is maintained at the three phase (water – guest – hydrate).It is assumed steady heat transfer from the front to the water and guest fluid.

In 2001 there were suggested two models on lateral hydrate film growth; Mori(Mori, 2001) (Figure 7b) and Freer et al. (Freer, Selim, & Sloan, 2001) (Figure 7c) which is based on lateral growth of the hydrate film on the interface between a stagnant water pool & a guest fluid and experimental data on methane hydrate film growth at the methane-water interface, respectively.

Mochizuki and Mori suggested that the major problem with Uchida et al model was that the conductive heat transfer formulation. They found that Mori`s model has unrealistic countercurrent convections, since hydrate mass density is very small similar to water. This model (Figure 7d) is based on an assumption: transient two dimensional convective heat transfer from the film front through both water and guest fluid phases and the hydrate film itself. The hydrate film exists at the water side of the water-guest fluid interface (as Freer et al model). (Mochizuki & Mori, 2005, 2006)

$$\rho_h \delta \Delta h_H v_f = \int_0^{\delta} (\lambda_h \frac{\partial T}{\partial x}|_{x=x_{h-}} - \lambda_w \frac{\partial T}{\partial x}|_{x=x_{h+}}) dy \qquad (3)$$

Where, δ is hydrate thickness; $\partial T/\partial x|_{x=xh-}$ and $\partial T/\partial x|_{x=xh+}$ are the hydrate side and water-side temperature gradients, respectively; $x=x_h$ is the x position at the hydrate-film front; Δh_H is the heat formation pr. unit mass of hydrate; λ_h and λ_w [W/m K] is the thermal conductivity of hydrate and water, respectively; vf is the linear growth rate of the hydrate film; ρ_H [m^3/kg] is the density of hydrate.

Eq. 3 show a linear growth rate of the hydrate film, calculated by Mochizuki and Mori (Mochizuki & Mori, 2005, 2006).

Makogon (Y. Makogon, Makogan, & Holditch, 1998) and Taylor (Taylor, Dieker, Miller, Koh, & Sloan, 2006) compared Freer et al. and Mochizuki & Mori model, and saw that the calculations and the experimental data of methane was similar due to each other.

2.2.4.4 Driving force

The key of hydrate nucleation correlation is the driving force, normally in term of fugacity (see Table 4). The isothermal driving force for a general case is said to be isobaric equivalent with the subcooling driving force.(E. Dendy Sloan & Koh, 2008)

Christiansen and Sloan (Christiansen & Sloan Jr, 1994) shows that all the driving forces in nucleation, in general, follows a driving force in terms of Gibbs free energy.

Table 4: A list of different driving forces for the nucleation process(E. Dendy Sloan & Koh, 2008)

Different Driving Forces Used for Nucleation

Investigators	Year	Driving force
Vysniauskas and Bishnoi	1983b	$T^{eq} - T^{exp}$
Skovborg and Rasmussen	1992	$\mu_{WH}^{exp} - \mu_{WL}^{exp}$
Natarajan et al.	1994	$f_i^{exp}/f_i^{eq} - 1$
Christiansen and Sloan	1995	Δg^{exp}
Kashchiev and Firoozabadi	2002	$\Delta\mu$, supersaturation
Anklam and Firoozabadi	2004	Δg
Arjmandi et al.	2005b	$T^{eq} - T^{exp}$

Arjmandi et al. (Arjmandi, Ren, & Tohidi, 2005) reviewed previous work and investigated how the pressure affected the driving force. They noted that the driving force decreased with increasing pressure at constant subcooling, in general, for a system having pressures above 20MPa. The driving force was underestimated when having pressures between 5-20MPa.

When having high driving force present in the system hydrates can be formed at many different locations, compared to a system with low driving force present, where the hydrate formation is more regularly located. (Some say that the supersaturation (driving force) is independent of the hydrate formation.)(E. Dendy Sloan & Koh, 2008)

2.3 Hydrate dissociation

By depressurization, thermal stimulation, thermodynamic inhibitor injection, or a combination of these methods hydrate dissolves. In gas production hydrate dissociation is of key importance. (E. Dendy Sloan & Koh, 2008)

Radial hydrate dissociation is suggested to be more rapid than the axial hydrate dissociation (i.e. dissociation of a hydrate plug is based on heat-transfer limited dissociation where the hydrate remains in the center and is surrounded by water.) (Davies, Selim, Sloan, Bollavaram, & Peters, 2006; E. Dendy Sloan & Koh, 2008) The comparison of radial and axial hydrate dissociation is shown in Figure 8.

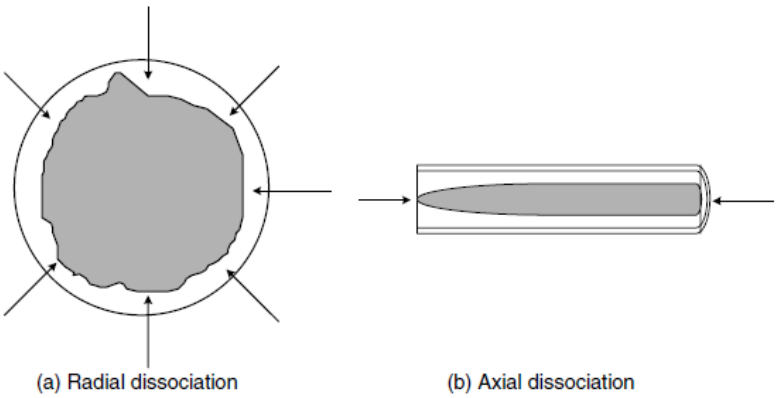

Figure 8: Hydrate dissociation: (a) in radial direction, (b) in axial direction. (E. Dendy Sloan & Koh, 2008)

A hydrate dissociation process consist of three phenomena ((E. Dendy Sloan & Koh, 2008):

1. Heat transfer to the hydrate-fluid phase
2. Kinetic dissociation
3. The fluid flow (gas and water) away from the interface

Table 5: A summary of hydrate dissociation models (Hong, Pooladi-Darvish, & Bishnoi, 2003).

	Heat transfer		Fluid flow			Solution
Model	Conduction	Convection	Gas	Water	Kinetics	Method
Holder and Angert (1982)	X		X			Numerical
Burshears et al. (1986)	X		X	X		Numerical
Jamaludin et al. (1989)	X				X	Numerical
Selim and Sloan (1989)	X	X	X			Analytical
Yousif and Sloan (1991)			X	X	X	Numerical
Makogon (1997)	X	X	X	X		Analytical
Tsypkin (2000)	X	X	X	X		Analytical
Masuda et al. (2002)	X	X	X	X	X	Numerical
Moridis et al. (2002)	X	X	X	X	X	Numerical
Pooladi-Darvish et al. (2003)	X	X	X	X	X	Numerical

Table 5 indicated that all three phenomena are involved in the model of the last decade. It is also stated if the model has an analytical or a numerical solution.

It is shown that heat transfer plays a major role in hydrate dissociation rather than intrinsic kinetics. (Davies et al., 2006; Hong et al., 2003; Moridis, 2002)
Hong et al.(Hong et al., 2003) suggested that intrinsic kinetics controlling the very early stage of hydrate dissociation and the later stages is controlled by heat transfer.

An analytical study (Hong & Pooladi-Darvish, 2005) suggested that convective heat transfer, kinetics and fluid flow are least dominant in hydrate dissociation, if kinetics are dominant the kinetic rate need to be reduced in an order of 2. The controllable factor in hydrate dissociation is conductive heat transfer.

Rehder et al. (Rehder et al., 2004) measured dissociation rates of hydrates (methane and carbon dioxide) in seawater, and it is shown that the hydrate dissociation is caused by difference in concentration of the guest molecule in both the surface and the bulk of the hydrate.

2.4 Heat transfer

All models outlined in the previous section describe hydrate formation and growth at a microscopic level or at the surface of individual growing particles. In the present work, the global system is treated regarding all the particles as part of the same mass. The gas consumed in the system gives rise to heat release, and the total heat balance will be between heat produced and the heat lost to the surroundings (i.e. cooling water).

2.4.1 Heat transfer in laboratory stirred cell system

According to Runar Bøe (assoc. professor at Dept. of Petroleum Engineering at UiS) (Boe, 2014):

The conducted cells used, in this present work, are all cylindrical with internal stirring and external cooling (see section 3 for outline and description). The heat transfer model used is based on the following assumption: The total heat transfer of the cell/system must be the same across all the boundaries in radial direction, thus we can simplify the system by looking at the effect of the heat transfer coefficient at the inner boundary layer between the wall and the water bulk phase only, and the temperature differences across the cell.

In a stirred cell system without any hydrates present the boundary layer at inner surface will be a function of the fluid flow along the surface (i.e. a function of the stirring rate).

With hydrates in the cell the heat transfer at the inner boundary layer will be affected by the continuous hydrate formation process and this will result in an altering concentration at the layer which will affect its heat transfer properties (i.e. suspended particles versus particles precipitated on the wall).

The illustration in Figure 9 shows how the temperature profiles from the interior of the cell (left hand side of Figure 9A) across the cell wall (shaded area in the middle of figure 9A), and to the cooling water on the outside of the cell (right hand of Figure 9A). Figure section B shows a view through the cell from the top side. The total heat flow described: the heat flow in both coolant (out of the cell) and the cell interior (into the cell) is convectional and conductional heat flow through the cell wall itself. In some cases, when having a solid hydrate

film at the cell wall, there can be assumed conductional heat transfer through this layer at the interior cell wall. The analytical solution of this system is showed in section 2.6.7.2, and appendix B.3.

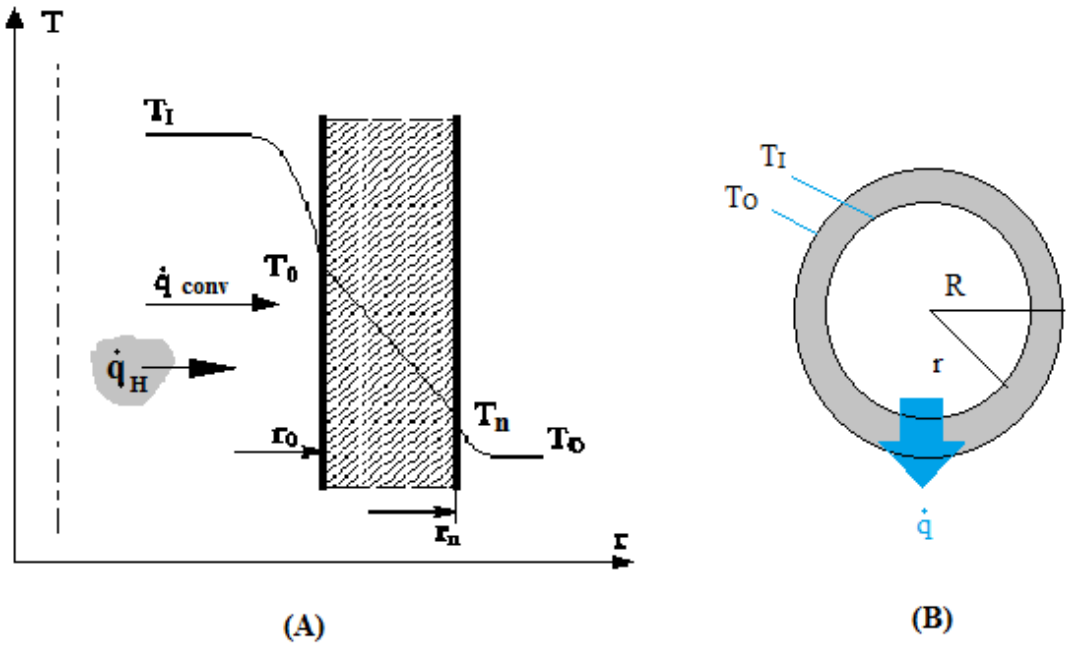

Figure 9: Illustration of heat transfer in a cylindrical cell; (A) through the outer wall into the cell interior having a hydrate slurry (Meindinyo et al., 2014a) , and (B) through the cell wall (Nordboe, 2013). (The geometry is according to figure 14.)

In general heat transfer requires knowledge of energy balance, momentum equations, fluid dynamics, and boundary layer analysis (Holman, 2010). Conductional heat transfer is when molecules are emitted from high to low temperature to produce energy, while convectional heat transfer is heat transfer through a flowing medium (Borgnakke & Sonntag, 2009). Whenever there is a fluid flow over a surface a velocity boundary layer will be developed, which is highly important in convectional transport. (Incropera, DeWitt, Bergman, & Lavine, 2007)

The overall convectional heat transfer (by Newton`s law of cooling) (eq. 4) in a pipe (Holman, 2010):

$$Q = hAdT = hA(T_w - T_\infty) \qquad (4)$$

Where, Q is the heat flux in a pipe [W/m^2]; h is the heat transfer coefficient [W/m^2 K]; T_w and T_∞ is the surface temperature near the wall, the temperature in the bulk/fluid phase [K], respectively; A is the area [m^2].

The conductional energy equation (by Fourier`s law) (eq. 5) in a pipe (Kaviany, 2002):

$$\boldsymbol{q} = -\lambda A \frac{dT}{dx} \qquad \textbf{(5)}$$

Where, **q** is conductional heat flux in a pipe [W/m^2]; A is area [m^2]; λ is thermal conductivity [W/m K]; dT is the temperature difference between the wall and the bulk phase [T]; dx is the length difference of the pipe [m].

The heat transfer coefficient (HTC) is a function of media properties, the flow and the geometry. (Borgnakke & Sonntag, 2009), and the momentum transfer is dependent of the molecular movements across the fluid. (Holman, 2010) The fluid is said to store heat better when the value of HTC is small (Incropera et al., 2007).

The model used is based on both conduction and convection and also use of cylindrical coordinates (see Figure 9 and 10), the equation for the system of hydrate will look like:

$$\boldsymbol{q_R} = (m_w C_w + m_H C_H + N_g C_{p,g}) \frac{\partial T}{\partial t}\Big|_I + h_I A_O (T_I - T_O) \qquad \textbf{(6)}$$

Where, $\mathbf{q_R}$ is the heat flux of the hydrate slurry [W/m^2]; m_w and m_H is the mass of water and solute (THF or EO)[kg]; Ng is the number of moles of the gas (air); C_w, C_H and $C_{p,g}$ [J/kg] is the specific heat capacity at constant pressure for water, the solute (THF or EO) and gas, respectively; h_I is the inner heat transfer coefficient [W/m^2 K];A_O is the outer surface area [m^2]; T_I and T_O [K] is the temperature of the inner and outer boundary, respectively.

The input parameters:

1. HTC for both water/cell and coolant water/cell interface
2. Heat conductivity for both cell and solution (THF or EO)
3. The number of moles of THF or EO and air
4. Enthalpy for the whole system

Major assumptions:

1. Radial system (see Figure 9B and 10, and also equation 7)
2. Transient heat transfer
3. No hydrate generation (assume the amount of hydrate is constant, $\mathbf{q_r} = 0$)
4. Inner and outer HTCs (h_I and h_O, respectively) are assumed constant, and relative to the entire heat transfer areas.

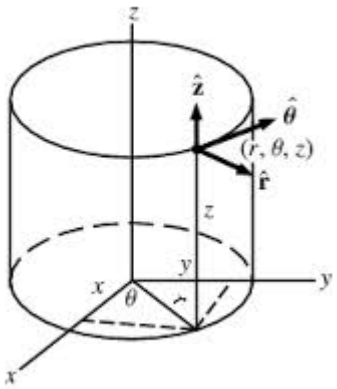

$$0 \leq \theta \geq 2\pi$$
$$0 \leq r \geq R$$
$$0 \leq z \geq L_z$$

Figure 10: Cylinder Coordinates

To be able to calculate the heat transfer in a system with hydrate present, it is necessary to start out with: heat diffusion equation with constant material properties, and no generation term (eq. 7):

$$\frac{1}{r}\frac{\partial}{\partial r}\left(r\frac{\partial T}{\partial r}\right) = \frac{1}{\alpha}\frac{\partial T}{\partial t} \qquad \textbf{(7)}$$

Where, r is the inner radius; T is temperature; t is the time; α is the thermal diffusivity.

Eq. 7 is only a basic equation. From here it is necessary to use the method of discretization by use of backward difference or forward difference on the right hand side (the term with change in time (t)) for implicit or explicit discretization, respectively, and central difference (Figure 11) on left hand side (the term with change in space (r)).

There will also only be needed 3 nodes, see picture below:

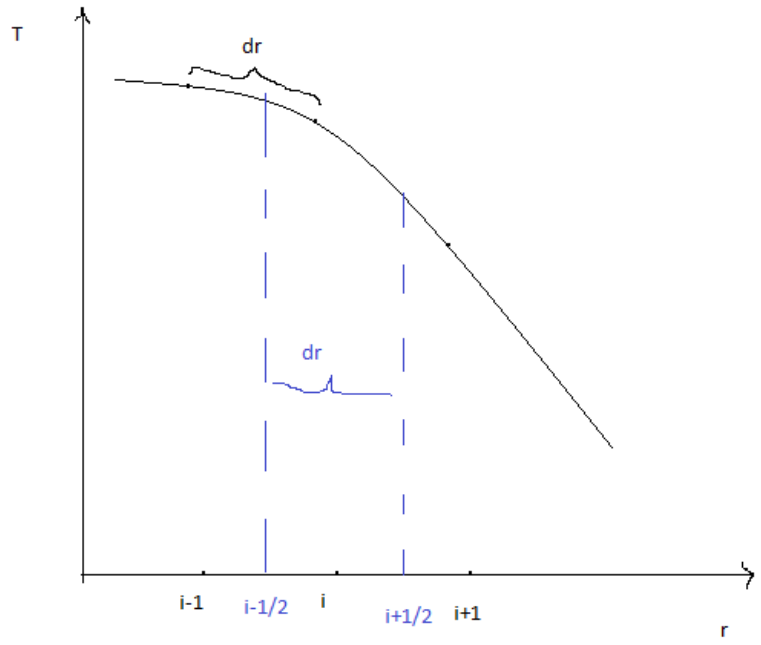

Figure 11: Discretization, in terms of central difference, by use of three nodes

2.4.1.1 Explicit method on a system without hydrate generation

When having an equation in explicit form, the time steps are in present time. (Incropera et al., 2007)

The given equation will be calculated from eq. 7:

Heat transfer equation by explicit discretization (eq.8):

$$\frac{T_i^{p+1} - T_i^p}{\Delta t} = \alpha \cdot \left(\frac{T_{i+1} - 2T_i + T_{i-1}}{(\Delta r)^2} + \frac{1}{2}\frac{T_{i+1}T_{i-1}}{r_i \Delta r}\right) \quad \textbf{(8)}$$

When using eq. 6 - 8 on a system with hydrate present, the equation 8 will be modified:

$$q_R = (m_w C_w + m_H C_H + N_g C_{p,g}) \frac{T_1^{p+1} + T_I^p}{\Delta t} + h_I A_O (T_I^p - T_O^p) \quad \textbf{(9)}$$

The cell interior when having hydrate generation (eq. 10):

$$T_1^{p+1} = X_I - C_I \cdot (T_I^p - T_O^p) + T_I^p \quad \textbf{(10)}$$

Where:

$$X_I = \frac{q_R \cdot \Delta t}{m_w \cdot c_w + m_H \cdot c_H + N_{air} \cdot c_{p,air}} \quad \textbf{(11)}$$

$$C_I = \frac{2h_I(\pi\delta r_O)\cdot\Delta t}{m_W \cdot c_W + m_H \cdot c_H + N_{air} \cdot c_{p,air}} \quad \textbf{(12)}$$

Cell interior without hydrate generation ($\mathbf{q_r}$ = 0 and therefore X_I = 0) (eq. 13):

$$T_1^{p+1} = \frac{2h_I(\pi\delta r_O)\cdot\Delta t}{m_W \cdot c_W + m_H \cdot c_H + N_{air} \cdot c_{p,air}} \cdot (T_I^p - T_O^p) + T_I^p \quad \textbf{(13)}$$

Inner border (i =0) (eq. 14):

$$T_O^{p+1} = \frac{2h_I\Delta t}{\rho c \Delta r}(T_I^p - T_O^p) + \frac{2\alpha\Delta t}{r_O(\Delta r)^2} \cdot \left(r_O + \frac{\Delta r}{2}\right)(T_I^p - T_O^p) + T_O^p \quad \textbf{(14)}$$

Interior node (i) (eq. 15)

$$T_i^{p+1} = T_i^p + \frac{\alpha\Delta t}{(\Delta r)^2} \cdot (T_{i+1}^p - 2T_i^p + T_{i-1}^p) + \frac{2\alpha\Delta t}{2r_i\Delta r} \cdot (T_{i+1}^p - T_{i-1}^p) \quad \textbf{(15)}$$

Outer border (i=n) (eq. 16):

$$T_n^{p+1} = \frac{2h_O\Delta t}{\rho c \Delta r}(T_O^p - T_n^p) - \frac{2\alpha\Delta t}{r_n(\Delta r)^2} \cdot \left(r_n + \frac{\Delta r}{2}\right)(T_n^p - T_{n-1}^p) + T_n^p \quad \textbf{(16)}$$

Where, ρ is density; c is specific heat capacity, t is time, α is thermal diffusivity, r is the radius; N is number of moles; m is the mass [kg]; X_I [K] is the temperature equivalent for heat of generation; C_I is the dimensionless parameter of the cell interior; h_I and h_O (always parameterized)[W/m^{2}K] is the inner and outer heat transfer coefficients, respectively ; $T_i^{p+1}$is the current nodal in wall temperature profile (always unknown); T_0^{p+1} is the current temperature of inner wall (always unknown); T_n^{p+1} is the current temperature of outer wall (always unknown); T_I^{p+1} is the current temperature of the cell content (treated as unknown); T_O^{p+1} is the current cooling water temperature (measured), where temperature (T) has a unit of degrees Kelvin [K].

2.4.1.2 Implicit method on a system without hydrate generation

The time steps are in future time. The equation has a high number of unknowns, present here. The implicit method is unconditionally stable; remains stable for all space and time intervals, and is compatible with the stability requirements).(Incropera et al., 2007)
Note: conduction at the interior node, and convection at the border nodes.

The given equation will be calculated from eq. 7:
Heat transfer equation by implicit discretization (eq.17):

$$\frac{T_i^{p+1} - T_{\square}^{p}}{\Delta t} = \alpha \cdot \left(\frac{T_{i+1}^{p+1} - 2T_i^{p+1} + T_{i-1}^{p+1}}{(\Delta r)^2} + \frac{1}{2}\frac{T_{i+1}^{p+1} T_{i-1}^{p+1}}{r_i \Delta r}\right) \qquad \textbf{(17)}$$

This method requires use of “Gauss-Seidel iteration” or “matrix inversion” to be able to calculate the unknown variables that comes when using future time steps. (Incropera et al., 2007) It is used “matrix inversion” in this case (Runar Bøe):

The entire equation (eq.18):

$$\boldsymbol{A \cdot T = Y} \qquad \textbf{(18)}$$

Matrix A (eq. 19):

$$\boldsymbol{A} = \begin{bmatrix} a_{I,I} & \cdots & a_{I,n} \\ \vdots & \ddots & \vdots \\ a_{n,I} & \cdots & a_{n,n} \end{bmatrix} \qquad \textbf{(19)}$$

Matrix T (eq. 20):

$$\boldsymbol{T} = \begin{bmatrix} T_I \\ T_0 \\ T_1 \\ \vdots \\ T_n \end{bmatrix} \qquad \textbf{(20)}$$

Matrix Y (eq. 21):

$$\boldsymbol{Y} = \begin{bmatrix} {T_I}^p \\ {T_0}^p \\ {T_1}^p \\ \vdots \\ y_n \end{bmatrix} \quad \textbf{(21)}$$

eq. 18 in terms of matrix T (eq. 22):

$$\boldsymbol{T} = \boldsymbol{A}^{-1} \cdot \boldsymbol{Y} \quad \textbf{(22)}$$

Calculation of matrix A (eq. 23):

$$\boldsymbol{A} = \begin{bmatrix} (1+C_I) & -C_I & 0 & 0 & 0 & 0 & 0 & 0 \\ -2Bi_IFo & \left(1+2\left[Bi_I+\left(\frac{\Delta r}{2r_O}+1\right)\right]Fo\right) & -2\left(\frac{\Delta r}{2r_O}+1\right)Fo & 0 & 0 & 0 & 0 & 0 \\ 0 & \left(\frac{\Delta r}{2r_1}-1\right)Fo & (1+2Fo) & -\left(\frac{\Delta r}{2r_1}+1\right)Fo & 0 & 0 & 0 & 0 \\ 0 & 0 & \left(\frac{\Delta r}{2r_2}-1\right)Fo & (1+2Fo) & -\left(\frac{\Delta r}{2r_2}+1\right)Fo & 0 & 0 & 0 \\ 0 & \vdots & \vdots & \vdots & \ddots & \vdots & \vdots & \vdots \\ 0 & 0 & 0 & 0 & \left(\frac{\Delta r}{2r_{n-1}}-1\right)Fo & (1+2Fo) & -\left(\frac{\Delta r}{2r_{n-1}}+1\right)Fo & 0 \\ 0 & 0 & 0 & 0 & 0 & 2\left(\frac{\Delta r}{2r_n}-1\right)Fo & \left(1+2\left[Bi_O-\left(\frac{\Delta r}{2r_n}-1\right)\right]Fo\right) & 0 \end{bmatrix} \quad \textbf{(23)}$$

Matrix Y in a hydrate system (eq. 24):

$$\boldsymbol{Y} = \begin{bmatrix} {T_I}^p \\ {T_0}^p \\ {T_1}^p \\ {T_2}^p \\ \vdots \\ {T_{n-1}}^p \\ {T_n}^p + 2Bi_OFo \cdot {T_O}^{p+1} \end{bmatrix} \quad \textbf{(24)}$$

When calculating the heat of formation by use of implicit method the principle used in explicit method (see eq. 13) can also be used here:

Cell interior (eq. 25):

$$C_I \cdot {T_0}^{p+1} = (1+C_I) \cdot {T_I}^{p+1} - {T_I}^p \rightarrow (1+C_I) \cdot {T_I}^{p+1} - C_I \cdot {T_0}^{p+1} = {T_I}^p \quad \textbf{(25)}$$

Inner border (i =0) (eq. 26):

$$1+2\left[Bi_I+\left(\frac{\Delta r}{2r_O}+1\right)\right]Fo \cdot {T_0}^{p+1} - 2\left(\frac{\Delta r}{2r_O}+1\right)Fo \cdot {T_1}^{p+1} = {T_0}^p + 2Bi_IFo \cdot {T_I}^{p+1} \quad \textbf{(26)}$$
$$\rightarrow -2Bi_IFo \cdot {T_I}^{p+1} + 1 + 2\left[Bi_I+\left(\frac{\Delta r}{2r_O}+1\right)\right]Fo \cdot {T_0}^{p+1} - 2\left(\frac{\Delta r}{2r_O}+1\right)Fo \cdot {T_1}^{p+1} = {T_0}^p$$

Interior node (i) (eq. 27):

$$\left(\frac{\Delta r}{2r_i}-1\right)Fo\cdot {T_{i-1}}^{p+1}+(1+2Fo)\cdot {T_i}^{p+1}-\left(\frac{\Delta r}{2r_i}+1\right)Fo\cdot {T_{i+1}}^{p+1}={T_i}^{p} \quad (27)$$

Outer border (i=n) (eq. 28):

$$2\left(\frac{\Delta r}{2r_n}-1\right)Fo\cdot {T_{n-1}}^{p+1}+(1+2[Bi_O+(\frac{\Delta r}{2r_n}-1)]Fo)\cdot {T_n}^{p+1}={T_n}^{p}+2Bi_OFo\cdot {T_O}^{p+1} \quad (28)$$

Where, ρ is density; c is specific heat capacity, t is time, α is thermal diffusivity, r is the radius; N is number of moles; m is the mass [kg]; X_I [K] is the temperature equivalent for heat of generation; hI [W/m^{2}K]and hO (always parameterized)[W/m^{2}K] is the inner and outer heat transfer coefficients, respectively ; $T_i^{p+1}$is the current nodal in wall temperature profile (always unknown); T_0^{p+1} is the current temperature of inner wall (always unknown); T_n^{p+1} is the current temperature of outer wall (always unknown); T_I^{p+1} is the current temperature of the cell content (treated as unknown); T_O^{p+1} is the current cooling water temperature (measured); Fo is the fourier number; Bi is the Biot number. Temperature (T) has a unit of Kelvin degrees [K].

2.4.2 Methane hydrate

Heat transfer during growth of methane hydrate was done by Remi- E. Meindinyo (Meindinyo et al., 2014b). This study showed that the estimated HTC decreased with increasing concentration of methane hydrate in slurry.

2.4.3 Condensation process

The overall HTC of water in a steam chamber is increasing with increase in the rotational speed, when have horizontal cylinders. (But at very high rotational speed the HTC decreases) (Singer & Presckshot, 1963). In vertical cylinders the overall HTC increases with increase in rotational speed (Nicol & Gacesa, 1970).

A phenomenon called “Laminarization” happens when the flow regime changes from fully transient to laminar – like. This causes reduction in the HTC with increasing rotational speed (Hirai, Takagi, & Matsumoto, 1988).

Increase in overall HTC means increase in convectional HTC, caused by reduction of the condensate film thickness (Mohamed, 2006).

2.4.4 Rotational speed

Convection is affected by fluid motion, so in a fluid, the increase in stirring rate increase the HTC (i.e lower values of the HTC means more conduction (isolated system)) (Borgnakke & Sonntag, 2009; Incropera et al., 2007).

The rate of the heat is dependent of the stirring rate, when having a system with miscible solution of THF and water (Bollavaram, Devarakonda, Selim, & Sloan Jr, 2000).

An analytical solution by Rao et al.(Rao, Sloan, Koh, & Sum, 2011) showed that decrease in velocity of the fluid is caused by the increase in the hydrate thickness.

3 EQUIPMENT AND PROCEDURE/METHOD

Experiments have been conducted in 2 titanium cells (cell #0 and cell #5), and in sapphire cells (cell #1, cell #2). In the sapphire cells there have only been done observations on how the THF -, and EO –hydrates look like (i.e. thickness and structure). The experiments regarding the heat transfer coefficients have been done in both cell #0 and cell #5.

3.1 Equipment

In this thesis experiments have been conducted in different cells, in both Titanium and Sapphire cells. The connecting system of the cell is the same in every single case. It looks like this:

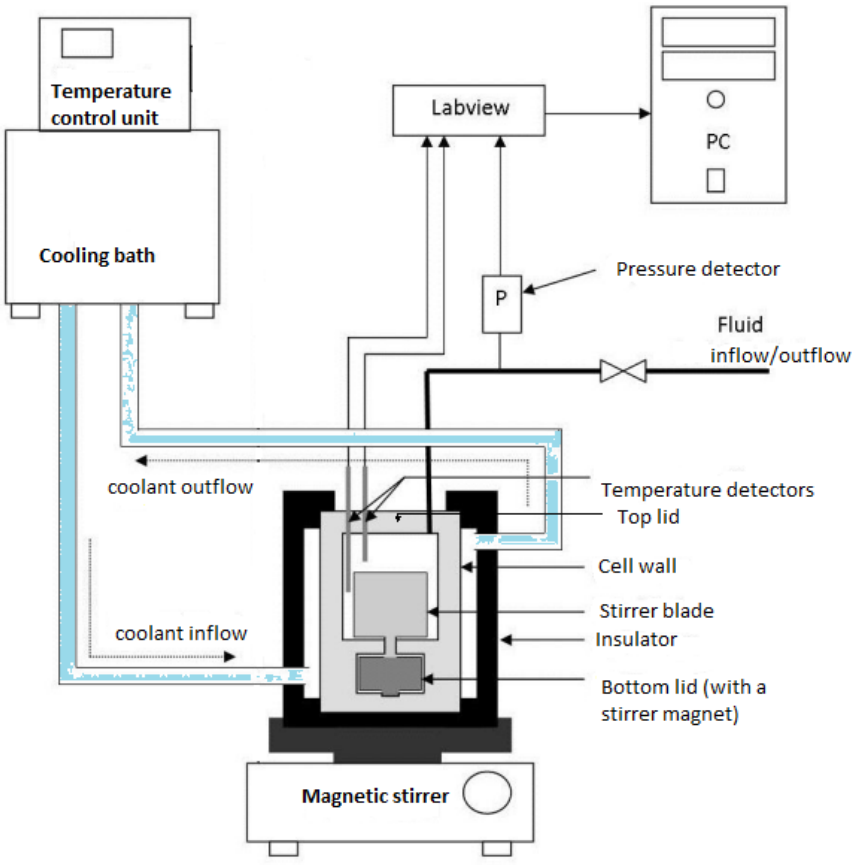

Figure 12: The experimental setup

The apparatus has these components:

- Cooling bath: Julabo 34 (±0.01 degrees)
- Temperature detectors: Pt-100, 1/10 DIN (± 0.03 degrees)
- Pressure detector: Rosemount (± 0.2 bars)
- Magnetic stirrer: IKA Reo basis C
- PC with additional software programs
- Titanium cell (volumes of 141 ml and 318 ml)/Sapphire cell (volume of 23 ml)

The geometry of the cell:

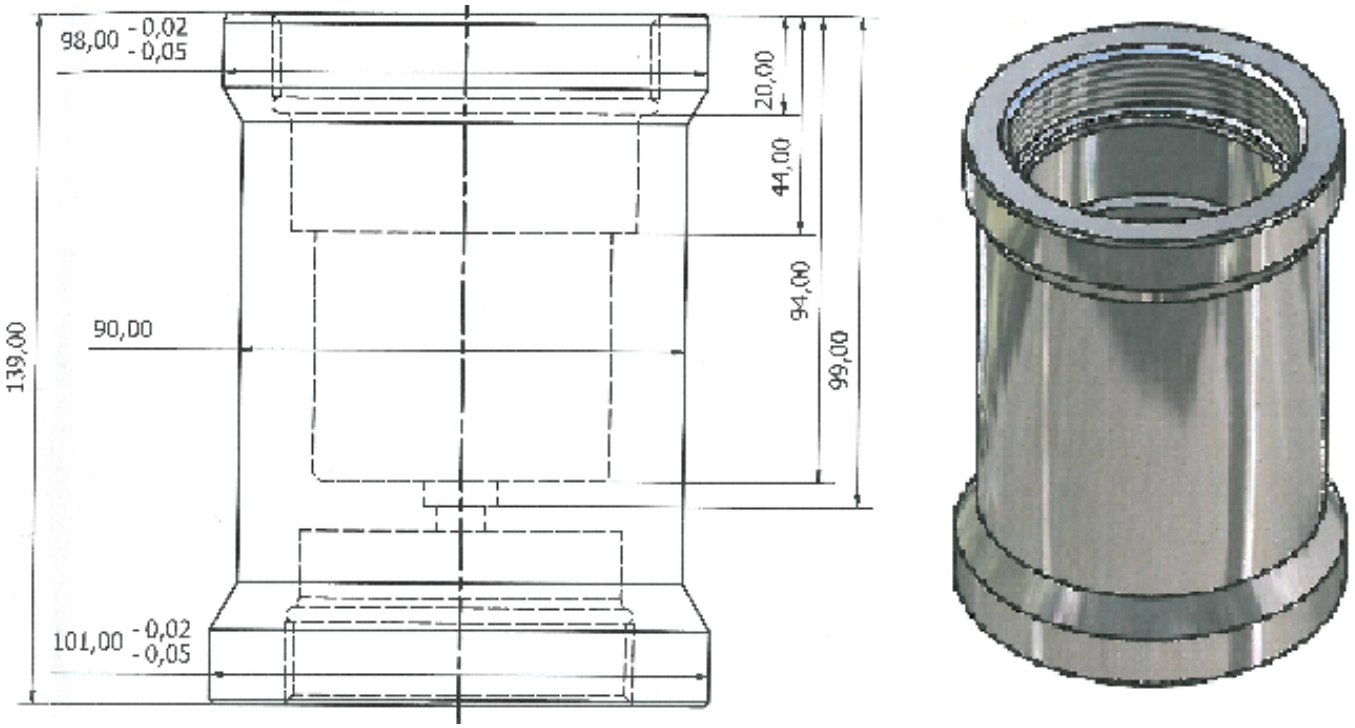

Figure 13: The geometry of the cell (titanium). The units are in cm.

The cell components:

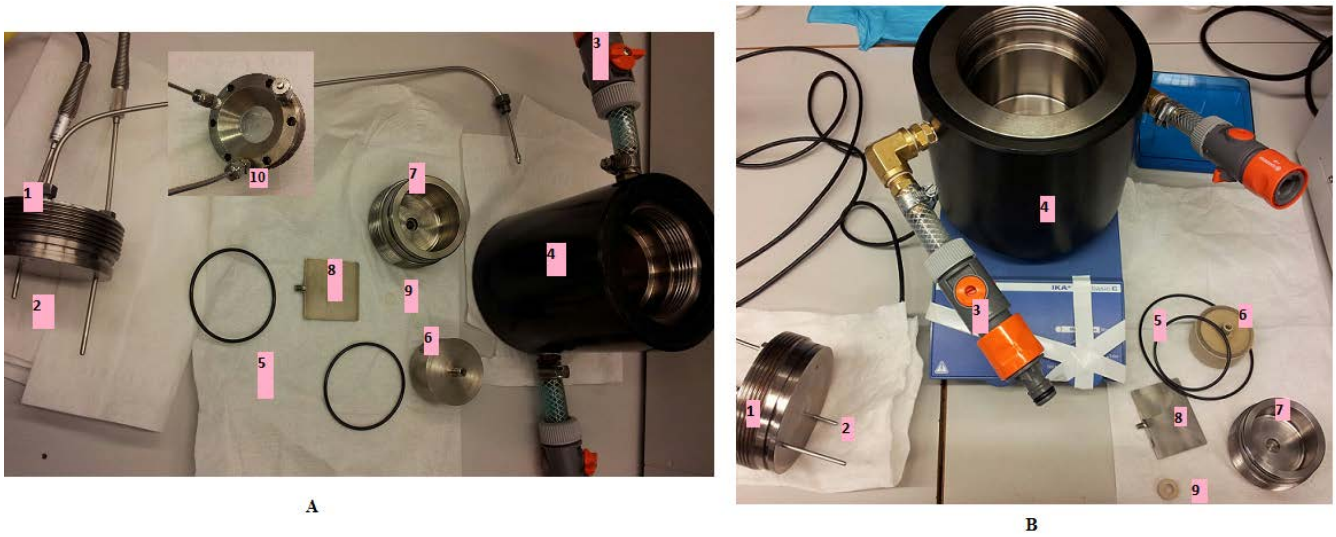

Figure 14: The components of the Titanium cells: (A) total volume of 141 ml, (B) total volume of 318 ml

The apparatus above has these components:

1. The top lid with a pressure detector
2. Temperature detectors
3. Inflow/outflow of the cooling bath
4. The cell with a protecting cap
5. O-rings
6. Magnet with ball bearings
7. The bottom lid
8. Stirring blade
9. A plastic ring (friction reducer)
10. Top lid with a Safire window (figure 13.A, only)

Figure 15: The components of the Safire cell

The apparatus above has these components:

1. Top lid with pressure and temperature detector
2. O-rings
3. Protecting cap
4. Connection between the bottom lid and the Safire cell
5. Bottom lid
6. Safire cell
7. Magnet with a ball bearing
8. The stirring blade

3.1.1 Software programs

Labview – measurements and data monitoring during run of experiments in real time.

Logitech webcam – pictures and video during run of experiments

Excel – view data detected, and transfer the data to a program for an analysis.

Kaleidagraph – save and compare data.

Matlab – Analyze and calculate the heat transfer coefficient.

3.1.2 Chemical solutions

In this thesis, the following have been used:
THF: (liquid), produced by VWR international AS 28.05.2010, EC-no: 2037288
EO: (gas), produced by Yara Praxiar, EC-no: 2008499
(Note: To be able to make a miscible solution of EO and water, EO needs to convert from gas to liquid phase, by cooling (see Figure 16.))

Both of these chemicals are highly dangerous for the environments and humans, as said in the SOP of both THF and EO. It is required to use gloves, protection glasses, laboratory coat, and gas mask.

In this case: there have been used 100-, 80-, 60-, 40-, 20 – and 0 % stoichiometric concentration (conc.) of both THF and EO in cell #5 and 80-, 40-, and 0 % stoichiometric conc. of both THF and EO in cell #5.

3.1.3 The experimental parameters

The accuracy of 1/10 DIN Pt-100 elements should be within ± 0.03 °C at 0 °C and ± 0.08 °C at 100 °C. Mounted in the system the temperatures were assumed measured within an accuracy of ± 0.1 °C. To verify the accuracy a calibration test were run in ice water at the end of the experimental program. The main reason for running the test was an observed discrepancy between the bath and the cell temperature during experiments. This discrepancy was assumed due to heat absorption through the top lid during the tests due to the large temperature difference between the cell (0 – 4 °C) and the surroundings (18 – 22 °C).

The calibration test in ice water (0°C) showed:
Cell #0, top lid with sapphire window:
$T_{g,\ cell\ \#0\text{-}1} = -0.05°C$

Cell #0, top lid with two temperature sensors:
$T_{g,\ cell\ \#0\text{-}2} = -0.02°C$
$T_{w,\ cell\ \#0\text{-}2} = 0.18°C$

Cell #5 showed temperatures:

T_g = 0.03°C
T_w = 0.17°C

All tests were conducted with temp sensors mounted in the top lid. Prior to the test the top lid with sensor was soaked in the ice water and cooled down to 0 °C to eliminate any leak of heat between the lid and the sensors. The discrepancy between the actual temperature and the measured temperatures were within the assumed accuracy for all sensors in the gas phase, but the water temperature sensors showed both deviations greater than the assumed accuracy. This could be due to some imperfect connection in the line between the signal cables and the temperature transmitters.

3.2 Experimental procedure

3.2.1 Washing procedure

Before each experiment (i.e. form hydrate at a different conc.) the cell needs to be reassembled and washed twice with soap and distillated water and then dried with air. When changing the conc. of the additive (THF or EO) there is a possibility to get impurities which is the reason for using soap. The memory effect on water due to melted hydrates are taking care of, thereby washing procedure.

3.2.2 Start-up procedure

High vacuum silicone grease and copper grease were used on the O-rings and threads, respectively when assembling the cell.

The amount of water and chemical is dependent on the different sizes/volumes of the cells. In every case the cell is filled with a 66 percent of air, and the rest is a miscible water-THF/EO solution, or water. (Further information found in the appendix.)

Example: (141 ml)
The bottom lid is filled with 7.5 ml of water
The cell is filled with 50 ml of water (approximately 51.40 ml of miscible solution)

Example: (318ml)
The bottom lid is filled with 7.5 ml of water
The cell is filled with 112 ml of water (approximately 113.40 ml of miscible solution)

The stirring starts when the cell is connected to the cooling bath and the pressure/temperature detector(s). Before running the experiments the temperature in the cell needs to match the temperature of the coolant. In the end, a chosen program (on the cooling bath) is used so that hydrates are able to form. Now, run the program (e.g. cooling bath) and Labview at the same time.

The procedure where EO is changing from gaseous phase to liquid phase is by cooling (from the tubing connected to the bottle), like this:

Figure 16: The cooling system of EO (gas to liquid)

Note: EO has melting equilibrium point at 11°C (see section 3.2.5), which means that the entire system (including the cell) needs to be below 10°C.

3.2.3 Programming the cooling bath

The programming procedure is as follows:
Click “menu” → “Int.programs” → “edit” → step 0 → step 1 → step 2

Example:

Step	0	Step	1	Step	2
Temp.	6.00 C	Temp.	1.00 C	Temp.	1.00 C
Time	00:10	Time	01:00	Time	99:00

The start-up procedure is as follows:
Click “menu” → “profile start” → “yes”

3.2.4 Heat transfer procedure

This procedure has been done in both of the titanium cells (cell #0, and cell #5).

After the hydrates are formed and hydrate growth reaches 100 percent, the heating and cooling sequences (HCS) have been performed. Since THF has an equilibrium melting point at 4.98°C (see section 3.2.5), this work is performed between 1- 4°C on both THF and EO to get more accurate data.

The HCS has been done at once, so the consistency is important. Therefore when the heating sequence is done and the temperature in the cell is leveled out (approximately 5 -10 minutes) the cooling sequence starts. The run is finished when the temperature has reached the same temperature as the starting point (see Figure 17).

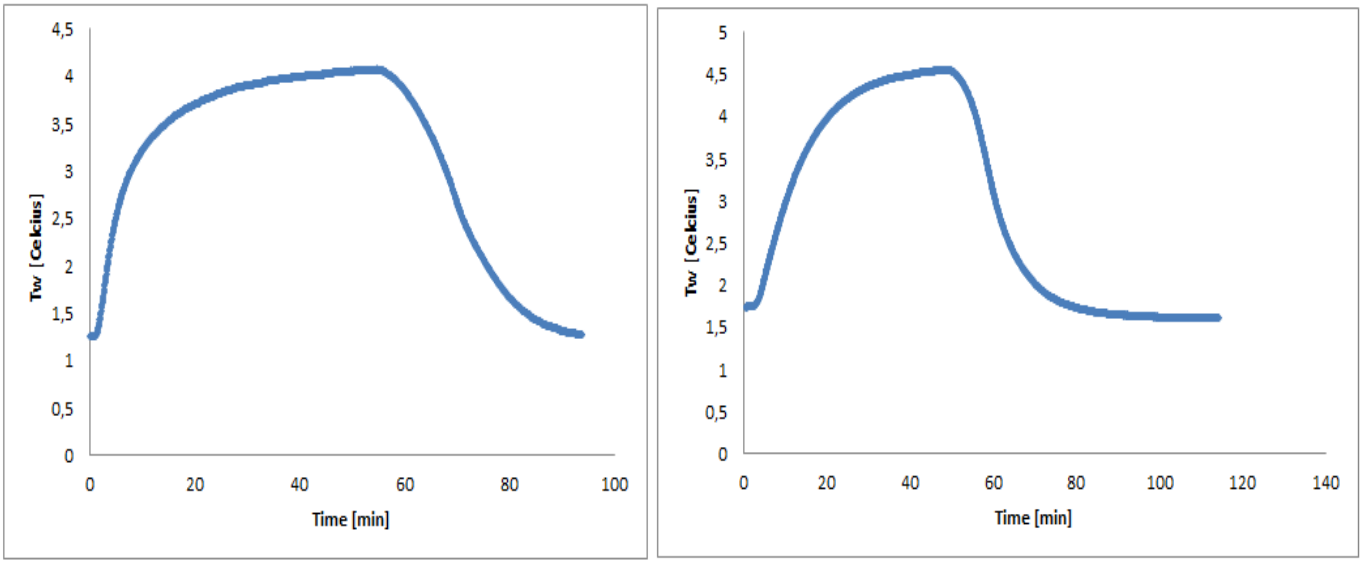

A B

Figure 17: An example on a HCS. (A) The heating sequence is leveled out (longer time used) than (B) where the leveled heating sequence is too short.

The HCSs have been performed on different rotational speeds 0, 500 and 1000 RPM, respectively. It is also been performed HCSs on different stoichiometric conc. of THF/EO, and in two different conducted cells volumes.

3.2.5 Observation procedure

This procedure has been done in both titanium cell (cell #0 with a sapphire window at the top lid) and in two Sapphire cells (cell #1 and cell #2).

The main purpose of this procedure is to predict how the hydrate is like (a hydrate film, plug or slurry) at the different stoichiometric conc. of THF/EO, and to see if the hydrate is stable throughout the HCS (i.e. stable hydrate structure (SHS)). (This procedure is been done the same way as the other experiments, with an additional camera.)

When run the heating sequence, the rate of heating or cooling is very rapid (approximately 8-9 °C/h), therefore, the dissociation of the hydrates is slower due to faster heating rate.

The stability of the hydrate is also observed by looking at the changing in the equilibrium melting temperature (T_{eq}) at each stoichiometric conc. of both THF and EO (look at Table 11).

Literature on hydrate equilibrium properties of EO and THF as function of concentration are scarce. Using stoichiometric conc. of THF in water and hydrogen as inert atmosphere the hydrate dissociation temperature (i.e. T_{eq}) has been determined to 4.4 °C (E. Dendy Sloan & Koh, 2008). According to data in Table 6 the contribution of hydrogen to the hydrate stability should be negligible. The conducted experiments, in this present work, have been done in presence of air, and according to the same Table (6), air being composed of oxygen and nitrogen as main components could affect the stability of both sI and sII hydrate.

In the laboratory, Svartaas has measured the T_{eq} of stoichiometric conc. of THF in water in presence of a pure nitrogen atmosphere and found that the hydrate dissociated at 4.98 °C (Svartaas, 2014).This shows that the nitrogen atmosphere result in a hydrate with increased stability and increased melting temperature.

Figure 19 shows literature data on hydrate T_{eq} for EO hydrate as function of the concentration in water (Dever et al., 1994; Siegfried & Dieter, 1987) The maximum T_{eq} was found at a mole fraction of 0.1491 which corresponds to 114.1 % of the stoichiometric conc. and the T_{eq} decreased at increasing or decreasing mole fractions above / below 0.1491. In figure 19 only the mole fractions below the maximum is included, and the figure shows that the stability of EO hydrate is function of concentration in water phase.

Table 6: Ratio of molecular diameter to cavity diameter for gas hydrates (E. Dendy Sloan & Koh, 2008).

Guest hydrate former		Molecular diameter/cavity diameter for cavity type			
		Structure I		Structure II	
Molecule	Diameter[b] (Å)	5^{12}	$5^{12}6^2$	5^{12}	$5^{12}6^4$
H_2	2.72	0.533	0.464	$0.542^{\zeta\phi}$	$0.408^{\zeta\phi}$
N_2	4.1	0.804	0.700	0.817^{ζ}	0.616^{ζ}
O_2	4.2	0.824	0.717	0.837^{ζ}	0.631^{ζ}

$^{\zeta}$ Indicates the cavity occupied by the simple hydrate former.
$^{\phi}$ Indicates that the simple hydrate is only formed at very high pressure.

Table 6: Indicates that the smaller molecules as nitrogen compared due to Hydrogen occupies more of the smaller cavities in sII. This means that the hydrate formers, THF in particularly (see table 2),in all probability, will have a higher melting equilibrium temperature when using nitrogen, oxygen, or air rather than hydrogen during cell experiments. The presence of air could also have some effects on the stability and melting point of EO hydrate.

Figure 18 shows the concentration of methane in the aqueous phase as function of temperature at a given pressure for system with and without hydrates present in the solution. In this figure, the reduced methane concentration as function of decreasing temperature for system with hydrate present, corresponds to an equilibrium condition of system at reduced pressure.

Figures 18 and 19, both demonstrate the relation between the concentration of a hydrate former in the aqueous phase and the equilibrium dissociation properties of the system. As demonstrated by these two figures, there is expected that the T_{eq} of the THF and EO solutions, used in this present work, will change as function of stoichiometric conc. At low stoichiometric conc. of both EO and THF, there have been seen some conflicts with the hydrate stability during some conducted experiments.

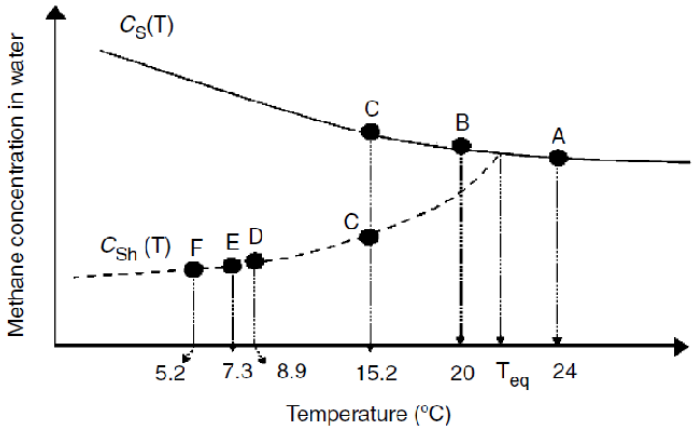

Figure 18: The equilibrium temperature (Teq) vs. concentration of methane –water solution (Subramanian, 2000).

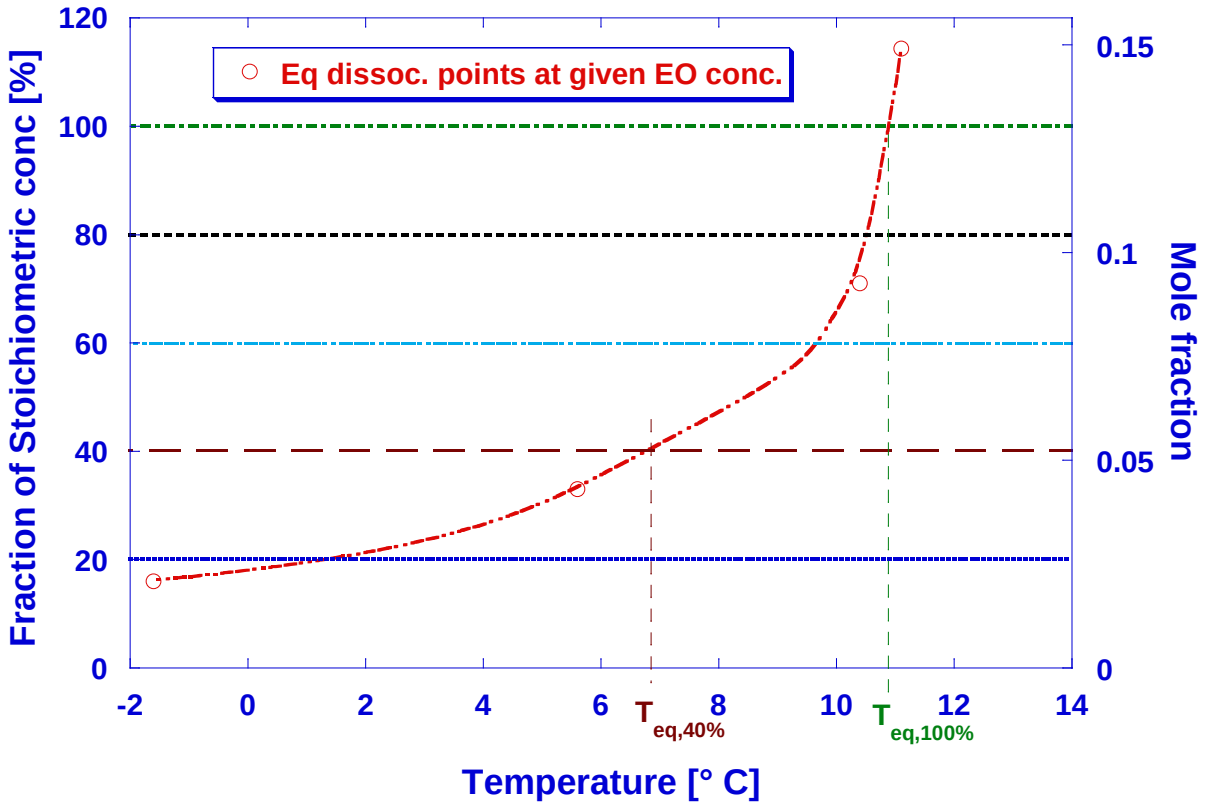

Figure 19: Equilibrium EO hydrates dissociation temperatures (red dots,) versus mole fraction of EO in the water solution (right y-axes)(Dever et al., 1994; Siegfried & Dieter, 1987). Stoichiometric EO – water solution is denoted 100 % (left y-axes). The indicated EO equilibrium curve (red) is only illustrative.

To evaluate the stability of the EO and THF hydrates at reduced stoichiometric conc. in water, some tests were run in the sapphire cells and a titanium cell with a connected sapphire window, to observe whether the hydrates remained stable or not. (See section 4.3.3.)

3.3 Experimental analysis

Matlab is used to estimate the HTC of the inner boundary, by use of a simulation model made by Prof. Runar Bøe (see appendix).

The heat transfer model is based on some major assumptions;

- The temperature in the reaction chamber is homogenous
- The flow of heat is radial
- A transient temperature profile
- Hydrate generation is zero
- An implicit discretization, which allows the time increment to be chosen to correspond with the logging rate of the temperature measurements.
- The structure of hydrates doesn`t matter
- The heat transfer coefficient takes care of both convection and conduction, but cannot distinguish between them, or which is dominant. (The border condition is the convective heat transfer.)
- The outer "infinite" temperature is set equal to the heating/cooling bath temperature, $T_O = T_B$. The measured values from a given run are imposed as time-varying border temperature for the corresponding simulation.
- The inner "infinite" temperature, $T_I = Tw$ is set equal to the fluid temperature in the cell. A time series of this temperature will be the result from a simulation, and may be compared due to the measured values from the given run.
- The outer heat transfer coefficient (h_O) is set to 1000 W/m^2K (see appendix), and treated as a constant.
- The simulated heat transfer coefficient (h_I = HTC) is treated as a constant value.
- The HTCs (h_I and h_O) are constant over the time period of interest.
- The heat capacity data required is stated in table 2, and $c_{p,air}$ = 1004 J/kg (Urieli)

The simulation model is based upon three curves; the inner temperature (green), the outer temperature (red) and the simulated temperature (blue), where the point is getting the best fit (i.e. the minimum variance between the outer and inner temperature) of the simulated curve (see Figure 20A).

Two methods of the simulation model exist:

- **Golden Search:** the minimum variance of the simulated temperature between the outer and inner temperature.
- **Try and Fail:** Changing the value of h_I until you get the best fit

(More details can be found in the appendix.)

The Golden Search method gives the best fit, normally. In some cases the Golden Search method fails (see Figure 20 and appendix):

- Fluctuaction of the HCS
- "Weird phenomenas"(reminds of melting/formation sequence) in the HCS
- Unknown reason

The "Golden Search" simulation has similar trend when changing h_I value of ±10 [W/m^2 K], in general.

When the Golden Search method doesn`t work, there is a need of using Try and Fail method. When having these "weird phenomena" the Try and Fail method doesn`t work either. Therefore, some comparisons have been done of the hydrates vs. the solution of THF. This is shown in section 4 (see Figure 21 and 22).

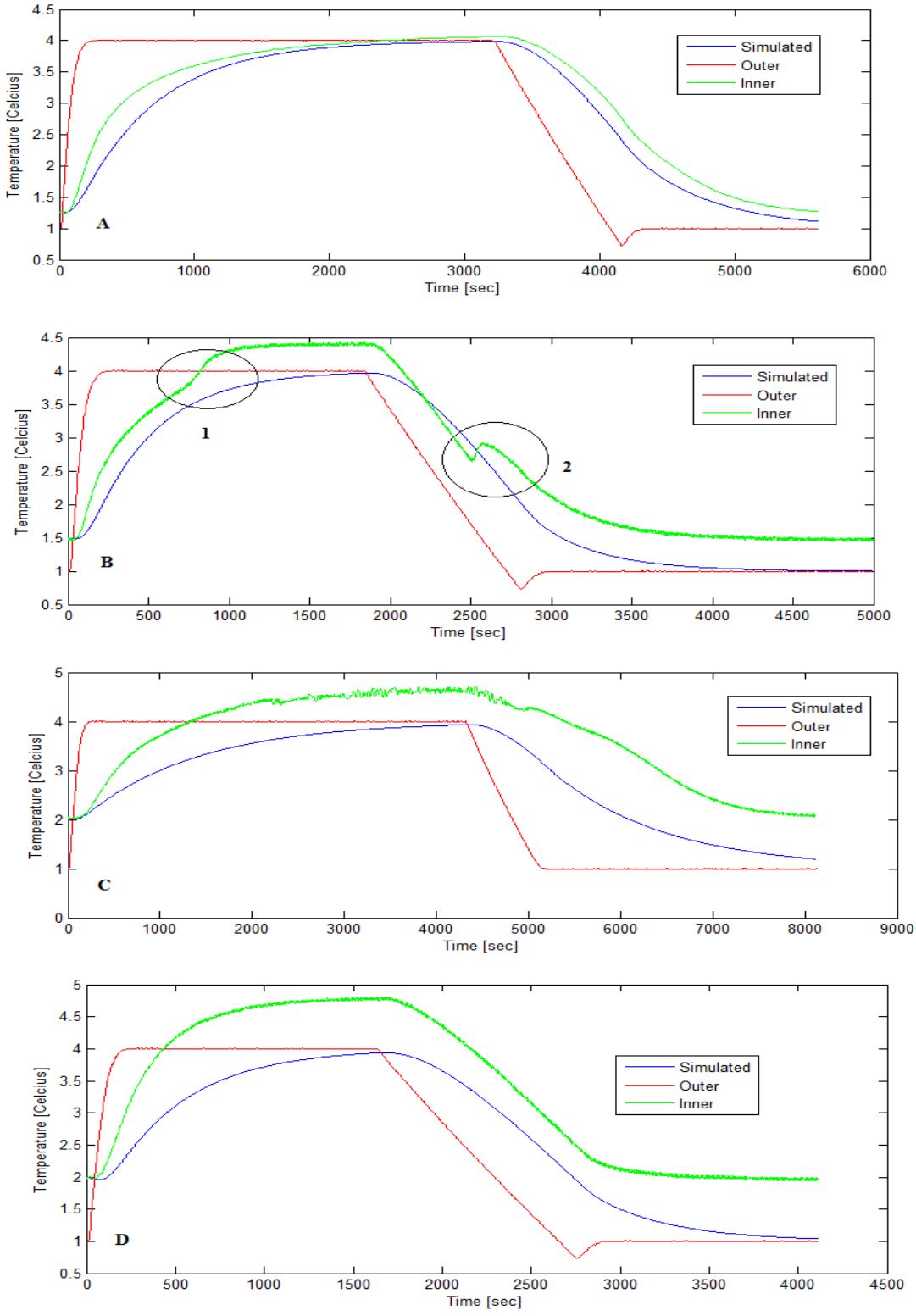

Figure 20: The simulated HTC by use of the Golden Search method; (A) Perfect match, (B) "weird phenomena" of inner temperature. (1) is melting sequence and (2) is formation sequence, most likely, and (C) Fluctuaction in inner temperature and (D) unknown reason for mismatch.

4 RESULT/DISCUSSION

4.1 Refused experiments

Some of the performed experiments, in the laboratory, were rejected due to equipment failure. For some concentrations of EO and THF in the region of 20-40 % stoichiometric or lower, hydrate formation didn`t occur or hydrates were unstable during heating-cooling test (partially dissociation during heating and re-formation during cooling). Formation of hydrates at stoichiometric conc. of 20 % or lower was almost impossible at experimental temperatures above 0°C.

4.2 Stability of THF hydrates during heating-cooling sequences

At 20 % stoichiometric conc. hydrate formation was not observed to occur at the "normal" formation temperature of 1 °C. The bath temperature was reduced to -0.5 °C in attempt to provoke hydrate formation, and it did. A heating-cooling test were made, and showed that THF hydrate with 20 % stoichiometric conc. melted before reaching 1°C. It was concluded that a concentration of 20 % stoichiometric THF solution is not suitable for the desired measurements.

Some peculiar responses were observed during HCSs on 40 % stoichiometric THF solutions. During the cooling sequence sudden heat release was observed indicating hydrate nucleation and growth in fluid not containing hydrates. This could occur if hydrates were completely dissociated during the previous heating sequence. To investigate this phenomenon, it was decided to compare the responses during heating-cooling sequences for system with fresh THF solution not previously exposed to hydrate formation. In addition, fresh THF solution was added to the cell, cooled down without stirring to avoid hydrate formation and then run a heating sequence to observe the response of THF solution without hydrates present during heating. The result of these tests is shown in Figures 21 and 22.

Figure 21A shows the experimental runs (denoted #1 #2 and #3 in the figure), cooling sequences, previously being exposed to hydrate formation; all show initial responses comparable with the fresh 40 % stoichiometric THF solution without hydrates. In addition all

3 runs show heat release during cooling indicating nucleation and growth from “hydrate free” system.

Figure 21B shows that the fresh THF solution without hydrates reaches the upper ramp temperature much faster than the systems with hydrates present. For the latter systems it is observed that the temperature gradient shows a sudden increase at the temperature region between 3.5 and 4 °C and the gradient approach a slope comparable with the fresh THF solution. This indicated that the hydrates were completely dissociated at this temperature and that the continuing heating response was comparable with hydrate free system. Similar problems were observed repeating the tests in the larger cell (cell#5).

Figures 22A and B shows situation where the fresh THF solution formed hydrate during the initial cooling cycle (cf. Figure 22B). During heating cycle (cf. Figure 22A) all solutions showed similar temperature responses and responses similar with the hydrate containing systems in Figure 21A. This test confirmed the instability problem during HSC runs on 40 % stoichiometric THF solution.

These tests show that at 40 % stoichiometric solution, the THF hydrates were not sufficiently stable within the temperature region of the HCS to run reliable HTC measurements.

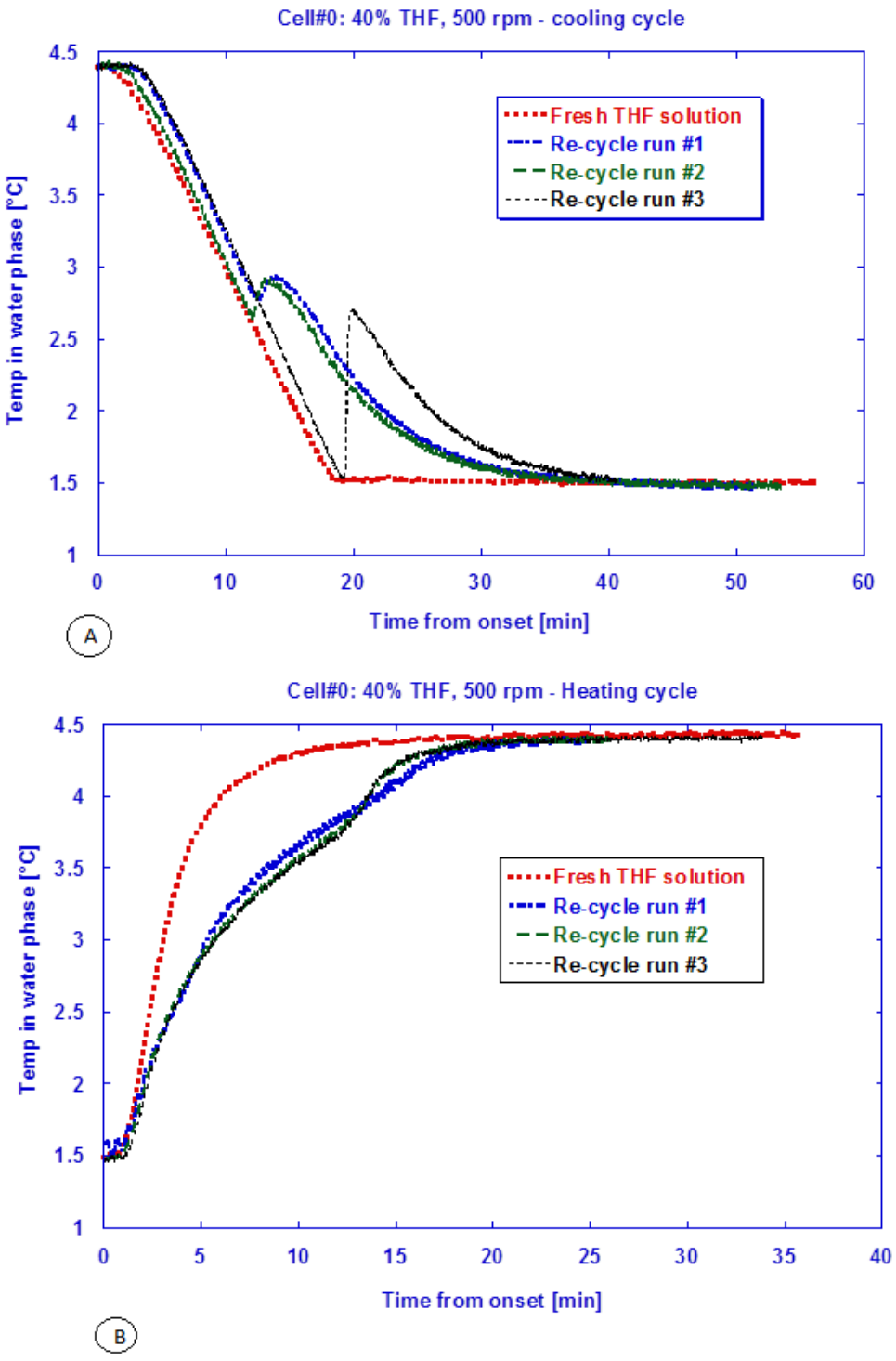

Figure 21: An example of a comparison of HCS between a fresh THF solution (40 % stoichiometric conc.) and the experimental runs (#1-3): (A) heating sequence (having phenomena (1)), and (B) a cooling sequence (having phenomena (2)) (see figure 20).

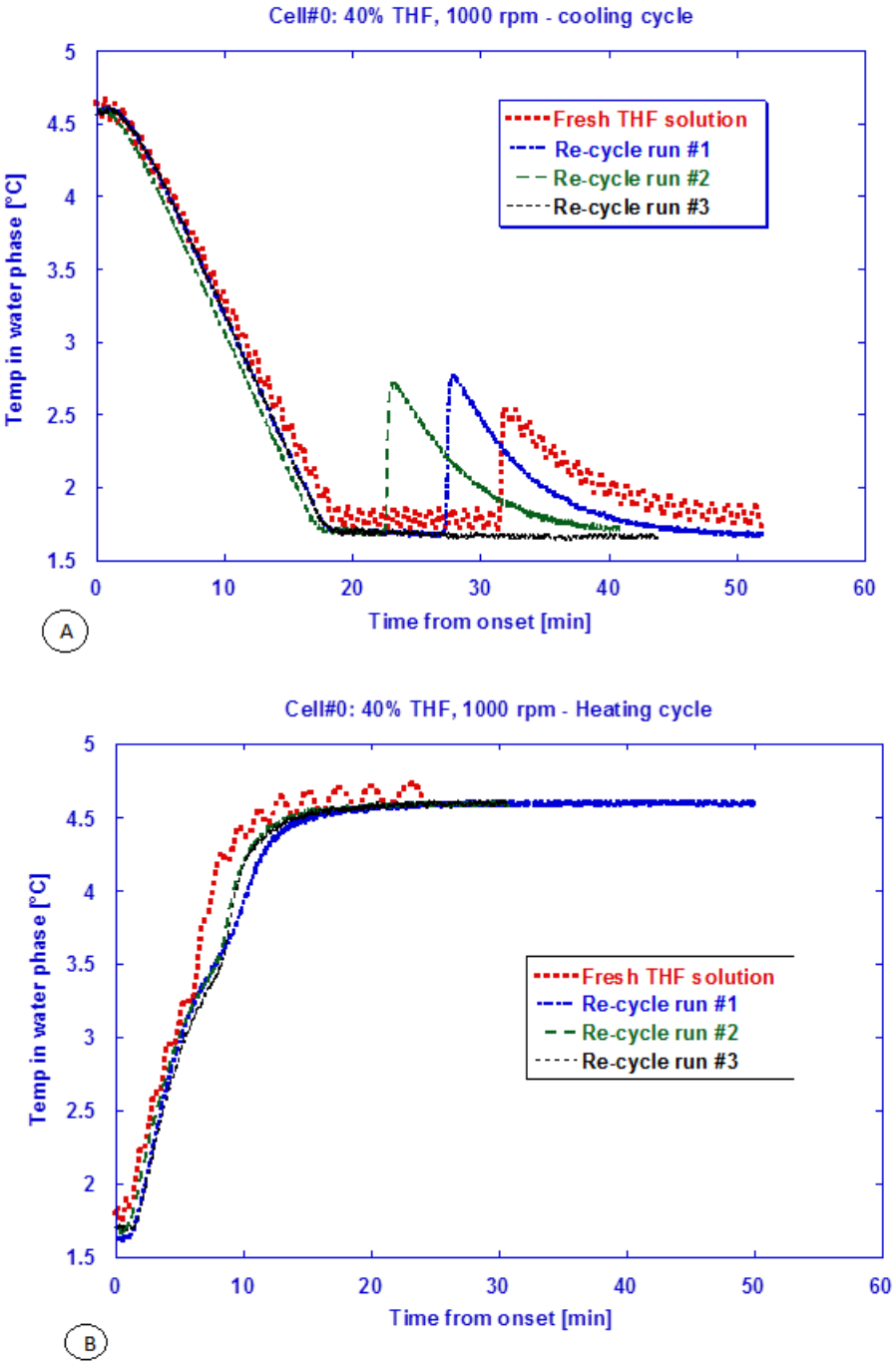

Figure 22: An example of a comparison done with experimental runs and the fresh solution of 40 % stoichiometric conc. of THF, when the solution has: (A) formed hydrates and (B) melted hydrates. (Here: cell #0 at 1000 RPM.)

4.3 The geometry/structure of the hydrates

The sapphire window top lid version of the cell was used to observe the quality of the hydrates during a test. In addition sapphire cell experiments were run for the same purpose. In the titanium cell initial experiments were done on 100 % stoichiometric THF (or EO) concentration, reducing the concentration at steps of 20 % down to 80%, 60 %, 40 % and 20 %. Having converted the optimal amount of water into hydrates, the cell was maintained at low temperature while the top lid was dismounted to obtain a better observation of the hydrates formed. Dependent on the concentration of THF, the hydrate consistencies could vary between dry hydrates pasted on the wall to wet hydrate slush / slurry.

Figure 23 illustrates the difference between a hydrate film and slurry, observed.

Figure 23: Illustrates the hydrate structure; (A) hydrate film and (B) hydrate slurry, observed in cell #0 with a sapphire window.

In the sections below, the observations on THF and EO hydrate are summarized in Tables 7 - 10.

4.3.1 THF

Table 7: An overview of THF hydrate in a Titanium cell

141.4 ml Titanium cell						
THF content	100	80	60	40	20	10
Visible?	Yes	Yes	Yes	Yes	No	-
At 1C	Dry hydrate layer	Dry hydrate layer	Wet hydrate layer	Slushy hydrate plug and a thin wet hydrate	Water - like plug(Foam)	-

			(sticky)	layer (sticky)		
At 4C	Same (stable)	Same (stable)	Slush (not stable)	Slushy hydrate plug (stable)	Water – like No hydrates	-
Thickness (cm):	1.0	1.2	1.5 - 1.7	T: 0.2 B: plug (the entire cross-sectional area)	Plug (the entire cross-sectional area)	-

(Note: the hydrate film was the same size along the entire wall. The measurements done have an uncertainty of ±0.1cm, and T=Top, B=Bottom)

Table 8: An overview of THF hydrates in a Sapphire cell

23 ml Sapphire cell						
THF content	100	80	60	40	20	10
Visible?	yes	yes	yes	yes	Yes (below 1°C)	No
At 1C	Dry hydrate plug	Wet hydrate plug	Wet hydrate layer at the wall	Slushy hydrates	Water-like No hydrates	No hydrates (water-like)
At 4C	Same (stable)	Same (stable)	Slushy (Not stable)	Slushy (Not stable)	Water-like no hydrates	No hydrates

Increase in stoichiometric conc. of THF gives an increase in stability when performing a HCS. For the stoichiometric conc. ≥ 60% there is stable hydrate structure (SHS) in the system. When the stoichiometric conc. is ≥ 60% the THF hydrate form layer around the wall. Conc. of THF <40% stoichiometric gives a slurry –like hydrate structure (hydrate particles suspended the water phase) Conc. of THF at 40% of stoichiometric resulted in some consistency in between a hydrate layer and slurry. When the stoichiometric conc. is ≤ 20% the hydrate formation is hard to accomplish. The HCS is probably performed without any hydrate present.

The problem here is to know if the hydrate does melt or not. If it does not melt, it has been a mechanical damage, so that the hydrate structure will convert from being a thin hydrate layer to just being slurry.

4.3.2 EO

Table 9 An overview of EO hydrates in a Titanium cell

141.4 ml Titanium cell						
EO content	100	80	60	40	20	10
Visible?	Yes	Yes	Yes	yes	yes	-
At 1C	Dry hydrate layer	Dry hydrate layer	Wet hydrate layer	Wet hydrate layer	Slushy hydrate plug and a thin wet hydrate layer	-
At 4C	Same (Stable)	Same (Stable)	Same (Stable)	Same (Stable)	Slushy hydrate plug (not stable)	-
Thickness (cm)	T: 1.0 M: 0.8	T: 1.0 M: 0.6	T: 0.5 M: 0.3 – 0.2	T: 2.5 M: 1.5	Plug (the entire cross-sectional area)	-

(Note: T = top, M = middle. The measurements done have an uncertainty of ±0.1cm)

Table 10 An overview of EO hydrates in a Sapphire cell

23 ml Sapphire cell						
EO content	100	80	60	40	20	10
Visible?	Yes	Yes	Yes	Yes	yes	No
At 1C	Dry hydrate plug	Dry hydrate plug	Wet hydrate plug	Wet hydrate plug	A hydrate layer	no hydrates (water-like)
At 4C	Same (Stable)	Same (Stable)	Same (Stable)	Same (Stable)	Water – like (not	No hydrates

					stable)	

Note: when using the term stable it means stable hydrate structure (SHS) which is when the hydrate has the same structure through the whole HCS.

Increase in stoichiometric conc. of EO gives an increase in stability when performing a HCS. For the concentrations ≥ 40% there is SHS. Stoichiometric conc. ≥ 40% have a hydrate structure as a film along the wall. Stoichiometric conc. ≤ 20% have a hydrate structure as slurry. When the stoichiometric conc. is < 20% the hydrate formation is hard to accomplish. The HCS is probably performed without any hydrate present.

4.3.3 Hydrate dissociation during heating sequences

For methane hydrate – water mixtures it is a relation between the temperature and the concentration of methane in the water phase. This concentration is lower than the concentration of methane in hydrate free water solution at the same pressure and temperature condition (illustrated in Figure 18). Similar relations exist for both THF and EO hydrate-water solution. Table 11 give observed T_{eq} during THF and EO experiments conducted in the present work. These T_{eq} do not represent equilibrium condition and could be from some tents to a degree above equilibrium due to the high heating gradient during experiments. For the 100 % stoichiometric solution, an T_{eq} of 4. 98°C for THF was measured by Svartaas (mentioned in section 3.2.5).

Table 11: the relation between the stoichiometric conc. [%] and Teq [°C] observed, experimentally.

	THF	EO
Stoichiometric conc. [%]	Observed Teq [°C]	Observed Teq [°C]
100	4.98 – 5.10	11.1
80	4.90	10.50
60	4.60	10.0
40	3.75	9.0
20	0.5	2.0

The observed T_{eq} appear to be fair correspondence with equilibrium data from literature (mentioned in section 2.3.5). Figure 19, gives an illustration of the relationship between the concentration and T_{eq}, for EO-water solution.

As seen in Figure 19, the estimated equilibrium curve indicates that T_{eq} lies between 8-11°C of 40 – 100 % stoichiometric conc. of EO – water solution. The observations done, in the present work, with air (nitrogen and oxygen) present in the system, could thus be reasonable taking the high cooling rate into account.

4.3.4 THF vs EO

THF is less stable throughout the HCS than EO, since the observed T_{eq} for the EO system at stoichiometric conc. above 40 % is higher than the corresponded THF system. In addition, THF produced a much thinner hydrate layer compared to EO, at similar concentrations.

EO is stable at all concentrations except from 20 % stoichiometric conc., but THF is only stable between 100 – 60 % stoichiometric conc. Both EO and THF represent hydrate which has issues making hydrates ≤ 20 % stoichiometric conc., as observed, the T_{eq} is very low.

The dissociation temperatures for THF were observed to decrease more rapidly as function of decreasing concentration thus producing a steep dissociation curve over the whole concentration region compared to EO. Both solutes, THF and EO, the dissociation temperatures were observed to decrease as function of decrease concentration more rapidly than the trend in figure 18 and 19 shows. This means that THF has a lower equilibrium temperature than EO at same amounts of hydrate present. Therefore, EO represents a more SHS compared to THF, and would be more suitable for the type of study conducted in the present work.

4.4 Concentration effects

4.4.1 THF

Figure 24 shows the relation between the estimated HTC as function of stoichiometric THF concentration during experiments at stirring rates of 0 RPM, 500 RPM and 1000 RPM, in cell #0.

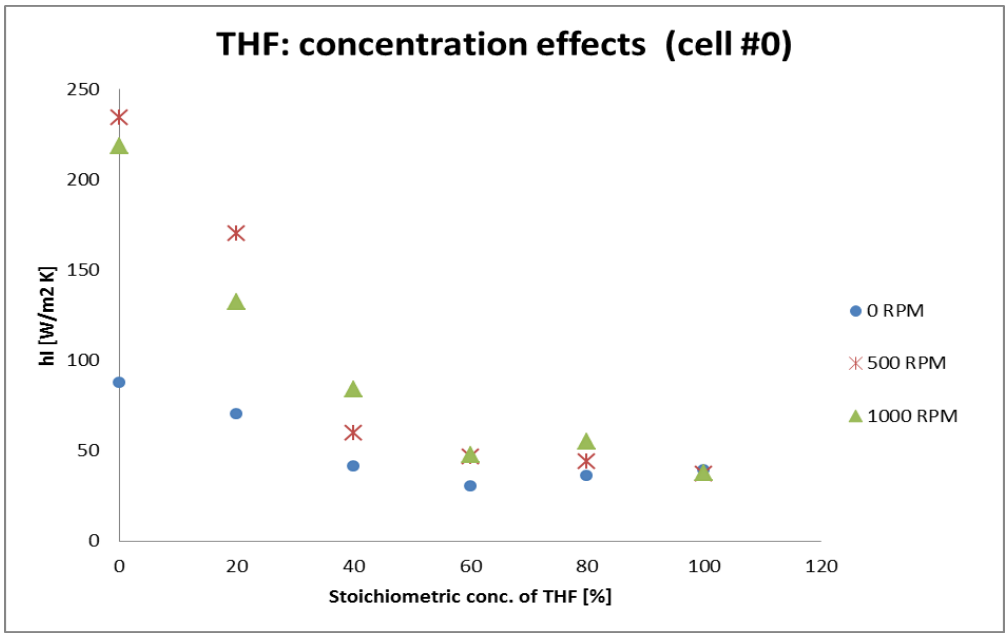

Figure 24: Effect of the concentration on simulated HTC in THF hydrates (cell #0).

Figure 24 shows that estimated HTC decrease with increasing stoichiometric conc. of THF, both with and without stirring. Without stirring the values of estimated HTC are lower compared to the situations with stirring. Increased stirring rate is assumed to result in increased estimated HTC, but between 500 and 1000 rpm, the difference between these two stirring rates was marginal. At concentrations of THF above 60 % of stoichiometric estimated HTC approach fairly constant level similar for all stirring rates.

The lowest estimated HTC values are shown at 0 RPM, at all stoichiometric conc. of THF. The case of 0 RPM has a higher conductional heat transfer, therefore, the experiments without stirring with THF hydrate present, supports the theory (see section 2.4.4).

In all of the cases (at all stirring rates) in Figure 24 the estimated HTC decrease with increase in stoichiometric conc. of THF, which is similar the methane hydrate system described in section 2.4.2. It is suggested that the hydrates above 60 % stoichiometric conc. had produced immobile hydrate layers on wall and thus stirring will no longer affect heat transfer by conduction in any of the systems. (Mentioned in section 2.4.4).

4.4.2 EO

Figure 25 shows the relation between the estimated HTC as function of stoichiometric EO concentration during experiments at stirring rates of 0 RPM, 500 RPM and 1000 RPM, in cell #0.

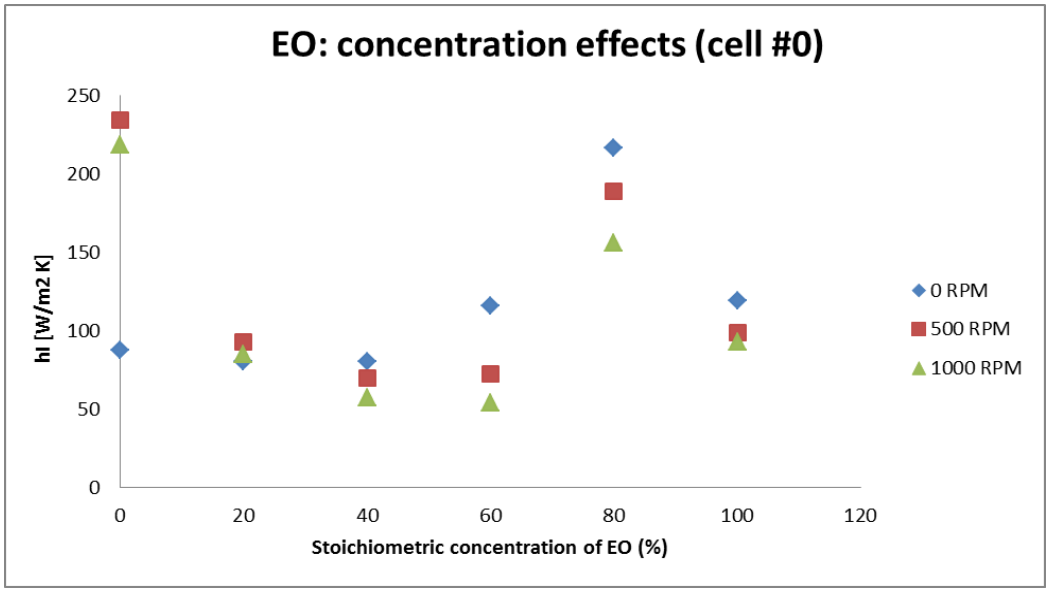

Figure 25: Effect of the concentration on simulated HTC in EO hydrates (cell #0).

Without stirring, the stoichiometric conc. of EO in region between 0 – 40 %, the estimated HTC remains approximately constant except from 80 % stoichiometric conc. With stirring, the estimated HTC is decreasing with increasing stoichiometric conc., for all stoichiometric concentrations below 60%. Between 60 - 80 % stoichiometric conc., the estimated HTC increase with increasing stoichiometric conc., and between 80 - 100 % stoichiometric conc. of EO, the estimated HTC decreases with increasing stoichiometric conc. The effect of stirring rate was marginal.

The lowest estimated HTC values are shown at 0 RPM, at 0% stoichiometric conc. of THF. When higher % stoichiometric conc. is present in the system, 1000 RPM represent the lowest estimated HTC values. The case of 1000 RPM has a higher conductional heat transfer, therefore, the experiments with EO hydrate present, do not support the theory (see section 2.4.4).

In Figure 25, the systems with 500 and 1000 RPM and at stoichiometric concentrations between 0 and 60 % show similar pattern in estimated HTC with a decrease as function of increasing concentration. This response is comparable with the methane hydrate system discussed in section 2.4.2. With 80 % stoichiometric conc. of EO, the estimated HTC is above the values measured at 60 and 100 % stoichiometric concentration. This induced estimated HTC can be affected by increase in convectional heat transfer caused by increase in the thickness of the hydrate layer (see section 2.4.4). Or an increase in Reynolds number (Re) caused by an increase in the viscosity can be the reason for the increase in the estimated HTC at 80 % stoichiometric conc. of EO. Note that similar effects have been shown for a system without stirring as well. Therefore, the effects shown for 80 % stoichiometric conc. of EO, appears independent of stirring and Re.

4.4.3 THF vs. EO

Figure 26 shows the relation between the stoichiometric conc. of the solute as function of the estimated HTC at stirring rates of 0 RPM, 500 RPM and 1000 RPM, for both the THF and the EO systems in cell #0.

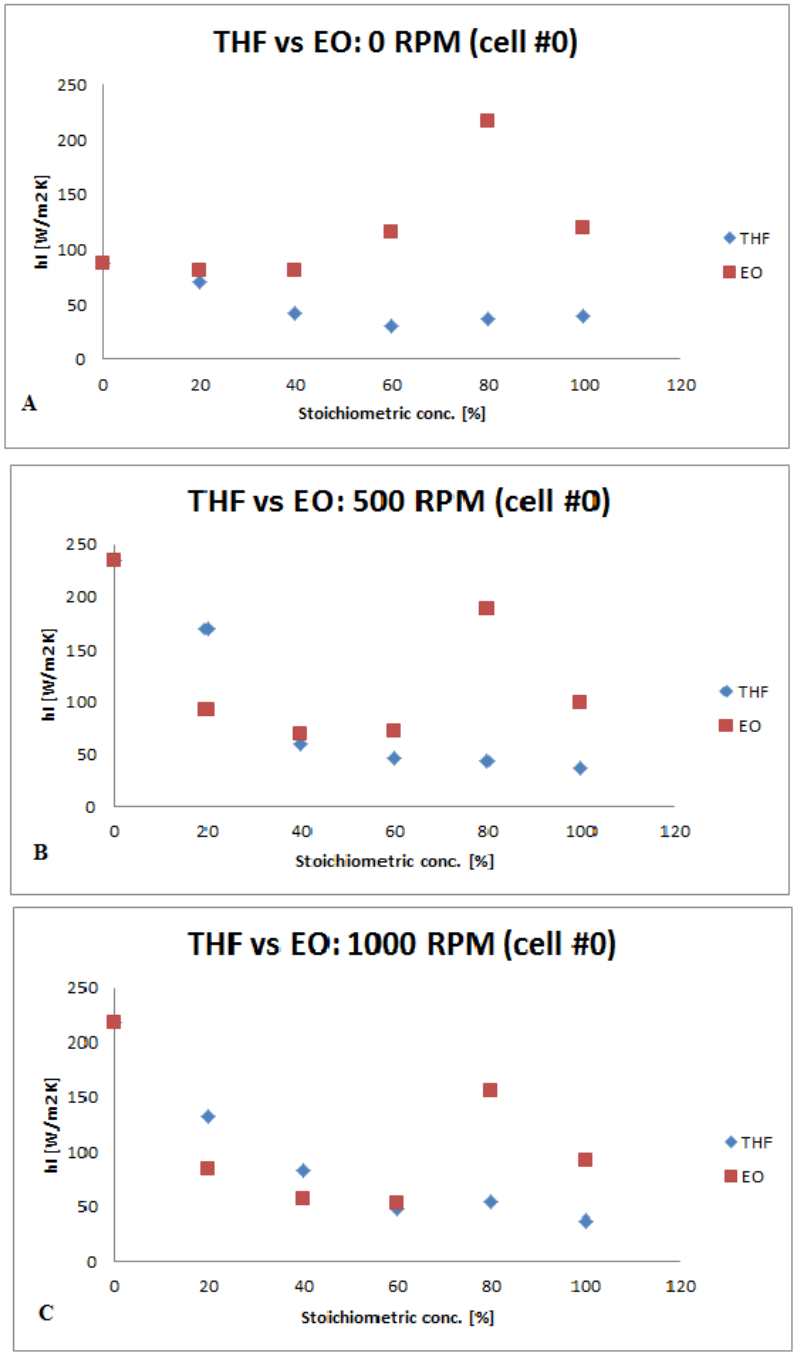

Figure 26: Concentration effects on simulated HTC of both THF and EO at: (A) 0 RPM, (B) 500 RPM and (C) 1000 RPM (cell #0).

For both 500 RPM and 1000 RPM, the estimated HTC decrease with increasing stoichiometric conc. up to 60 %, for both THF and EO systems. Without stirring, in the region between 0 % and 20 % stoichiometric conc. of both THF and EO hydrate have comparable and almost identical estimated HTC values. The estimated HTCs of EO system is approximately constant in the region between 0 and 40 % stoichiometric conc., and then

increase towards a maximum at 80 % before it drops towards 100 %. For THF on the other hand, decrease with increase in stoichiometric conc. towards a minimum value around 60 %.

As seen in Figure 26, the hydrate with THF has slightly higher estimated HTC than hydrate with EO at ≤ 40 % stoichiometric conc. of hydrates. Thereby, the degree of convection into hydrates, for both THF and EO, at lower concentrations is almost negligible (see the theory mentioned by Mohamed in section 2.4.3).

4.5 Volume effects

The size effects in this present thesis are referred to the different volumes of the cells used in the study. The amount of water added in either of the cells is adjusted to keep the gas – liquid ratio (i.e. volume ratio) during experiments the same in both cells. Thus in the larger cell (cell #5) the mass of the cell body and water are larger than for the smaller cell (cell #0).

4.5.1 Comparing the responses of HCS in the smaller vs. the larger cell

When using two different cells with different dimensions, there is expected that the heat transfer rate (i.e. the slope of temperature vs. time) in the smallest cell is higher compared to the larger cell caused by the difference in the area (i.e. the estimate HTC value is higher for the small cell compared to the large cell). There is needed to do some comparisons of the HCSs between the cells (the small and large cell), of all chosen stoichiometric concentrations and at all chosen stirring rates. See Figure 27 and 28.

Figure 27 shows a comparison of the HCS performances in cell#0 and cell#5 at similar experimental conditions with respect to concentration of hydrate forming agent (THF and EO), stirring rate, bath heating / cooling gradients and ramping temperatures. Figure 27A shows that the small cell has higher heat transfer rate compared to the large cell (called ideal case). Figure 27B shows HCS performed, where the small cell has identical heat transfer rate during heating as the big cell, and different heat transfer rate during cooling. Figure 27C shows HCSs performed, where the heat transfer rates during both cooling and heating is identical, caused by dissociation and re-formation effects.

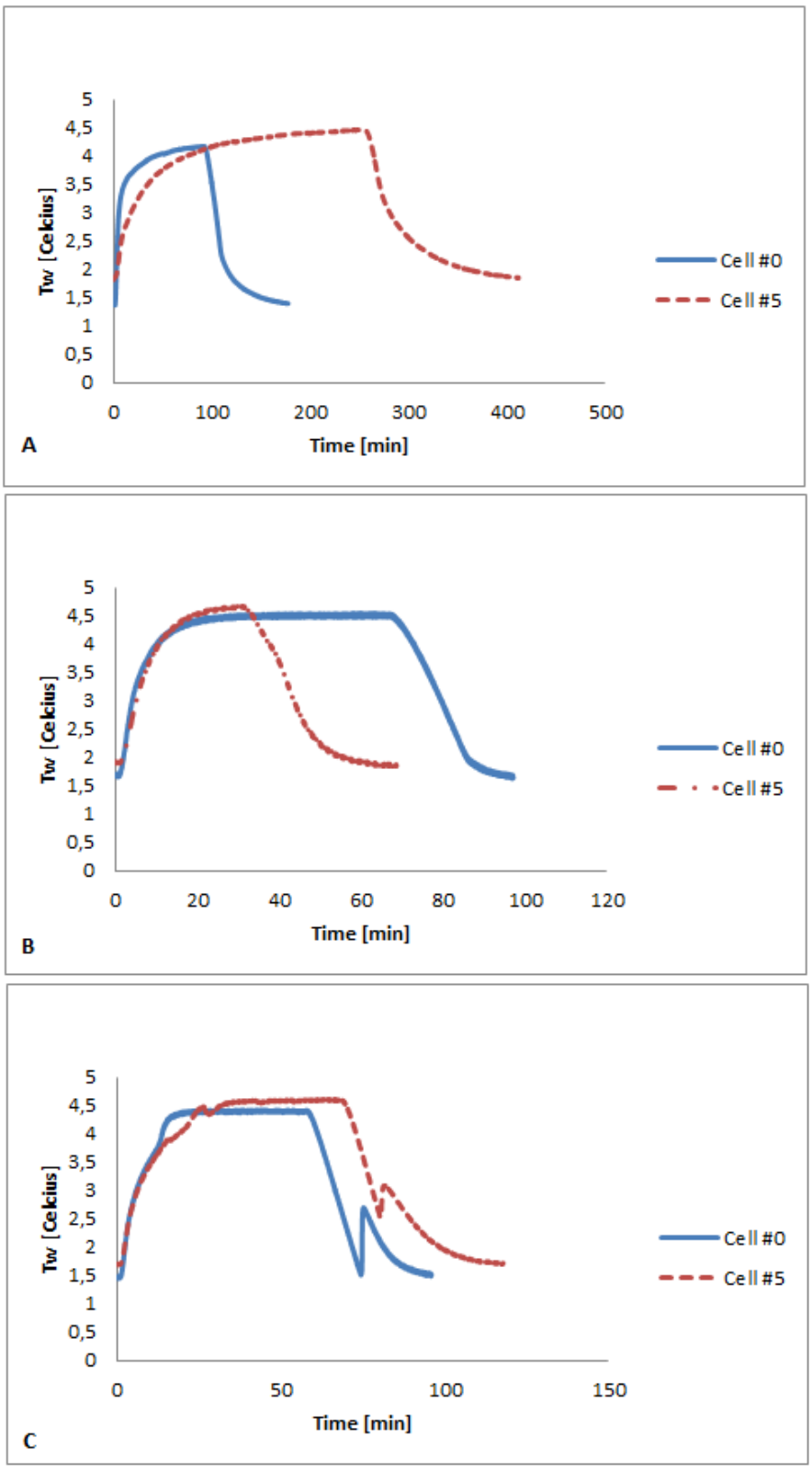

Figure 27: An illustration of how the experimental HCS looks like in both cell #0 and cell #5, when having these cases: (A) ideal, (B) same steepness of the heating sequence and (C) formation and dissociation (phenomena 1 and 2).

In the system with 40 % stoichiometric conc. of EO, the small cell has steeper slope than big cell during heating, but not cooling (see Figure 27B). The cells have parallel slopes during heating and cooling, in the case of 40 % stoichiometric conc. of THF (see Figure 27C), caused by formation and dissociation of hydrates.

The heat rate of the system is bigger for the small case, with a system with stirring at 0 and 80 % stoichiometric conc. of THF and EO. Without stirring, all the chosen concentrations have identical trend, the heat transfer rate is biggest in the small cell.

4.5.2 Effect of stirring rate

4.5.2.1 Baselines (0 % stoichiometric conc. of hydrates)

Figure 28 illustrates the relation between the estimated HTC and the stirring rate at similar conditions (e.g. gas –liquid ratio) in cell #0 and cell #5.

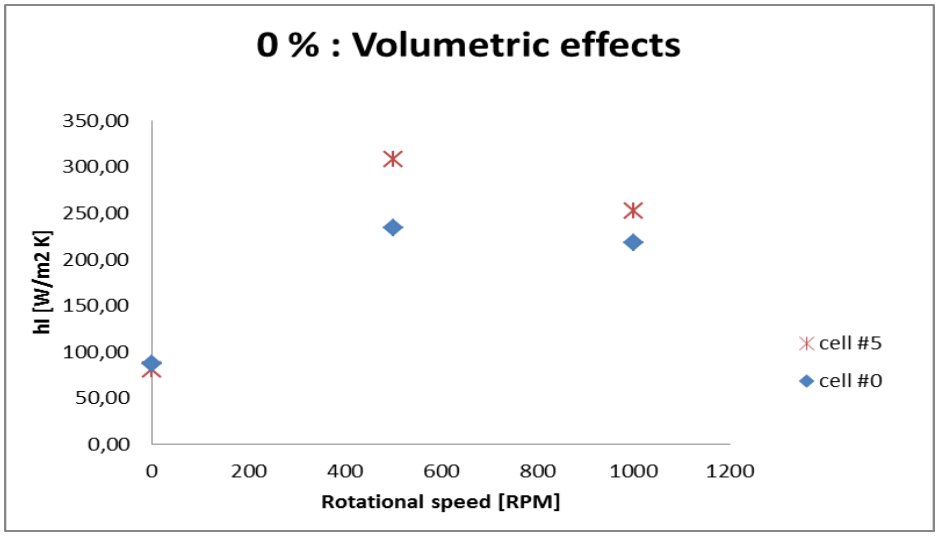

Figure 28: Volume effects on simulated HTC of 0 % stoichiometric conc. of THF (cell #0 and cell #5).

The comparison shows that the big cell produce more heat release compared to the small cell. In both cells, the estimated HTC increase with increase in stirring rate towards some optimum. It is observed that the HCSs for 0 % stoichiometric conc. of THF/EO, at all stirring rates, the slope of the small cell is steeper than the big cell (as seen in Figure 27A). Therefore, the values of the estimated HTC in the small cell compared to the big cell are expected to be higher. When compare the result of the estimated HTCs (appendix C.1) and the HSCs, the

case with no stirring have the values expected, but with stirring, the estimated HTC is highest in the big cell.

4.5.2.2 THF

Figure 29 illustrates the result from 40 % stoichiometric conc. of THF, when looking at the relation between the estimated HTC and the stirring rate, at different cell volumes (cell #0 and cell #5).

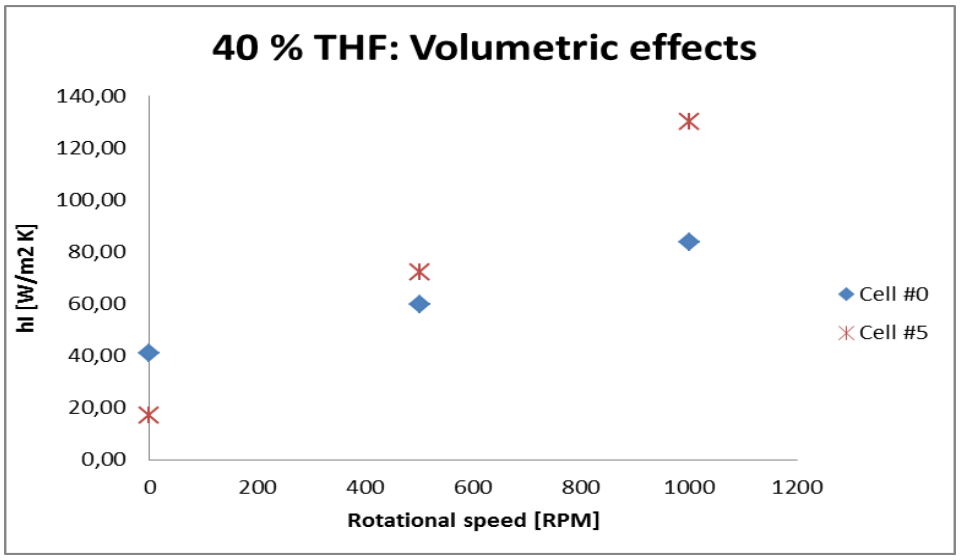

Figure 29: Volume effects on simulated HTC of 40 % content of THF (cell #0 and cell #5).

The estimated HTC in both cells increase linearly with increase in rotational speed, most likely. In Figure 29, the big cell has a steeper slope than the small cell. This shows that the estimated HTC is more affected by the stirring rate in the big cell compared to the small cell. The bigger the cell size thus larger effects of the rotational speed.

It is observed that the HCSs for 40 % stoichiometric conc. of THF, at no stirring, the slope of the small cell is steeper than the big cell (as seen in Figure 27A). Therefore, the values of the estimated HTC in the small cell compared to the big cell are expected to be higher. When compare the result of the estimated HTCs (appendix C.2) and the HCSs, the case with no stirring have the values expected, but with stirring, the estimated HTC is highest in the big cell. This can be caused by the formation and dissociation effects seen in Figure 27C.

Figure 30 shows the relation between estimated HTC and the stirring rate of different cell volumes at 80 % stoichiometric conc. of THF (cell #0 and cell #5).

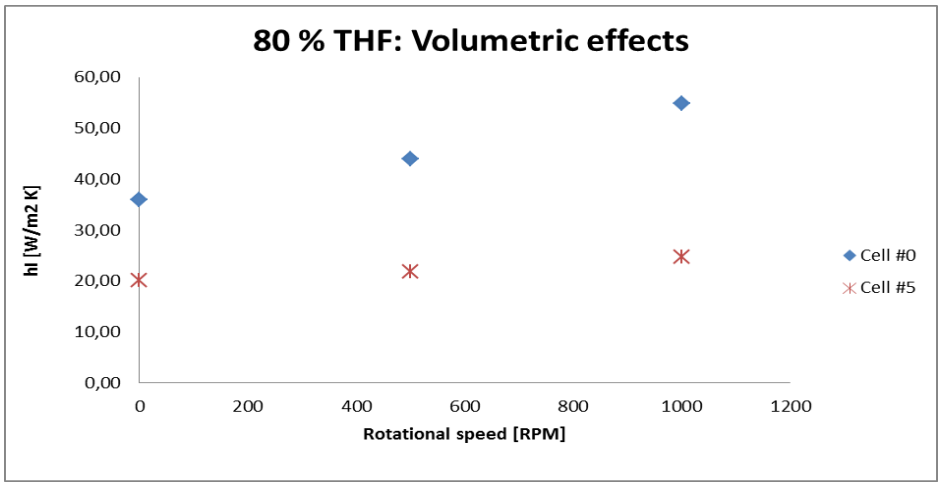

Figure 30: the volumetric effects on estimated HTC of 80 % content of THF (cell #0 and cell #5).

The estimated HTC is almost constant with increase in rotational speed, in the big cell. The estimated HTC increases with increasing rotational speed, in the small cell.

The reason why the estimated HTC in the big cell is almost constant can be affected by more conduction in the system, since conduction is less affected by the rotational speed (see theory in section 2.4.4).

At all stirring rate, the values of the estimated HTC in the small cell are higher than the values of estimated HTC in the big cell (see appendix C.2). Also the HCS relation between the two cells is following the ideal case; steeper slope for the small cell than the big cell, shown in Figure 27A.

4.5.2.3 EO

Figure 31 shows the relation between the estimated HTC and the stirring rate of different cell volumes at 40 % stoichiometric conc. of EO (cell #0 and cell #5).

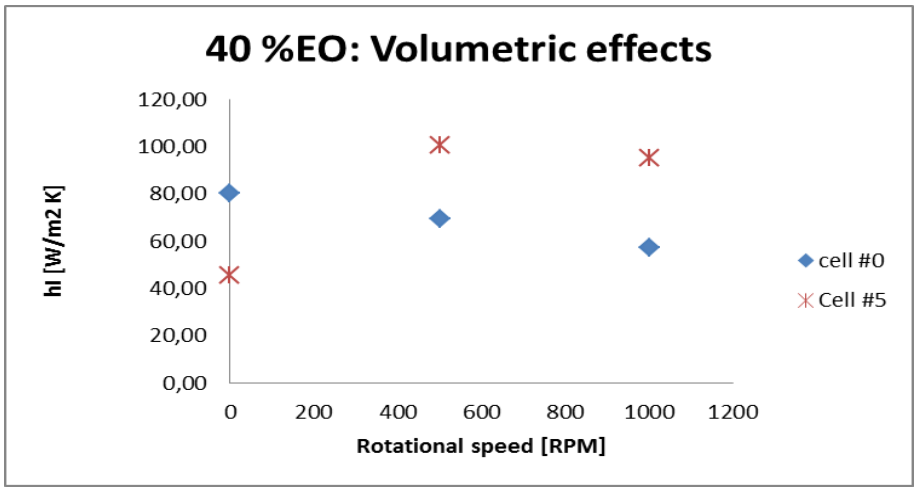

Figure 31: Volumetric effects on simulated HTC of 40 % content of EO (cell #0 and cell #5).

It can be seen in Figure 31, that the estimated HTC of 40 % stoichiometric conc. of EO have different outcomes in the cells. The small cell shows that the estimated HTC decrease with increasing rotational speed, but the estimated HTC in the big cell increase with increasing rotational speed.

It is observed that the HCSs for 40 % stoichiometric conc. of EO, at no stirring, the slope of the small cell is steeper during cooling and identical during heating compared to the big cell (as seen in Figure 27B). Therefore, the values of the estimated HTC in the small cell compared to the big cell are not as expected. When compare the result of the estimated HTCs (appendix C.3) with the HCSs, the case without stirring has higher estimated HTC values for the small cell compared to the larger cell. With stirring, the estimated HTC is highest in the big cell. This can be affected by the heating sequence which has parallel slopes when comparing the small and the big cell (seen in Figure 27B).

Figure 32 shows the relation between estimated HTC and the stirring rate of different cell volumes at 80 % stoichiometric conc. of EO (cell #0 and cell #5).

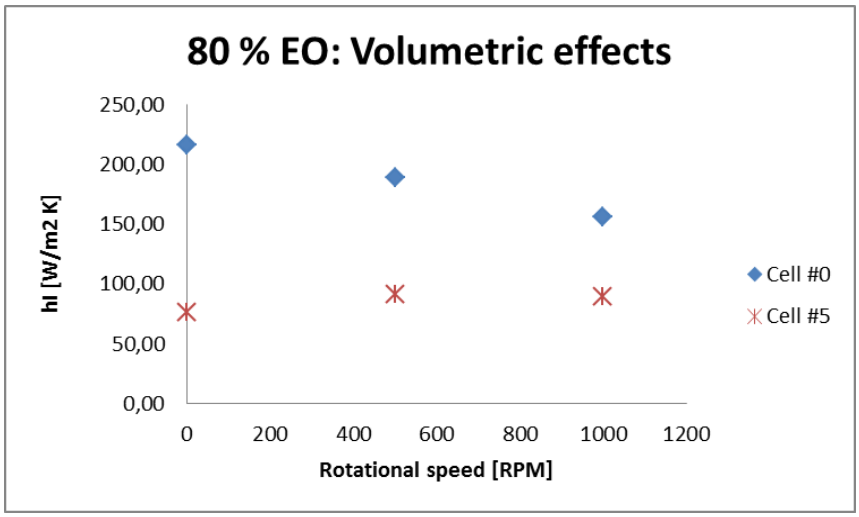

Figure 32: Volumetric effects on estimated HTC of 80 % content of EO (cell #0 and cell #5).

The reason why the estimated HTC in the big cell is almost constant can be affected by more conduction in the system, since conduction is less affected by the rotational speed (see theory in section 2.4.4).

At all stirring rate, the values of the estimated HTC in the small cell are higher than the values of estimated HTC in the big cell (see appendix C.3). Also the HCS relation between the two cells is following the ideal case; steeper slope for the small cell than the big cell, shown in Figure 27A.

4.5.2.4 THF vs. EO

Figure 33 shows the relation between the estimated HTC and rotational speed in different cell volumes, comparing THF and EO (cell #0 and cell #5).

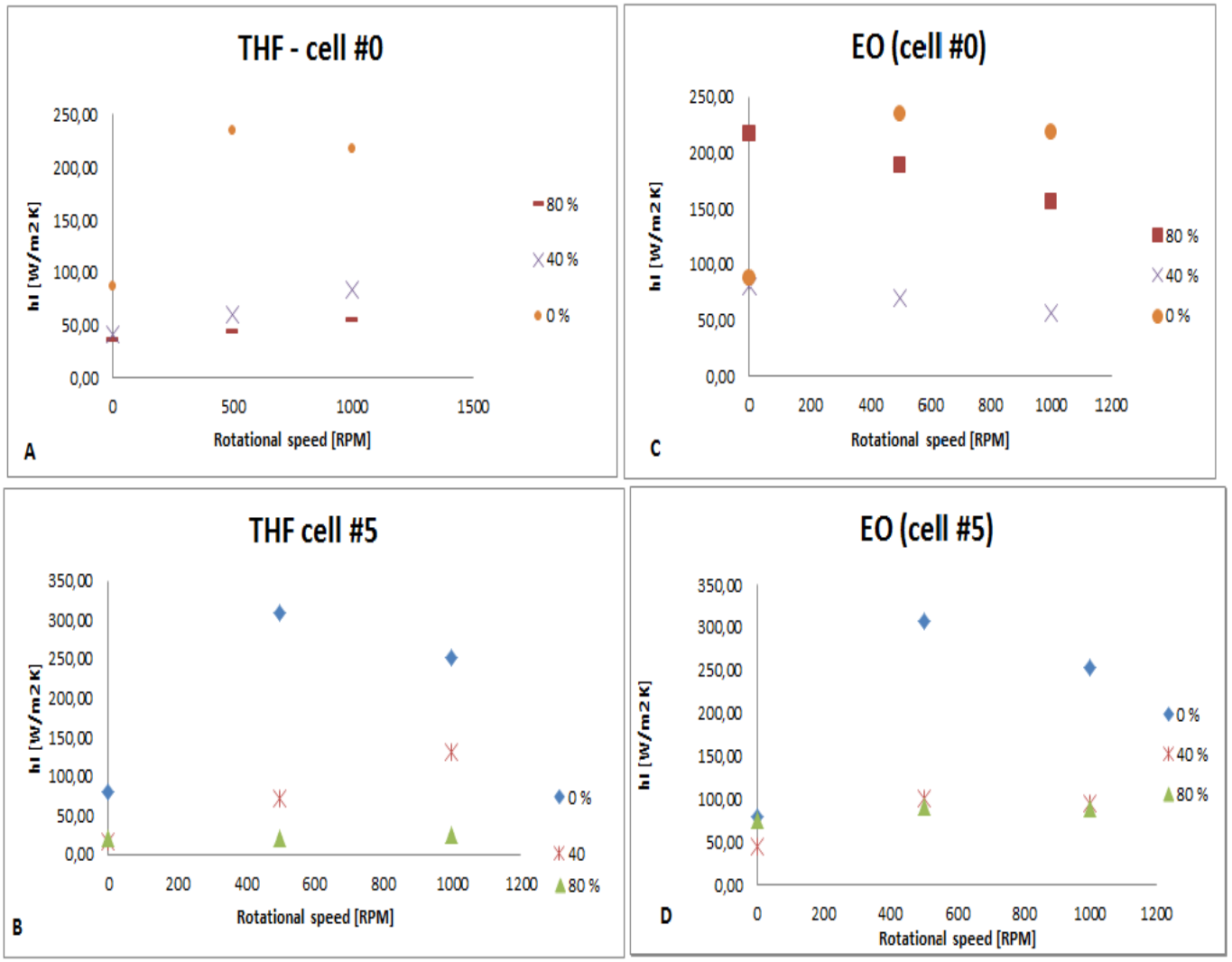

Figure 33: Volumetric effects on different rotational speeds of both THF and EO in cell #0 and cell #5.

With no stirring, the estimated HTC is following the same pattern in all of the cases (Figure 33A-D). With stirring, the pattern of the estimated HTC increases with increasing stirring rate for Figure 33A, B and D. This is not the case for EO hydrate, in the small cell. This means that EO and THF have different response when changing the area of the cell. Therefore, the estimated HTC in EO hydrate is more dependent of the stirring rate in a bigger sized cell than a smaller sized cell.

Without stirring, 80 % stoichiometric conc. of THF and 40 % stoichiometric conc. of EO in both of the cells have the lowest value of the estimated HTC. With stirring, 80 % stoichiometric conc. for both EO and THF in the big cell has the lowest estimated HTC value.

In the smallest cell while stirring, 80 % stoichiometric conc of THF and 40 % stoichiometric conc. of EO have the lowest value of estimated HTC.

The THF in both cells, the estimated HTC increase with increasing stirring rate, which is the same as vertical cylinders in steamer (see section 2.4.3) The EO hydrate in the small cell, the estimated HTC is decreasing with increasing stirring rate, mainly, and the estimated HTC in the big cell increase with increase in stirring rate. The EO follows both horizontal and vertical cylinders in a steamer, respectively (see section 2.4.3). The cases with no stirring, and EO hydrate in the small cell, the estimated HTC follows a pattern like anticline when the stirring rate increases. The reason can be explained by a phenomena called; “Laminarization” (see section 2.4.3). The 80 % stoichiometric conc. of THF, in both of the cells, has the highest conductional heat transfer. For EO hydrate, 80 % stoichiometric conc has higher conductional heat transfer in the big cell, and 40 % stoichiometric conc has higher conductional heat transfer in the small cell. (See section 2.4.4.)

4.5.3 Changing stoichiometric concentration of the solute

4.5.3.1 THF

Figure 34 shows the volumetric effects on estimated HTC and stoichiometric conc. of THF at different rotational speeds (0 RPM, 500 RPM and 1000 RPM) in the small cell and the big cell.

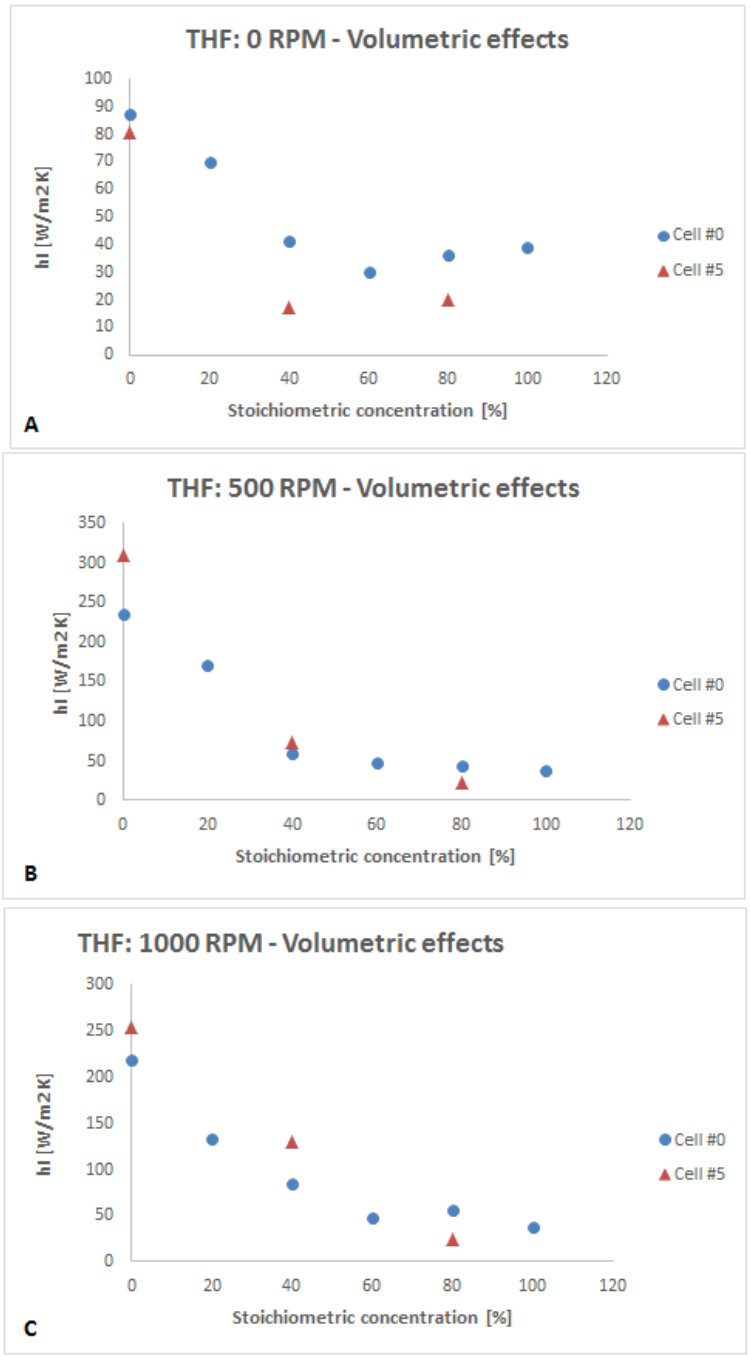

Figure 34: The volumetric effects on estimated HTC of THF at (A) 0 RPM, (B) 500 RPM, and (C) 1000 RPM. (Cell #0 and cell #5.)

At 0 RPM the estimated HTC can be explained by conduction. In both of the cells the estimated HTC decrease with increase in stoichiometric conc. of THF. The values of the estimated HTC given by the big cell are lower than the small cell. During stirring, the estimated HTC decrease with increase in stoichiometric conc. of THF, in both of the cells, just like the case without stirring. In the case of 500 RPM, the estimated HTC values are

almost the same for both cells. In the case of 1000 RPM, the big cell has higher values of the estimated HTC than the small cell.

In all of the cases (Figure 34A-C), the THF hydrate and methane hydrate have the same pattern of the estimated HTC vs. stoichiometric conc. (see section 2.4.2). Without stirring, the big cell represents a higher degree of conduction than the small cell. During 500 RPM, both of the cells have equal domination by conduction. And during 1000 RPM, the small cell represents a higher degree of conduction than the big cell. (See section 2.4.4)

4.5.3.2 EO

Figure 35 shows the volumetric effects on estimated HTC and stoichiometric conc. of EO hydrate at different rotational speeds (0 RPM, 500 RPM and 1000 RPM) in small and the big cell.

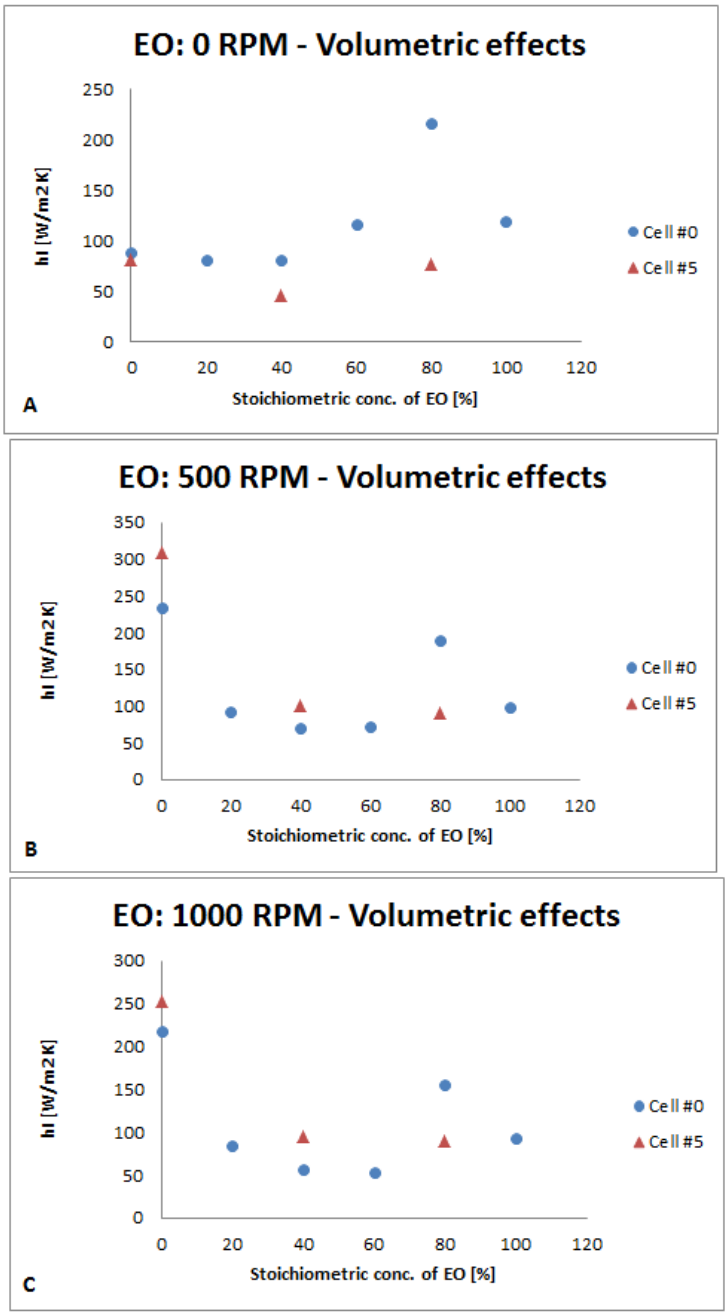

Figure 35: Volumetric effects on simulated HTC of EO at (A) 0 RPM, (B) 500 RPM, and (C) 1000 RPM.

At 0 RPM the estimated HTC can be explained by conduction, especially at lower stoichiometric conc. of EO. In both of the cells, the estimated HTC vs. stoichiometric conc. of EO follows a pattern like inclination. The big cell has lower values of the estimated HTC than the small cell. During stirring, the estimated HTC decrease with increase in stoichiometric conc. of EO for the big cell, and for the small cell at stoichiometric conc. below 80 % the same pattern is shown for the estimated HTC. The values of the estimated HTC are higher for the big cell than the small cell, except at 80 % stoichiometric conc. of EO. When comparing

the small cell, the values of the estimated HTC is higher at 80 – 100 % stoichiometric conc. compared to 60 % stoichiometric conc. of EO. The estimated HTC value at 100 % stoichiometric conc. is decreased compared to 80 % stoichiometric conc., when use EO as solute. The estimated HTC value at 80 % stoichiometric conc. of EO, the big cell has lower value compared to the small cell.

In case of 0 RPM, the big cell is more conducted compared to the small cell. During stirring, the small cell is more conducted than the big cell, below 80 % stoichiometric conc. of EO. At stoichiometric conc. of EO, the big cell is more conducted than the small cell. (See section 2.4.4.) Below 80 % stoichiometric conc. of EO, the estimated HTC is following the same pattern as methane hydrate (see section 2.4.2). The high "jump" in the estimated HTC value at 80 % stoichiometric conc. of EO can be affected by a sudden increase in viscosity causing an increase in the Re, but since the same "jump" is shown for 0 RPM as well, the increase in Re is negligible. In a system with 80 % stoichiometric conc. of EO, the estimated HTC is much higher for the large cell than the small cell. Thereby, errors in the method used, the equipment, etc is hard to distinguish. The value of 80 % stoichiometric conc. of EO is considered neglected.

4.5.3.3 THF vs. EO

Figure 36 shows the volumetric effects on estimated HTC and stoichiometric conc. of the hydrate (THF and EO) at different rotational speeds (0 RPM, 500 RPM and 1000 RPM) in different cell volumes (cell #0 and cell #5).

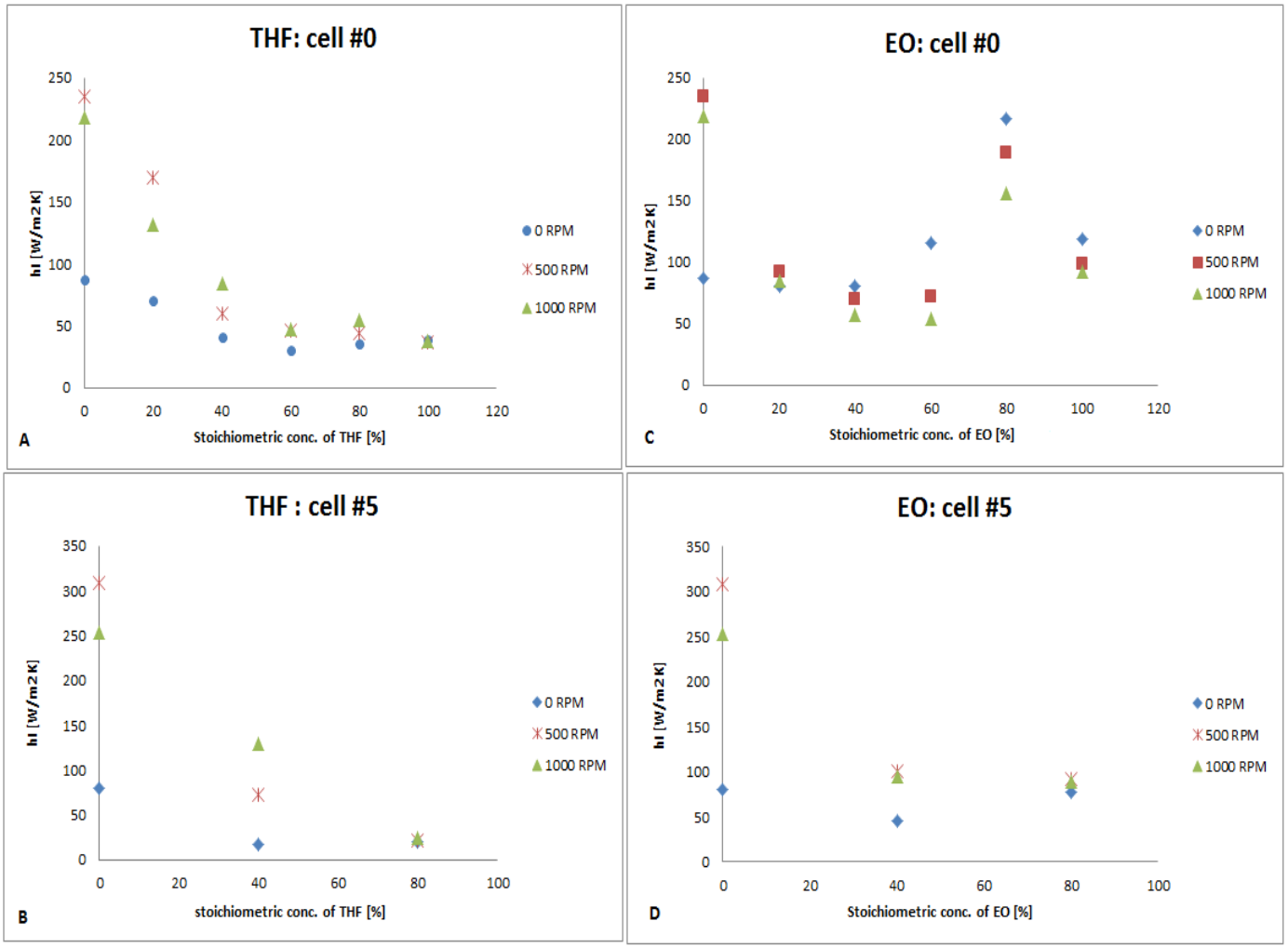

Figure 36: Volumetric effects on simulated HTC of: (A) THF cell #0, (B) THF cell #5, (C) EO cell #0 and (D) EO cell #5.

At 0 RPM, the estimated HTC decrease with increase in stoichiometric conc. of THF. For EO, there is some inconsistency of the pattern of the estimated HTC vs. stoichiometric conc. In general, the THF hydrate has lower estimated HTC values than the EO hydrate. With stirring, the estimated HTC decrease with increase in stoichiometric conc. of the solute, except in the small cell above 60 % stoichiometric conc. of EO. THF hydrate in general, tends to have lower values of the estimated HTC than EO hydrate.

The differences in the cell size affects THF hydrate and EO hydrate in the same way – the small cell has lower values of the estimated HTC than the big cell, when look at stoichiometric conc. of EO below 80 % in the small cell. The concentration effects are not affected by the volume of THF hydrate, but of EO hydrate. You can see that the trend of

estimated HTC vs. stoichiometric conc. is the same for THF, but not for EO when the volume of the cell is changing.

In Figure 35A-C, the estimated HTC vs. stoichiometric conc. of the solute have the same pattern as methane hydrate (see section 2.4.2). In general, THF hydrate is more conducted than the EO hydrate (see section 2.4.4).

4.6 Rotational speed effects

4.6.1 THF

Figure 37 shows the relation between estimated HTC and stirring rate at different stoichiometric conc. of THF (cell #0).

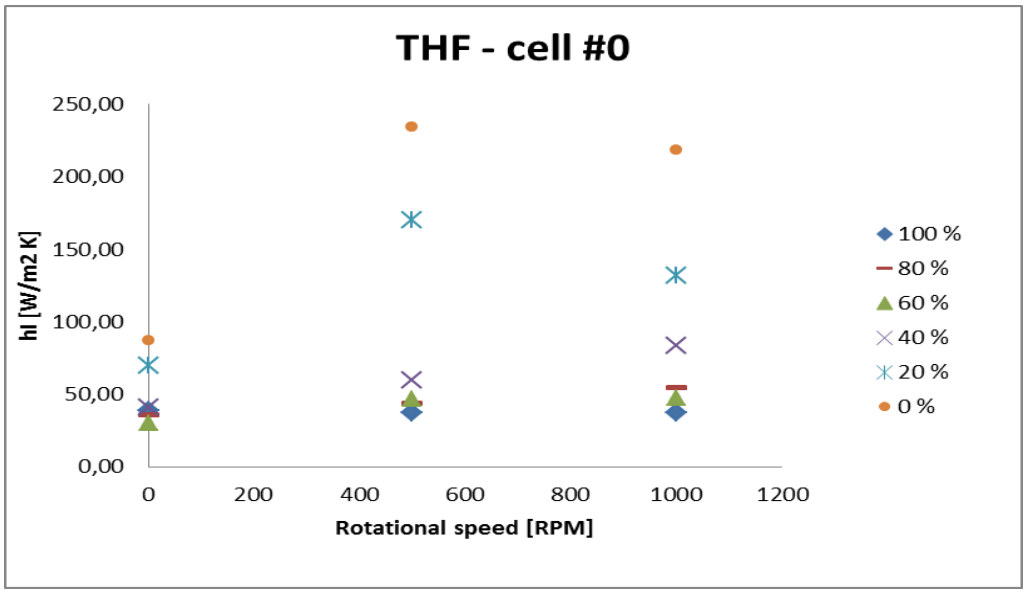

Figure 37: The effect of rotational speed on simulated HTC in THF-hydrates (Cell #0).

Without stirring, the estimated HTC is highest for 0 % stoichiometric conc. of THF and lowest for 60 % stoichiometric conc. of THF. With stirring, the value of the estimated HTC is lowest for 100 % stoichiometric conc. of THF, and highest for 0 % stoichiometric conc. of THF.

In the cases of 0 – 20 % - and 60 % stoichiometric conc. of THF: the estimated HTC increase between 0 – 500 RPM, and decrease between 500 – 100 RPM. In the cases of 40 % - and 80

% stoichiometric conc. of THF: the estimated HTC increase gradually with increase in rotational speed. In case of 100 % stoichiometric conc. of THF: the estimated HTC decrease gradually with increase in rotational speed.

Without stirring, 60 % stoichiometric conc. of THF is most conducted. With stirring, 100 % stoichiometric conc. of THF is most conducted. The above statement; 100 % stoichiometric conc. of THF is the most conducted when stirring, is reasonable when looking at Table 8.

It is said that having a miscible solution of THF and water, the heat transfer rate is dependent on the stirring rate. So by looking at figure 37, this can be correct. (See section 2.4.4.) In the case of 40 and 80 % stoichiometric conc. of THF: the estimated HTC vs. RPM is the same as seen in a steam chamber of vertical cylinders. The case of 0, 20 and 60 % stoichiometric conc. of THF: the estimated HTC vs. RPM is the same as seen in steam chamber of horizontal cylinders. (See section 2.4.3 for more details.) “Laminarization” can be the case where the estimated HTC decrease with increase in rotational speed, as seen for 100 % stoichiometric conc. of THF, and between 500 – 1000 RPM in the case of 0, 20 and 60 % stoichiometric conc. of THF (see section 2.4.3). In case of 0 – 40 % stoichiometric conc. of THF the values of the estimated HTC is higher than the values of estimated HTC in higher stoichiometric conc. of THF. Therefore, lower stochimetric conc. of THF is more affected by convection than higher stoichiometric conc. of THF (see section 2.4.4).

4.6.2 EO

Figure 38 shows the relation between estimated HTC and stirring rate at different stoichiometric conc. of EO (cell #0)

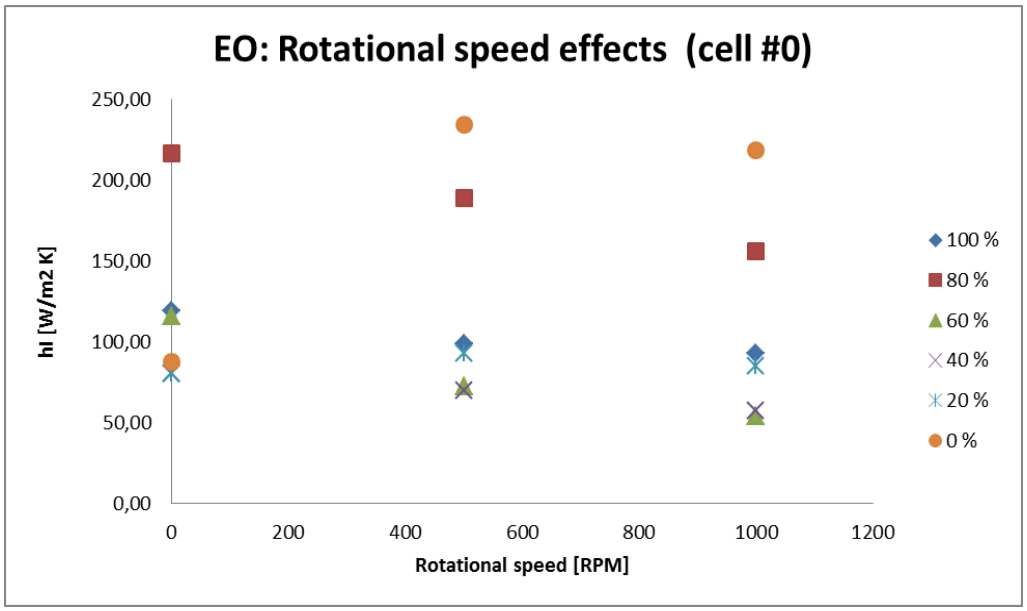

Figure 38: The rotational speed effects on simulated HTC in EO hydrates (cell #0).

Without stirring: 80 % stoichiometric conc. of EO has the highest value of the estimated HTC, and 0 – 20 % stoichiometric conc. of EO has the lowest value of the estimated HTC. With stirring: 0 % stoichiometric conc. has the highest value of the estimated HTC, and 40 – 60 % has the lowest value of the estimated HTC.

In figure 38, the different stoichiometric conc. of EO in the system, the estimated HTC decreases with increasing rotational speed, except from 0 % stoichiometric conc. of EO.

Without stirring, 0 - 20 % stoichiometric conc. of EO is most conducted. With stirring, 40 - 60 % stoichiometric conc. of EO is most conducted. The above statement; 40 - 60 % stoichiometric conc. of EO is the most conducted when stirring, is reasonable when looking at table 10, where the hydrate is wet and sticky.

In the case of 0 % stoichiometric conc. of EO: the estimated HTC vs. RPM is the same as seen in a steam chamber of horizontal cylinders. (See section 2.4.3 for more details.) “Laminarization” can be the case where the estimated HTC decrease with increase in rotational speed, as seen for 40 -100 % stoichiometric conc. of EO (see section 2.4.3). The decrease in the estimated HTC with increase in rotational speed can be affected by the Reynolds number, where the viscosity decreases.

4.6.3 THF vs EO

Figure 39 shows the relation between estimated HTC and stirring rate at different stoichiometric conc. of hydrate, comparing THF and EO (cell #0).

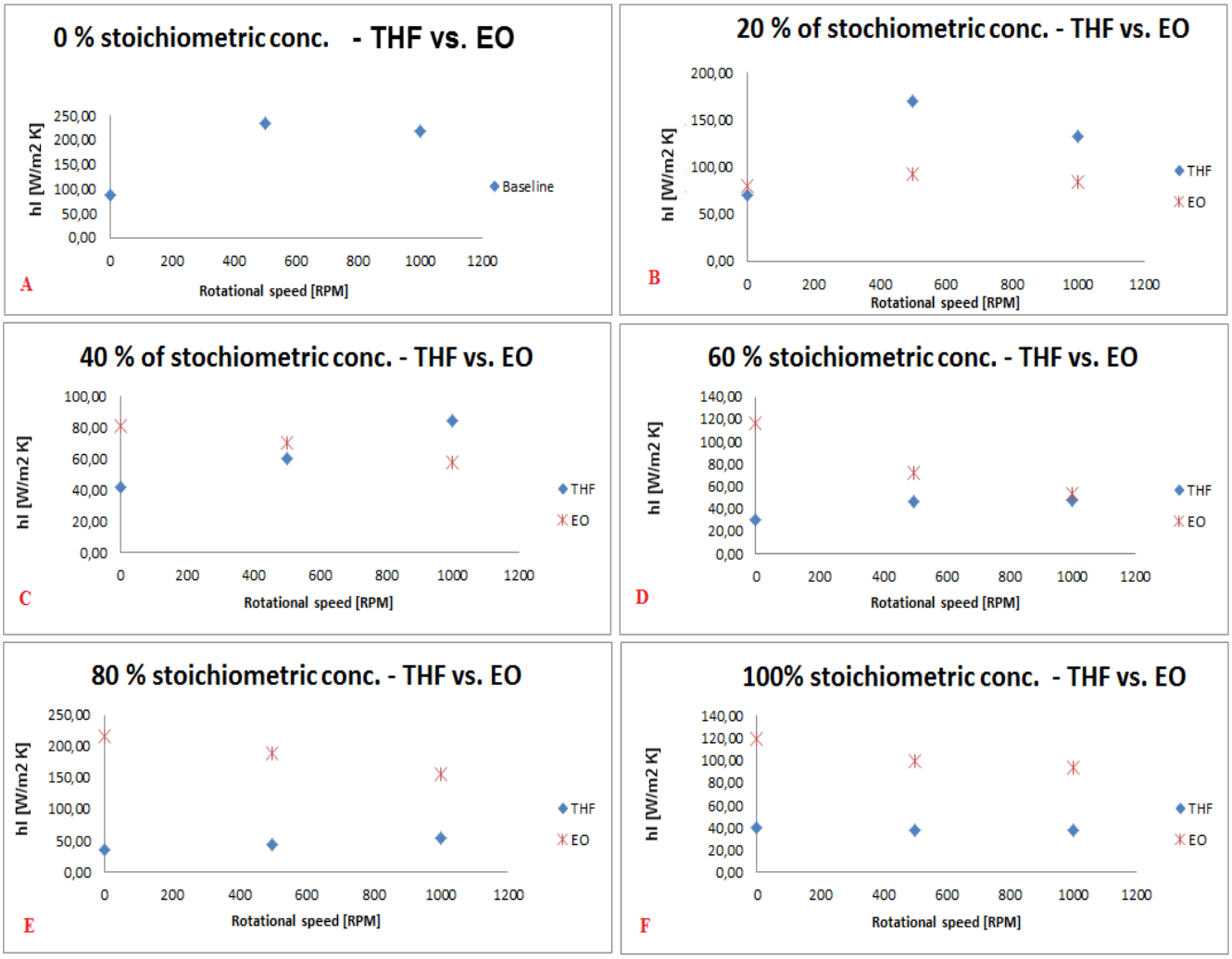

Figure 39: The effect on rotational speed on simulated HTC in different amounts of hydrates of both THF and EO (cell #0); (A) 0 %, (B) 20 %, (C) 40 %, (D) 60 %, (E) 80 % and (F) 100 %.

Without stirring, EO hydrate, of 20 – 100 % stoichiometric conc., has higher value of the estimated HTC than THF hydrate. With stirring, at 60 – 100 % stoichiometric conc. of solute, EO hydrate has higher values of the estimated HTC than THF hydrate. With stirring, 20 % stoichiometric conc. of solute, THF hydrate has higher values of the estimated HTC than EO

hydrate. Art 40 % stoichiometric conc. of solute, the value of estimate HTC is higher for EO hydrate at 500 RPM, and lower at 1000 RPM compared to THF hydrate.

In the cases of 40 – 100 % stoichiometric conc. of solute: The estimated HTC increase with increasing stirring rate for THF hydrate, and estimated HTC decrease with increasing stirring rate for EO hydrate. In case of 0 – 20 % stoichiometric conc. of solute: the estimated HTC vs. stirring rate follow a trend like inclination for both EO and THF hydrate.

In case of 40 – 100 % stoichiometric conc. of the solute: the estimated HTC vs stirring rate is follow the same pattern as vertical cylinders in a steamer for THF hydrate, and EO hydrate is following the pattern as the "laminarization" phenomena (see section 2.4.3). In the case of 0 – 20 % stoichiometric conc. of solute: Both THF and EO hydrate is following the same trend of the estimated HTC vs. stirring rate as horizontal cylinders in a steamer (see section 2.4.3).

When comparing the Figure 39 and the data given in appendix for a system without stirring, the 100 % stoichiometric THF hydrate has a lower thermal conductivity than water. EO on the other hand, 100 % stoichiometric, has a slightly higher thermal conductivity than water. For both systems, 100 % stoichiometric concentration of THF and EO, the estimated HTC is almost identical when change in stirring. With 60 and 80 % stoichiometric concentration of THF, the estimated HTC increase slightly with increase of stirring, therefore, the convective heat transfer is marginal. On the other hand, a system with 40 % stoichiometric conc., the degree of convectional heat transfer is high when increase in stirring. Without stirring, the hydrate slurry is on contact with the cell wall. On the other hand, with stirring, the cell wall is in contact with the gas. This can affect the result of the estimated HTC and the thermal conductivity. The change in the thickness of the hydrate layer and or hydrate slurry is another factor affecting the thermal conductivity.

A system with 20 % stoichiometric concentration of THF, the convectional heat transfer is dominant, and the values of the estimated HTC are increasing toward the value of water. The difference between the water and 20 % stoichiometric conc. of THF can be related to the THF-water solution without hydrates present, in all probability.

4.7 Uncertainties

4.7.1 Temperature sensors

During a calibration test (see section 3.1.3) the temperature sensors in the water phase showed higher temperature than expected. The temperature sensors can have an accuracy of ± 0.03 °C, the assumed accuracy of measurements connected in line is 0.1°C, but the test showed Tw of 0.17°C and o.18°C at 0°C for cell #5 and #0, respectively. The calculated temperature difference between the outer and inner boundary is higher than the actual temperature difference.

The simulation method is assumed to have radial heat transfer, only. The estimated HTC is based on the experimental temperatures between the outer and inner boundary of the cell. Therefore, the simulations done can be affected by the difference in the actual temperature and the measured temperature of the water phase.

4.7.2 Different coolant fluid

Both water - glycol (max. 5% of glycol) and distilled water were used as coolant compound, in cell #5 and cell #0, respectively. This needs to be taken in consideration when looking at the volume effects.

4.7.3 Condensation effects

In this present work low temperatures are used during heat transfer experiments, thereby, condensation at the outer wall and top lid is observed. The simulation method assumed radial heat transfer, so the condensation effects are not considered in this study.

5 CONCLUSION

When the stoichiometric concentration of the solute, THF or EO, is less than 20 % the hydrate formation is hard to accomplish. With use of 40 % stoichiometric concentration of THF, hydrates have been formed, but during heating and cooling, hydrates have been dissociated and re-formed, respectively, affecting the simulation results.

The hydrate structure of THF between 20 – 100 % stoichiometric concentrations is observed to change from slurry to a dry hydrate film, respectively. For EO hydrate, the same outcome is observed. The stability of the hydrate throughout the heat transfer experiments is controlled by the stoichiometric concentration and temperature. It has been observed; EO hydrates have a more stable hydrate structure than THF hydrates.

For both EO system and THF system, the heat transfer coefficient of the hydrate in slurry (h_I) decreases with increasing stoichiometric concentration, independent of the cell size.

A system with THF present h_I decreases with increasing stirring rate, independent of the cell size. It is observed that h_I decreases with increasing the thickness of the hydrate layer, and that the thermal conductivity is greater for a dry porous hydrate layer than for a wet hydrate layer. On the other hand, a system with EO present, h_I increase with increasing stirring rate, independent of the cell size. It is observed that h_I increases with increasing the thickness of the hydrate layer, and the thermal conductivity is greater for a wet hydrate layer compared to a dry hydrate layer.

6 FUTURE WORK

The heating or cooling sequence (HCS) should be leveled out in at least 15-20 minutes before stop running.

In this present work, several heating and cooling sequences in a row (more than 3) have a tendency of melt more hydrates, especially without stirring. In the future, do 3 or less heating and cooling sequences in a row.

Now, only few CFD (Computational Fluid Dynamics) simulations have been performed on heat transfer effects on hydrate formation. (Note: There has been done some work on a CFD analysis in a propane hydrate system. (Jassim, Abdi, & Muzychka, 2010)) CFD analysis will be advantageous, because the geometry of the system and heat properties can be found.

Instead of only using the coolant temperature as an outer boundary, the temperature at the wall within the cell will be of great interest, for improving the simulation model. To do so, detect the temperature at the wall within the cell additionally.

If using EO/THF, there should be detected the hydrate generation within the temperature range used (to see if there is hydrate generation or not) – and/or choose a temperature range where you know there is no hydrate generation (by several observation while detect the hydrate generation) (The simulation model only take cares of the entire heating and cooling sequence.) In the future, the model can be able to calculate the heat transfer coefficient of the slurry, with use of partial heating and cooling sequences, if possible.

The simulation model is based on only radial heat transfer. The model should take care of the axial heat transfer as well as the radial.

The simulation model used does not take in consideration which type of hydrate structure, slurry of a hydrate layer, present. In the future, it will be advantageous using a model based on the different hydrate structures present.

7 REFERANCES

Abay, H. K., & Svartaas, T. M. (2010). Effect of ultralow concentrations of methanol on methane hydrate formation. *Energy & Fuels, 24*, 752 - 757.

Abay, H. K., Svartaas, T. M., & Ke, W. (2011). Effect of gas consumption on sII hydrate growth kinetics. *Energy & Fuels, 25*, 1335 - 1341.

Arjmandi, M., Ren, S., & Tohidi, B. (2005). *Proceedings of the 5th International Conference on Gas Hydrates, Paper4011*, 1178-1184.

Ashworth, T., Johnson, L. R., & Lai, L.-P. (1984). Thermal conductivity of pure ice and tetrahydrofuran clathrate hydrates. *Proceedings of the 9th European Thermophysical Properties Conference, 17*, 413 - 419.

Baez, L. A., & Clancy, P. (1994). Computer Simulation of the Crystal Growth and Dissolution of Natural Gas Hydrates. In E. D. Sloan Jr, J. Happel & M. A. Hnatow (Eds.), *International conference on natural gas hydrates* (Vol. 715, pp. 177 - 186). New York: Anneals of The New York Academic of Science.

Berg, W. F. (1938). *Proc.Roy.Soc, A164*, 79.

Berthoud, A. (1912). *J.de Chim.Phys., 10*, 624.

Bird, R. B., Stewart, W. E., & Flightfoot, E. N. (1960). Transport phenomena. *Wiley & sons inc.*

Boe, R. (2014, February - June). [Heat transfer].

Bollavaram, P., Devarakonda, S., Selim, M. S., & Sloan Jr, E. D. (2000). Growth kinetics of single crystal sII hydrate; elimination of mass and heat transfer effects In G. D. Holder & P. R. Bishnoi (Eds.), *Gas hydrates: Challenges for the future* (Vol. 912, pp. 533 - 543). New York, NY: Anneals of the New York Academy of Science.

Borgnakke, C., & Sonntag, R. E. (2009). *Fundamentals of thermodynamics* (7 ed.). Hoboken, NJ: Wiley.

Bunn, C. W. (1949). *Discussion faraday soc., 5*, 132.

Camargo, R., & Goncalves, M. (2004). *Proceedings in OTC*.

Christiansen, R. L., & Sloan Jr, E. D. (1994). *Proc. Annual convention of gas processors association, 74*, 15.

Creek, J., Douglas, E., & Subramanian, S. (2011). Project design hydrate management by application of multiphase flow simulationtools with hydrate formation and transport. *Proceedings of the 7th International Conference on Gas Hydrates*.

Davies, S. R., Selim, M. S., Sloan, E. D., Bollavaram, P., & Peters, D. J. (2006). *AIChE, 52*, 4016.

Davy, H. (1811). The bakerian lecture. On some of the combinations of oxymuriatic gas and oxygen, and on the chemical relations of these principles to inflammable bodies. (part I), 1-35, 101.

Deaton, W. M., & Frost, E. M. (1946). Gas hydrates and their relation to the operation of natural-gas pipe lines. *U.S Bureau of Mines Monography, 8*, 101.

Dever, J. P., George, K. F., Hoffman, W. C., Soo, H., & corp., U. c. (1994). Ethylene Oxide *Kirk-Othmer Concise Encyclopedia of chemical technology* (Vol. 9, pp. 915-959). New York: John Wiley & sons, Inc.

Dorstewitz, F., & Mewes, D. (1993). The influence of hydrate formation on heat transfer in gas pipelines. *Proceedings of the 6th International Symposium on Transport Phenomena in Thermal Engineering, 1*.

Dyadin, Y. A., Bondaryuk, I. V., & Zhurko, F. V. (1991). Inclusion compounds. *Oxford University Press, 5*.

Elwell, D., & Scheel, H. J. (1975). Crystal growth from high temperature solution (Überarbeitete Version von 1975 ed., Vol. 273, pp. 273). London: Academic press.
Englezos, P., & Bishnoi, P. R. (1988). Prediction of gas hydrate formation conditions in aqueous electrolyte solutions. *AIChE, 34*(10), 1728-1721.
Englezos, P., Kalogerakis, N. E., Dholabhai, P. D., & Bishnoi, P. R. (1987a). Kinetics of formation of methane and ethane gas hydrates. *Chem. Eng. Sci., 42*(11), 2647-2658.
Englezos, P., Kalogerakis, N. E., Dholabhai, P. D., & Bishnoi, P. R. (1987b). Kinetics of gas hydrate formation from mixtures of methane and ethane. *Chem. Eng. Sci., 42*(11), 2659-2666.
Englezos, P., & Servio, P. (2003). Morphology of methane and carbon dioxide hydrates formed from water droplets. *AIChE, 49*, 269-276.
Erva, J. (1956). *Suomen Kemistilehti, 29B*, 183.
Freer, E., Selim, M. S., & Sloan, E. D. (2001). Fluid phase equilibria. *185*, 65.
Glew, D. N., & Rath, N. S. (1965). *J. Chem.Phys., 44*, 1711.
Glew, D. N., & Rath, N. S. (1966). *J.Chem.Phys, 44*, 1710.
Glew, D. N., & Rath, N. S. (1995). Aqueous nonelectrolyte solutions. Part XIII. Ice and hydrate freezing points of aqueous ethylene oxide solutions and the formula of congruent ethylene oxide hydrate. *CA. J. Chem, 73*(6), 788-796. doi: 10.1139/v95-099
Haas, W. J. d. (1950). Water - thermal properties. Retrieved April 28, 2014, from http://www.engineeringtoolbox.com/water-thermal-properties-d_162.html
Hammerschmidt, E. G. (1934). Formation of Gas Hydrates in Natural Gas Transmission Lines. *Ind. Eng. Chem., 26*, 851-855.
Hawtin, R. W., & Rodger, P. M. (2006). Polydispersity in ogliomeric low dosage gas hydrate inhibitors. *J. Material chem., 16*(20), 1934-1942.
Hirai, S., Takagi, T., & Matsumoto, M. (1988). Predictions of the laminarization phenomena in an axially rotating pipe flow. *Trans ASME, 110*, 424-430.
Holman, J. P. (2010). *Heat Transfer* (10th ed.). New York: McGraw-Hill companies.
Hong, H., & Pooladi-Darvish, M. (2005). *J.Can.Petrol.Technol., 44*(11), 39.
Hong, H., Pooladi-Darvish, M., & Bishnoi, P. R. (2003). *J.Can.Petrol.Technol., 42*, 45.
Hovland, M., & Gudmestad, O. T. (2001). Potential influence of gas hydrates in seabed installations. *American geophysical union*, 307-315.
Huo, Z., Jager, M. D., Miller, K. T., & Sloan, E. D. J. (2002). Ethylene oxide hydrate non-stochiometry: measurements and implications. *Chem. Eng. Sci., 57*, 705 - 713.
Incropera, F. P., DeWitt, D. P., Bergman, T. L., & Lavine, A. S. (2007). *Introduction to heat transfer* (fifth ed.). Hoboken, N.J.: Wiley.
Jassim, E., Abdi, M. A., & Muzychka, Y. (2010). A new approach to investigate hydrate deposition in gas - dominated flowlines. *nat. gas sci. eng., 2*. doi: 10.1016/j.jngse.2010.05.005
Jynto. (2011). Ethylene Oxide 3D-balls. Retrieved 8th of March, 2014, from http://upload.wikimedia.org/wikipedia/commons/6/6c/Ethylene-oxide-3D-balls-2.png
Kashciev, D., & Firoozabadi, A. (2002). *J.Cryst.Growth, 243*.
Kaviany, M. (2002). *Principles of heat transfer*. New York: Wiley.
Kelland, M. A. (2006). History of the developement of low dosage hydrate inhibitors. *Energy & Fuels, 20*(3), 825 - 847.
Kelland, M. A. (2009). *Production Chemicals for the Oil and Gas Industry* (1 ed.). Boca Raton: Taylor & Francis Group.
Kvamme, B. (1996). Molecular dynamic simulation of PVP kinetic inhibitor in a liquid water and a hydrate/liquid water system. *Proceeding of 2nd International Conference on Gas Hydrates, 136*, 347 - 354.

Kvenvolden, K. A., & Claypool, G. E. (1985). Proceeding of the unconventional gas recovery. *gas hydrate peer review session*.
Larsen, R., Knight, C. A., Rider, K. T., & Sloan Jr., E. D. (1999). Melt growth and inhibition of ethylene oxide clathrate hydrate. *Crystal growth, 214*, 376 - 381.
Larsen, R., Knight, C. A., & Sloan, E. D. J. (1998). Clathrate hydrate growth and inhibition. *Fluid phase equilibria, 150 - 151*, 353 - 360.
Lee, J. Y., Yun, T. S., Santamarina, J. C., & Ruppel, C. (2007). Observations related to tetrahydrofuran and methane hydrates for laboratory studies of hydrate - bearing sediments. *Geochem. Geophys. Geosyst., 8*(6), 1-10. doi: 10.1029/2006GC001531
Lesist, D. G., Murray, J. J., Post, M. L., & Davidson, D. W. (1982). Enthalpies of decomposition and heat capacities of ethylene oxide and tetrahydrofuran hydrates. *Am. Chem. Soc., 86*(21), 4175 - 4176. doi: 2086-4175S01.25
Long, J. (1994). *Gas hydrate formation mechanism and its kinetic inhibition.* (PhD), Colorado School of Mines.
Loudon, G. M. (2002). *Organic chemistry* (4th ed.). New york: Oxford university press.
Mak, T. C. W., & McMullan, R. K. (1965). Polyhedral Clathrate Hydrate. X. Structure of the double hydrate of Tetrahydrofuran and hydrogen sulfide. *Chem. Phys, 42*(8), 2732 - 2737.
Makogon, T. Y., Larsen, R., Knight, C. A., & Sloan Jr., E. D. (1996). Melt growth of tetrahydrofon clathrate hydrate and its inhibition: method and first result. *Crystal growth, 179*, 258- 262.
Makogon, Y., Makogan, T., & Holditch, S. (1998). *Proceedings of the national oil conference in Japan, 259*.
Makogon, Y. F. (1965). Hydrates of natural gas (pp. 237). Moscow, Russia: PennWell Books. (Reprinted from: 1981).
Malegoankar, M. B., Dholabhai, P. D., Bishnoi, P. R., & Can, J. (1997). *Can. J. Chem. Eng, 75*(1090).
Malone, R. D. (1985). Mechanism for hydrate consolidation. *Courtesy of U.S dept. of energy*.
McKetta, J. J., & Cunningham, W. A. (1984) *Enclopedia of chemical technology elastomers synthetic to expert systems* (Vol. 20, pp. 309): CRC press.
McMullan, R. K., & Jeffrey, G. A. (1965). *Chem.Phys., 42*(2765).
Meindinyo, R.-E. T., Svartaas, T. M., & Boe, R. (2014a). Heat transfer during hydrate formation - an investigation on the effect og hydrate content on heat transfer coefficient of gas hydrate slurry. *Proceedings of the 8th International Conference on Gas Hydrates*.
Meindinyo, R.-E. T., Svartaas, T. M., Nordbø, T. N., & Boe, R. (2014b). Hydrate growth estimation from heat transfer - experimental results analysis. *Proceedings of the 8th International Conference on Gas Hydrates*.
Mochizuki, T., & Mori, Y. H. (2005). *Proceedings of the 5th International Conference on Gas Hydrates, Paper1009*.
Mochizuki, T., & Mori, Y. H. (2006). Cryst.Growth. *260*(642).
Mohamed, H. A. (2006). Effect of rotation and surface roughness on heat transfer rate to flow through vertical cylinders in steam condensation process. *Heat transfer, 128*(318 - 323).
Moon, C., Taylor, P. C., & Rodger, P. M. (2003). *Am.Chem.Soc, 125*, 4706.
Mori, Y. H. (2001). *Cryst.growth, 223*, 206.
Moridis, G. J. (2002). *SPE Gas technology symposium*, 75691.

Mork, M., & Gudmundsson, J. S. (2001). Rate of hydrate formation in subsea pipelines - correlation based on reactor experiments. *12th International Oil Field Chemistry Symposium*, 1-12.
Mullin, J. W. (1993). *Crystallization* (3rd ed.). Oxford, UK: Butterworth-Heimann.
Nicol, A. A., & Gacesa, M. (1970). Condensation of steam on rotating vertical cylinder. *J. Heat transfer, 92*, 144-152.
Nordboe, T. N. (2013). *Hydrate growth kinetics: a study on the relation between energy release rates and gas consumption rates during methane hydrate formation and growth.* (Master), T.N. Nordbø, Stavanger.
Parrish, W. R., & Prausnitz, J. M. (1972). Dissociation Pressures of Gas Hydrates Formed by gas mixtures. *Ind. Eng. Chem. Process Des. Dev., 11*(1). doi: 10.1021/i260041a006
Pooladi-Darvish, M. (2004). Gas production from hydrate reserves and its modeling. *Journal of petroleum technology, 56*(6), 65-71.
Priestly, J., & Pearson, T. (1790). Experiments and Observations on Different Kinds of Air and Other Branches of Natural Philosophy Connected with the Subject (pp. 359). Birmingham.
Radhakrishnan, R., & Trout, B. L. (2002). *Chem.Phys, 117*(1786).
Rao, I., Sloan, E. D., Koh, C. A., & Sum, A. K. (2011). Laboratory experiments & modeling for hydrate formation and deposition from water saturated gas systems. *Proceedings of the 7th International Conference on Gas Hydrates, Paper00055*.
Rehder, G., Kirby, S., Durham, B., Stern, L., Peltzer, E. T., Pinkston, J., & Brewer, P. (2004). *Geochimica Cosmochimica Acta, 68*, 285.
Ross, R. G., & Andersson, P. (1982). Clathrate and other solid phases in the tetrahydrofuran - water system: thermal conductivity and heat capacity under pressure. *Can. J. Chem, 60*(881). doi: 070881-12$01.00/0
Siegfried, R., & Dieter, M. (1987). Ethylene Oxide *Ullmann`s encyclopedia of industrial chemistry* (5th ed., Vol. A10, pp. 117-135). New York: VCH.
Singer, R. M., & Presckshot, G. W. (1963). The condensation of vapor on a horizontal rotating cylinder. *Proceedings of Ins.Heat transfer fluid mech., 14*, 205-211.
Skovborg, P., & Rasmussen, P. (1994). *Chem. Eng. Sci., 49*(1131).
Sloan, E. D., & Koh, C. A. (2008). *Clathrate hydrates of natural gases*. Boca Raton, Fla.: CRC Press.
Sloan, E. D., Koh, C. A., & Sum, A. K. (2011). *Natural Gas in Flow Assurance* (1 ed.). Burlington: Gulf Professional Publishing.
Sloan Jr, E. D. (2000). *Hydrate engineering* (1 ed.). Texas: Arco E&P technology Inc.
Subramanian, S. (2000). *Measurements of clathrate hydrates containing methane and ethane using Raman spectroscopy.* (Ph.D.), Colorado school of Mines, Golden, CO.
Svartaas, T. M. (2014, May). [Equilibrium melting point for THF].
Taylor, C. J. (2006). *Adhesion force between hydrate particles and macroscopic investigation of hydrtae film growth at the hydrocarbon/water interface.* (Master), Colorado school of mines, Golden, CO, USA.
Taylor, C. J., Dieker, L. D., Miller, K. T., Koh, C. A., & Sloan, E. D. (2006). *Colloid interface sci.*
Tombari, E., Presto, S., Salvetti, G., & Johari, G. P. (2006). Heat capacity of tetrahydrofuran clathrate hydrate and of its components, and the clathrate formation from supercooled melt. *Chem. Phys., 124*, 154507.
Torkildsen. (2013, 11th of october). water properties. from http://no.wikipedia.org/w/index.php?title=Vann&oldid=12705199

Trèhu, A. M., Ruppel, C., Holland, M., Dickens, G. R., Torres, M. E., Collett, T. S., . . . Schultheiss, P. (2006). Gas hydrates in marine sediments - lessons from scientific ocean drilling. *Oceanography, 19*(4).
Uchida, T., Ebinuma, T., Kawabata, J., & Narita, H. J. (1999a). Cryst. Growth. *204*(348).
Urieli, I. Specific heat capacities of air. Retrieved April 28, 2014, from http://www.ohio.edu/mechanical/thermo/property_tables/air/air_Cp_Cv.html
Valeton, J. J. P. (1924). *Zeit. fur Kristallog, 59*, 483.
Van der Waals, J. H., & Platteeuw, J. C. (1959). *Adv. Chem. Phys, 2*(1).
Villard, P. (1896). *Compt. Rend, 123*(337).
Vogel, K., EOSTG, & council, t. a. c. (2007). EthyleneOxide *Ethylene Oxide Product Stewardship Guidance Manual* (third ed., pp. 2-15, 118-135, 145-150).
Waite, W. F., Gilbert, L. Y., Winters, W. J., & Mason, D. H. (2005). *Proceedings of the 5th International Conference on Gas Hydrates, paper 5042*.
Wilcox, W., I., Katz, D. L., & Carson, D. B. (1941). Natural gas hydrates. *Ind. Eng. Chem., 33*(5), 662-665. doi: 10.1021/ie50377a027

APPENDIX

Appendix A: Calculation of stoichiometric concentrations of a solute

Appendix A.1: THF calculations

THF-water solution mole percent

	THF	H2O
MW	72,11	18,015
density	0,8892	1
moles	1	17

mole%	THFmass	H2Omass	Totalmass	sum
1,176	5,374346	114,1257	119,5	119,5
2,353	10,28609	109,2139	119,5	119,5
3,529	14,79249	104,7075	119,5	119,5
4,706	18,94175	100,5583	119,5	119,5
5,880	22,77469	96,72531	119,5	119,5
0,00294	1,390488	118,1095	119,5	119,5
0,00588	2,748989	116,751	119,5	119,5

		number of moles		Fraction	
wt %	mole%	THF	H2O	THF	H2O
0,2	1,176	0,07453	6,335035	0,044974	0,955026
0,4	2,353	0,142644	6,062388	0,086076	0,913924
0,6	3,529	0,205138	5,81224	0,123787	0,876213
0,8	4,706	0,262678	5,581918	0,158508	0,841492
1	5,880	0,315833	5,369154	0,190583	0,809417
0,05	0,002941	0,019283	6,556176	0,011636	0,988364
0,1	0,005882	0,038122	6,480767	0,023004	0,976996

wt %	volumes	
	THF	H2O
0,2	6,044023	114,1257
0,4	11,5678	109,2139
0,6	16,63573	104,7075
0,8	21,30201	100,5583
1	25,61256	96,72531
0,05	1,563751	118,1095
0,1	3,09153	116,751

Appendix A.2: EO calculations

	EO	H2O
MW	44,05	18,015
density	0,8697	1
moles	3	23

wt %	n%	fraction of	fraction of	m EO	m H2O	m total	V EO	V H2O	V total

		EO	H2O						
0,2	2,608696	0,062459382	0,937540618	3,591414	53,90859	57,5	4,129487	53,90859	57,5
0,4	5,217391	0,122371025	0,877628975	7,036334	50,46367	57,5	8,09053	50,46367	57,5
0,6	7,826087	0,179887698	0,820112302	10,34354	47,15646	57,5	11,89323	47,15646	57,5
0,8	10,43478	0,235150194	0,764849806	13,52114	43,97886	57,5	15,5469	43,97886	57,5
1	13,04348	0,288288485	0,711711515	16,57659	40,92341	57,5	19,06012	40,92341	57,5
0,05	0,652174	0,015862537	0,984137463	0,912096	56,5879	57,5	1,048748	56,5879	57,5
0,1	1,304348	0,031558209	0,968441791	1,814597	55,6854	57,5	2,086463	55,6854	57,5

Appendix B: Experimental Analysis

Appendix B.1: Outer heat transfer coefficient (hO) calculations

Outer heat transfer coefficient, titanium hydrate cell.

14.05.2013; **updated 25.03.2014** (By Prof. Runar Bøe)

Flow rate capacity for pump unit obtained from internet
(`http://www.julabo.de/en/products/refrigeratedcirculators/refrigerated-heating-circulators/f33-hl-refrigeratedheating-circulator`)

(Should be confirmed) is 22 - 26 l/min. This corresponds to 4.33e-4 m3/s for the high estimate (26 l/min).

Measurement of cooling water flow rate gives **14 l/min** (should be confirmed)
Physical data for water at 5 - 10 C is approximately [i.e. rounded to at most 2 significant figures] (Mörtstedt/Hellsten - Data och Diagram):

Heat capacity: cw = 4200 J/kg K
Density: ρw = 1000 kg/m3
Thermal conductivity: kw = 0.57 W/m K
Dynamic viscosity: μw = 1.4e-3 Ns/m2
This gives a Prandtl number; Prw ≈ 10.

The cooling water flows in a concentric annulus with the following dimensions:

Outer diameter: Do = 101 mm
Inner diameter: Di = 90 mm
Length: L ≈ 109 mm
Cross section: Ac = 1.65e-3 m2
Hydraulic diameter: Dh = 0.011 m
Diameter ratio, Di/Do: r* = 0.891

(See attached calculation details for the numerical values)

Flow regime:
The Reynolds number based on hydraulic diameter as the characteristic length scale, and the average velocity calculated as Q/A becomes quite low; **Re = 1100** using the measured value for flow rate of 14 l/min. If maximum flow rate could be obtained this would give $\mathbf{Re_{max}}$ **= 2043**. This can be pointed out as a special consideration for annular geometries: The cross section for the flow may be quite large, while the characteristic length scale for flow is small. This leads to a low average flow velocity, combined with a small length scale, and in combination this may leads to very low Reynolds numbers.

For internal flow, however, it is assumed that the results obtained for circular pipes are more or less transferable to non-circular geometries, when replacing the diameter with the hydraulic diameter. In that case, **the flow in the cooling mantle should be well within the laminar regime**, at most bordering on transition to turbulence.

That the flow is laminar indicates that the outer heat transfer coefficient may not be as high as initially assumed. If it had been possible to justify that it would be in the upper range for forced convection in liquids, say, in the order of 10000 W/m^2K, it would be somewhat negligible in the sense that it would represent a small resistance towards heat transfer at the outer cell wall.

On the other hand, a laminar flow regime may better lend itself to CFD simulations, should one see the need for a more thorough theoretical treatment of the phenomenon.

Correlations for laminar flow will usually give a quite low estimate for heat transfer coefficients, but they assume fully developed temperature- and velocity profiles. When entry effects are included (i.e. for short lengths) this will always lead to higher values for the heat transfer coefficient.

Correlations for laminar flow; in short:

1. In contrast to turbulent flow, it is possible to obtain analytical solutions for convection heat transfer in the laminar flow regime. Theoretically, in laminar flow, there is a total absence of fluid movement in the direction perpendicular to the flow (i.e. in the y-direction, assuming that the flow moves in the x-direction). One important find for the simple tube geometry is that when both the temperature- and velocity profiles are fully developed (i.e. at a distance sufficiently far from the entrance of the tube for the flow to smooth out and become essentially laminar), the heat transfer coefficient is a function of the fluid conductivity and the length scale only, and independent of flow velocity, fluid density- and heat capacity, and so on. In other words, the heat transfer is completely dominated by conduction in the fluid, and thereby far less efficient than in the turbulent regime.

2. For an annular geometry, the scene is slightly more complicated, since one need to consider two heated (or cooled, or one heated and one cooled) surfaces, vs. just one for the tube. But in essence, the heat transfer is still dominated by conduction. This is all taken from reference [1], and only cases with constant heat rate are considered in there (The other case, where surface temperatures are considered constant is just another approximation made, in order to formulate the right boundary conditions, so only slight numerical differences will be the case for the final solutions).

3. In the case of the hydrate cell, the length of the annulus is approximately the same as the outer diameter, and so we do not have a fully developed, laminar flow regime after all. And in contrast to a fully developed temperature profile in the flow, the case close to the entrance of an annulus will be that there is a more "square" than parabolic temperature profile, lead in to higher temperature gradient at the walls, and thereby to higher values of the heat transfer coefficient. In other words, what we are looking at here is a mode of convective heat transfer that will be more efficient than a truly laminar flow, but maybe not as efficient as a turbulent flow would be.

One thing to be considered in the cases of entry-length solutions, is whether only thermal effects need to be considered (which is simpler) or whether both hydrodynamic and thermal effects must be included. The textbook [1] states that for Prandtl-numbers greater than 5, it can be assumed that the velocity profile develops so much faster than the temperature profile, that the solutions that assumes a fully developed velocity profile at all times can be used (even if this obviously is not the case for real). The Prandtl number is a (temperature dependent) pure fluid parameter, and for cool water Pr ≈ 10, so we are "in the clear".

Estimating the outer heat transfer coefficient:

First, let us calculate the "extremal" values: If the laminar velocity profile was fully developed, and only conduction governs the heat, the outer heat transfer coefficient for the cell wall (which in terms of the current geometry is the *inner* coefficient ☺ for the annulus) is given by the following formula:

$$Nu_i = \frac{h_i D_h}{k} = \frac{Nu_{ii}}{1 - \left(\frac{\dot{q}''_o}{\dot{q}''_i}\right)\theta_i^*}$$

Obtained through interpolation in **Table 8-1** (for r* = 0.891) are the following values **(again, see the calculation details)**:

Nu_{ii} = 5.49
θ_i = 0.376

What we need to guess (in lieu of any other sensitive way to do it) is how the surface heat fluxes on the outer- and inner surface of the annular space relate to each other. First- they will both be positive during a run with hydrate growth, since both surfaces are **cooled by the cooling water** (heat enters the fluid, by the reaction, and from the surroundings), so the ratio is a positive number, which could be around 1 - 0.5 (?) (the outer surface works towards a higher temperature difference than the inner, but also towards free convection in air; 1 is as good an estimate as anything). If it was possible to insulate the cooling mantle from the surroundings, it could be argued that this ration would be closer to 0 (exactly zero for perfect insulation). The ratio would be negative for the cases where the cell is heated by the cooling water, but still below ambient temperature; what is more this means that for laminar flow the heat transfer coefficient **should** change according to what mode the cell is operated in.

So with numbers: $Nu_i = 5.49/(1 - 0.376) = 8.8 \Rightarrow h = 8.8*0.57/0.011 =$ 456 W/m^{2}K, assuming a ratio of heat fluxes of 1; further summarized:

q_o/q_i	Nu_i	h [W/m2 K]
-0.5	4.62	239
0	5.49	285
0.5	6.76	350
1	8.8	456

So if the flow was truly laminar, the heat transfer coefficient for the mantle would be somewhat dependent on the operation, but **in the order of 250 - 450 W/m^{2}K**

The other extreme will be to assume that the flow is "turbulent-like" enough to use correlations for the turbulent flow regime; after all, the calculated Reynolds number could be in the borderland of turbulence, since the laminar regime will not be fully developed. According to ref. [1], the same equation should apply for turbulence, only with different values for the Nusselt number and the influence coefficient.

These values can be obtained by **Table 13-5**, which really is for parallel planes, but closer to r* = 0.981 than the preceding table, which is for r* = 0.5. The lowest Reynolds number in the table is 10000, indicating that the values should be somewhat lower for lower Reynolds numbers:

Nu_{ii} = 101
θ^*_i = 0.046

Since this particular table states that one of the planes is insulated, this really makes the influence coefficient obsolete. so assuming $Nu_{ii} = 100$ and no influence by a heat flux on the other side of the gap: $Nu_i = Nu_{ii} = 100 \Rightarrow h = 100*0.57/0.011 =$ 5182 W/m^{2}K. This can then be regarded as a high estimate; i.e if the flow was turbulent; a heat transfer coefficient **in the order of 5000 W/m^{2}K.**

For the in-between case, with an entry length and all, we must first quantify the entry length, and this is done by the dimensionless parameter:

$$x^+ = \frac{2\left(\frac{x}{D_h}\right)}{Re \cdot Pr}$$

For our case, the entry length x = L, and the dimensionless counterpart becomes:
$x+ = 2*(0.109/0.011)/(1100 * 10) = 0.0018$

In this case we must do a few interpolations in **Table 8-10**, which should give:

Nu_{ii} = 18.746
θ^*_i = 0.0302

Which for the same values for the heat flux rations as used for the fully laminar case should give a similar table:

q_o/q_i	Nu_i	h [W/m2 K]
-0.5	18.47	957
0	18.746	971
0.5	19.03	986
1	19.33	1002

As seen, the influence of how the heat fluxes are configured is much less in this un-developed "laminar-like" flow regime than if had been a fully developed one. So we may conclude that it will **be in the order of 1000 W/m^{2}K**

So in sum:

If fully developed laminar flow:	h ≈ 250 - 450 W/m^{2}K
For the most likely flow regime:	**h ≈ 1000 W/m^{2}K**
If fully turbulent flow:	h ≈ 5000 W/m^{2}K

References:

1. Kays, W.M., Crawford, M.E.: *Convective Heat and Mass Transfer*, 2nd Ed., McGraw-Hill, 1980, ISBN 0-07-033457-9

Tables:

Table 8-1 Circular-tube-annulus solutions for constant heat rate and fully developed velocity and temperature profiles

r^*	Nu_{ii}	Nu_{oo}	θ_i^*	θ_o^*
0	∞	4.364	∞	0
0.05	17.81	4.792	2.18	0.0294
0.10	11.91	4.834	1.383	0.0562
0.20	8.499	4.883	0.905	0.1041
0.40	6.583	4.979	0.603	0.1823
0.60	5.912	5.099	0.473	0.2455
0.80	5.58	5.24	0.401	0.299
1.00	5.385	5.385	0.346	0.346

Table 8-10 Nusselt numbers and influence coefficients for the circular-tube-annulus family; constant heat rate; thermal-entry length

$r^* = r_i/r_o$	x^+	Nu_{ii}	Nu_{oo}	θ_i^*	θ_o^*
0.05	0.002	33.2	13.4	0.1265	0.00255
	0.01	24.2	7.99	0.460	0.00760
	0.02	21.5	6.58	0.817	0.0125
	0.10	18.1	4.92	2.13	0.0278
	0.20	17.8	4.80	2.17	0.0293
	∞	17.8	4.79	2.18	0.0294
0.10	0.002	25.1	13.5	0.0914	0.00491
	0.10	17.1	8.08	0.311	0.0147
	0.02	14.9	6.65	0.540	0.241
	0.10	12.1	4.96	1.296	0.0521
	0.20	11.9	4.84	1.38	0.0560
	∞	11.9	4.83	1.38	0.0562
0.25	0.002	18.9	13.8	0.0605	0.01104
	0.01	12.1	8.28	0.194	0.0328
	0.02	10.2	6.80	0.325	0.0540
	0.10	7.94	5.04	0.746	0.118
	0.20	7.76	4.91	0.789	0.125
	∞	7.75	4.90	0.793	0.125
0.50	0.002	16.4	14.2	0.0437	0.0189
	0.01	10.1	8.55	0.1347	0.0570
	0.02	8.43	7.03	0.224	0.0934
	0.10	6.35	5.19	0.498	0.204
	0.20	6.19	5.05	0.526	0.215
	∞	6.18	5.04	0.528	0.216
1.00	0.0005	23.5	23.5	0.01175	0.01175
(Parallel	0.005	11.2	11.2	0.0560	0.0560
planes)	0.02	7.49	7.49	0.1491	0.1491
	0.10	5.55	5.55	0.327	0.327
	0.25	5.39	5.39	0.346	0.346
	∞	5.38	5.38	0.346	0.346

Table 13-5 Nusselt numbers and influence coefficients for fully developed turbulent flow between parallel planes; constant heat rate; one side heated and the other side insulated

Re	Laminar		10^4		3×10^4		10^5		3×10^5		10^6	
Pr	Nu	θ^*	Nu	θ^*	Nu	θ^*	Nu	θ^*	Nu	θ^*	Nu	θ^*
0.0	5.385	0.346	5.70	0.428	5.78	0.445	5.80	0.456	5.80	0.460	5.80	0.468
0.001			5.70	0.428	5.78	0.445	5.80	0.456	5.88	0.460	6.23	0.460
0.003			5.70	0.428	5.80	0.445	5.90	0.450	6.32	0.450	8.62	0.422
0.01			5.80	0.428	5.92	0.445	6.70	0.440	9.80	0.407	21.5	0.333
0.03			6.10	0.428	6.90	0.428	11.0	0.390	23.0	0.330	61.2	0.255
0.5			22.5	0.256	47.8	0.222	120	0.193	290	0.174	780	0.157
0.7			27.8	0.220	61.2	0.192	155	0.170	378	0.156	1,030	0.142
1.0			35.0	0.182	76.8	0.162	197	0.148	486	0.138	1,340	0.128
3.0			60.8	0.095	142	0.092	380	0.089	966	0.087	2,700	0.084
10.0			101	0.045	214	0.045	680	0.045	1,760	0.045	5,080	0.046
30.0			147	0.021	367	0.022	1,030	0.022	2,720	0.023	8,000	0.024
100.0			210	0.009	514	0.009	1,520	0.010	4,030	0.010	12,000	0.011
1,000.0			390	0.002	997	0.002	2,880	0.002	7,650	0.002	23,000	0.002

From Mörtstedt & Hellsten, Data och Diagram: Physical data for water

72

ALLMÄNNA FYSIKALISKA DATA FÖR VATTEN, LUFT OCH KÖLDMEDIA

Medium	Temp. °C	Värmekapacitivitet c_p J/(kg·°C)	Densitet ϱ kg/m³	Värmekonduktivitet λ W/(m·°C)	Dynamisk viskositet $10^6 \cdot \eta$ Pa·s	Kinematisk viskositet $10^6 \cdot \nu$ m²/s	Värmediffusivitet $10^6 \cdot a$ m²/s	$Pr = \frac{\nu}{a}$	$Gr \cdot Pr \cdot 10^{-10}$ vid $l = 1$ m och $\theta = 1$ °C
Vatten	0	4 225	999,8	0,559	1 792	1,792	0,132	13,57	≈ 0,2
vätska vid $p = 1$ bar	5	4 206	1 000	0,568	1 519	1,519	0,135	11,35	0,071
$M = 18{,}016$	10	4 194	999,7	0,577	1 308	1,308	0,138	9,42	0,494
$R = 460$	20	4 181	998,2	0,597	1 005	1,004	0,143	6,97	1,433
$t_{krit} = 374{,}15$ °C	30	4 175	995,7	0,615	801	0,805	0,148	5,38	2,51
$P_{krit} = 221{,}29$ bar	40	4 175	992,2	0,633	656	0,661	0,153	4,34	3,73
	50	4 177	988,1	0,647	549	0,556	0,157	3,58	5,09
	60	4 180	983,2	0,659	469	0,477	0,161	2,99	6,64
	70	4 186	977,8	0,668	406	0,417	0,163	2,53	8,52
	80	4 193	971,8	0,674	357	0,367	0,165	2,19	10,52
	90	4 201	965,3	0,678	317	0,328	0,167	1,91	12,77
	100	4 210	958,4	0,682	284	0,296	0,169	1,72	15,0

Appendix B.2: Mass of air (kg) calculations

pressure	P	55000
temperature	T	275,65
gas constant	R	8,3144
compressibility	Z	1
Volume	V	
celle #0	V (cell #0)	0,0000915
celle#5	V (cell #5)	0,000206
moles	n	0,00494357
mass (g)	m	0,14336363
Molecular weight	M	29
m (kg)		0,00014336

PV = ZnRT

$$m = nM = \frac{PVM}{ZRT}$$

Appendix B.3: The numerical model by use of Matlab

Appendix B.3.1: "Try and Fail" method

```
%%%%%%%%%%%%%%%%%%%%%%%%%%%%%%%%%%%%%%%%%%%%%%%%%%%%%%%%%%%%%%%%%%%%%%%%%%%
% Simulating radial heat transfer through titanium hydrate cell using the
% implicit discretization scheme.
% NB! In order to run, the outer border temperature vector TO must be
% imported to the workspace first; in order to compare with measured
% results, the representative inner border temperature TIr is also needed.
% (and to initialize properly)
%  THIS IS THE ORIGINAL SIMULATION FILE ASSUMING NO HYDRATE GENERATION,
%  UPDATED AND MODIFIED TO PERFORM SIMULATIONS ON THE QUIESENT SLURRY
%  CASES. NOTE THAT 3 PHASES ARE NOW PRESENT IN THE CELL, AND IT IS ASSUMED
%  THAT THEIR RELATIVE AMOUNTS ARE UNCHANGING DURING A RUN.
%  31.03.2014


% Constants:
% Titanuim:
k   = 21.9;  % W/m K
rho = 4506;  % kg/m3
c   = 544;   % J/kg K
% Cylinder:
Ri       = 0.03;   % m
Ro       = 0.045;  % m
delta    = 0.05;   % m
% Fluids:
% Water:
mw       = 112*1e-3; % kg (0.05 kg corresponds to 50 ml)
cw       = 4205; % J/kg K
% Hydrate, pure THF/EO:
mH       = 0;  % kg
```

```
cH      = 1600  % J/kg K
% gas: air:
Ng      = 1.4*1e-4;  % kg
Cpg     = 1004;   % J/kg K
% Heat transfer coefficients:
hI      = 249.3645 % W/m2 K
hO      = 1000  % W/m2 K
% Grid:
N   = 18;
Dt  = 3;    % s
% Calculated properties:
alpha   = k/(rho*c);
Dr      = (Ro - Ri)/N;
Fo      = alpha*Dt/Dr^2;
BiI     = hI*Dr/k;
BiO     = hO*Dr/k;
CI      = 2*hI*pi*delta*Ri*Dt/(mw*cw + mH*cH + Ng*Cpg);
A_half  = 2*pi*(Ri + Dr/2)*delta;
A_nhalf = 2*pi*(Ro - Dr/2)*delta;
% Time steps in current border vector:
s       = size(TO);
s(:,2)  = [];
M   = s
% R-vector for plotting (R = 0 for interior of cell)
R       = [];
R(1,1)  = 0;
for i   = 2:(N+2)
    R(i,1)   = Ri + (i-2)*Dr;
end


%Setting up the A-matrix (This is constant throughout):
A   = [];
% First row; entry I - cell interior:
A(1,1)  = 1 + CI;
A(1,2)  = -CI;
for j   = 3:(N+2)
    A(1,j)  = 0;
end
% Second row; entry 0 - inner border/wall:
A(2,1)  = -2*BiI*Fo;
A(2,2)  = (1 + 2*(BiI + (Dr/(2*Ri) + 1))*Fo);
A(2,3)  = -2*(Dr/(2*Ri) + 1)*Fo;
for j   = 4:(N+2)
    A(2,j)  = 0;
end
% Internal node rows 1 - (n-1) => i = 3 - (N+1):
for i   = 3:(N+1)
    for j   = 1:(i-2)
        A(i,j)  = 0;
    end
    r   = Ri + (i-2)*Dr;
    A(i,(i-1))  = (Dr/(2*r) - 1)*Fo;
    A(i,i)      = (1 + 2*Fo);
    A(i,(i+1))  = -(Dr/(2*r) + 1)*Fo;
    for j   = (i+2):(N+1)
        A(i,j)  = 0;
    end
end
% Last row; entry N+2 - outer border:
```

```
for j   = 1:N
    A((N+2),j)  = 0;
end
A((N+2),(N+1))  = 2*(Dr/(2*Ro) - 1)*Fo;
A((N+2),(N+2))  = (1 + 2*(BiO - (Dr/(2*Ro) - 1))*Fo);
%Inverting the A-matrix:
AI  = inv(A);

% Initializing the Y-vector:
Y   = [];
for i   = 1:(N+1)
    Y(i,1)  = TIr(1,1);   % To compare the excel run
end
Y((N+2), 1) = TO(1,1) + 2*BiO*Fo*TO(2,1);
%Y
% Vectors for time series plotting:
Time    = [];
TI      = [];   % Interior; i.e. the temperature of the fluids (g + w)
TOp     = [];   % Need an extra plotting vector for the bath temperature
                %(to be of the same length as the time vector)
TIp     = [];
TW      = [];   % Need to plot the wall temperature too
% Heat vectors:
QI      = [];   % Heat to/from the interior
QO      = [];   % Heat to/from the cooling mantle

% Starting time loop (With measured values the number of repetitions is
% given by the size of the input vector, M):
t   = 0;
Time    = [Time; t];
TI      = [TI; TIr(1,1)];
TIp     = [TIp; TIr(1,1)];
% Initializing for "artificial" conditions, i.e. when no measurements for
% cell interior exis:
%TIp     = [TIp; TO(1,1)];
TOp     = [TOp; TO(1,1)];
TW      = [TW; TO(1,1)];
% Initially, no heat when temperature is homogeneous
QI      = [QI; 0];
QO      = [QO; 0];
% Testing part of run: %%%%%%%%%%%%%%%%%%%%%%%%%%%%%
%dTdt    = (TIr(2,1) - TIr(1,1))/Dt
%QI      = [QI; (mw*cw + Ng*Cpg)*-dTdt];
%QO      = [QO; (mw*cw + Ng*Cpg)*-dTdt*2.873];
%pause;
%%%%%%%%%%%%%%%%%%%%%%%%%%%%%%%%%%%%%%%%%%%%%%%%%%%%%%%%%%%%%%%%%%%%%%%
for i   = 1:(M-2)
%for i   = 1:194
    T   = AI*Y;
    TI  = [TI; T(1,1)];
    TW  = [TW; T(2,1)];
    TIp = [TIp; TIr((i+1),1)];
    TOp = [TOp; TO((i+1),1)];
    Tnp = T((N+2),1);
    qI  =  -k*A_half*(T(3,1) - T(2,1))/Dr;
    QI  = [QI; qI];
    qO  = -k*A_nhalf*(T(N+2) - T(N+1))/Dr;
    QO  = [QO; qO];
    Y   = T;
    %pause;
```

```
    Y((N+2), 1) = Tnp + 2*BiO*Fo*TO((i+2),1);
    %Y
    %pause;
    t   = t + Dt;
    Time    = [Time; t];
end
t

% Figure 1 = heat rate plots
figure(1);
plot(Time, QI);      % Blå - inner
hold;
plot(Time, QO, 'r');    % Rød - outer
%plot(Time, QOm, 'g');   % Grønn - målt/estimert fra kappemålinger
hold;

% Figure 2 - temperature vs. time plots
figure(2);
plot(Time, TI);     % Simulert (= blå)
hold;
plot(Time, TOp, 'r'); % målt = rød
plot(Time, TIp, 'g'); % målt = grønn
%plot(Time, TW, 'y');
hold;

% Figure 3 - wall temperature profile at end
figure(3);
plot(R, T);
%axis([0, 0.045, 14, 18.5]);
```

Appendix B.3.2: "Golden Search" method

```
%%%%%%%%%%%%%%%%%%%%%%%%%%%%%%%%%%%%%%%%%%%%%%%%%%%%%%%%%%%%%%%%%%%%%%%%%%%%%%%%
% Golden section procedure to find the hI that minimizes variance between
% measured and simulated temperature time series for "slurry tests". hO
% must be set to a predefined value.


global TIr TO

hO  = 1000  %W/m2 K 1000 is obtained by correllations for thermal entry
            % lenght [Ref. Kays and Crawford]

conv    = 1e-5;
% hI expected to fall between the values A and B
A   = 1.0;  %W/m2K
B   = 10000;

R   = (sqrt(5) -1)/2;

% Initialize:
x   = A + R*(B - A);
u   = heat_trans_slurry_f(x, hO);
y   = A + R^2*(B - A);
v   = heat_trans_slurry_f(y, hO);
% Testing:
while abs(x - y) >= conv
```

```
    if u > v
        B   = x;
        x   = y;
        u   = v;
        y   = A + R^2*(B - A);
        v   = heat_trans_slurry_f(y, h0);
    else
        A   = y;
        y   = x;
        v   = u;
        x   = A + R*(B - A);
        u   = heat_trans_slurry_f(x, h0);
    end
end
hI = x
```

Appendix C: Raw Data

Appendix C.1: Baseline

Cell #0			
Baseline	(0 % of the stochiometric conc.)		
Rotational speed [RPM]	0	500	1000
h #1 [W/m^2 K]	86,92	233,86	222,86
h #2 [W/m^2 K]	87,12	235,97	222,31
h #3 [W/m^2 K]	88,05	233,15	209,91
h mean[W/m^2 K]	87,36	234,33	218,36

Cell #5			
Baseline	(0 % of the stochiometric conc.)		
Rotational speed [RPM]	0	500	1000
h #1 [W/m^2 K]	77,06	297,03	251,40
h #2 [W/m^2 K]	80,68	307,78	256,97
h #3 [W/m^2 K]	83,90	319,23	249,36
h mean [W/m^2 K]	80,54	308,02	252,58

Appendix C.2: THF

Cell #0			
20 % THF	(20 % of the stoichiometric conc.)		
Rotational speed [RPM]	0	500	1000
h #1 [W/m^2 K]	69,60	170,09	131,97
h #2 [W/m^2 K]	70,44	168,29	142,21
h #3 [W/m^2 K]	70,02	171,44	122,04
h mean [W/m^2 K]	70,02	169,94	132,07

Cell #0			
40 % THF	(40 % of the stoichiometric conc.)		
Rotational speed [RPM]	0	500	1000
h #1 [W/m^2 K]	48,80	56,80	83,06
h #2 [W/m^2 K]	38,91	57,56	76,73
h #3 [W/m^2 K]	35,55	64,46	91,70
h mean [W/m^2 K]	41,09	59,61	83,83

Cell #0			
60 % THF	(60 % of the stoichiometric conc.)		
Rotational speed [RPM]	0	500	1000
h #1 [W/m^2 K]	37,86	49,18	50,92
h #2 [W/m^2 K]	28,57	43,14	48,02

h #3 [W/m^2 K]	23,55	47,43	43,54
h mean [W/m^2 K]	29,99	46,59	47,49

Cell #0			
80 % THF	(80 % of the stoichiometric conc.)		
Rotational speed [RPM]	0	500	1000
h #1 [W/m^2 K]	35,47	35,95	49,33
h #2 [W/m^2 K]	36,66	34,08	55,88
h #3 [W/m^2 K]	35,94	61,80	59,36
h mean [W/m^2 K]	36,03	43,94	54,86

Cell #0			
100 % THF	(100 % of the stoichiometric conc.)		
Rotational speed [RPM]	0	500	1000
h #1 [W/m^2 K]	39,73	34,58	36,16
h #2 [W/m^2 K]	38,99	34,45	37,25
h #3 [W/m^2 K]	38,51	42,13	39,29
h mean [W/m^2 K]	39,08	37,05	37,57

Cell #5			
40 % THF	(40% of the stoichiometric conc.)		
Rotational speed [RPM]	0	500	1000
h #1 [W/m^2 K]	17,33	65,19	105,34
h #2 [W/m^2 K]	17,78	74,79	100,97
h #3 [W/m^2 K]	16,40	76,03	184,04
h mean [W/m^2 K]	17,17	72,00	130,12

Cell #5			
80 % THF	(80 % of the stoichiometric conc.)		
Rotational speed [RPM]	0	500	1000
h #1 [W/m^2 K]	19,69	21,65	21,05
h #2 [W/m^2 K]	20,27	24,56	26,25
h #3 [W/m^2 K]	20,39	19,11	26,79
h mean [W/m^2 K]	20,12	21,77	24,70

Appendix C.3: EO

Cell #0			
20 % EO	(20 % of the stochiometric conc.)		
Rotational speed [RPM]	0	500	1000
h #1 [W/m^2 K]	77,11	88,90	87,87
h #2 [W/m^2 K]	82,18	98,25	82,52
h #3 [W/m^2 K]	81,54	90,42	83,35
h mean [W/m^2 K]	80,28	92,52	84,58

Cell #0			
40 % EO	(40 % of the stochiometric conc.)		
Rotational speed [RPM]	0	500	1000
h #1 [W/m^2 K]	80,00	67,57	62,41
h #2 [W/m^2 K]	82,79	73,29	52,20
h #3 [W/m^2 K]	78,83	68,39	57,78
h mean [W/m^2 K]	80,54	69,75	57,46

Cell #0			
60 % EO	(60 % of the stoichiometric conc.)		
Rotational speed [RPM]	0	500	1000
h #1 [W/m^2 K]	112,22	69,07	52,67
h #2 [W/m^2 K]	110,00	75,08	53,95
h #3 [W/m^2 K]	124,93	72,74	54,69
h mean [W/m^2 K]	115,71	72,30	53,77

Cell #0			
80 % EO	(80 % of the stoichiometric conc.)		
Rotational speed [RPM]	0	500	1000
h #1 [W/m^2 K]	215,69	197,73	158,38
h #2 [W/m^2 K]	214,16	189,05	156,23
h #3 [W/m^2 K]	219,03	180,62	153,60
h mean [W/m^2 K]	216,29	189,13	156,07

Cell #0			
100 % EO	(100 % of the stoichiometric conc.)		
Rotational speed [RPM]	0	500	1000
h #1 [W/m^2 K]	120,80	112,83	93,65
h #2 [W/m^2 K]	118,05	90,13	92,97
h #3 [W/m^2 K]	117,68	93,82	91,47
h mean [W/m^2 K]	118,85	98,93	92,70

Cell #5			
40 % EO	(40 % of the stoichiometric conc.)		
Rotational speed [RPM]	0	500	1000
h #1 [W/m^2 K]	41,10	86,90	96,70
h #2 [W/m^2 K]	35,11	114,17	95,44
h #3 [W/m^2 K]	60,29	100,48	93,29
h mean [W/m^2 K]	45,50	100,51	95,14

Cell #5			
80 % EO	(80 % of the stoichiometric conc.)		
Rotational speed [RPM]	0	500	1000
h #1 [W/m^2 K]	76,99	81,11	92,39

h #2 [W/m^2 K]	78,97	92,20	89,57
h #3 [W/m^2 K]	73,95	99,84	85,73
h mean [W/m^2 K]	76,64	91,05	89,23

Means that the value can be affected by fluctuaction in HCS.

Means that the value isn`t 100 % certain the minimum variance.

Means that it may be melting/formation phenomenon during HSC.

(This is shown in figure 20.)